

Air Force Institute of Technology

AFIT Scholar

Theses and Dissertations

Student Graduate Works

12-16-2008

Integrated Approach to Airborne Laser Communication

James A. Louthain

Follow this and additional works at: <https://scholar.afit.edu/etd>



Part of the [Signal Processing Commons](#), and the [Systems and Communications Commons](#)

Recommended Citation

Louthain, James A., "Integrated Approach to Airborne Laser Communication" (2008). *Theses and Dissertations*. 2547.

<https://scholar.afit.edu/etd/2547>

This Dissertation is brought to you for free and open access by the Student Graduate Works at AFIT Scholar. It has been accepted for inclusion in Theses and Dissertations by an authorized administrator of AFIT Scholar. For more information, please contact richard.mansfield@afit.edu.



INTEGRATED APPROACH
TO
AIRBORNE LASER COMMUNICATION

DISSERTATION

James A. Louthain, Lieutenant Colonel, USAF

AFIT/DEE/ENG/09-02

DEPARTMENT OF THE AIR FORCE
AIR UNIVERSITY

AIR FORCE INSTITUTE OF TECHNOLOGY

Wright-Patterson Air Force Base, Ohio

APPROVED FOR PUBLIC RELEASE; DISTRIBUTION IS UNLIMITED

The views expressed in this dissertation are those of the author and do not reflect the official policy or position of the United States Air Force, Department of Defense, or United States Government.

AFIT/DEE/ENG/09-02

INTEGRATED APPROACH
TO
AIRBORNE LASER COMMUNICATION

DISSERTATION

Presented to the Faculty
Department of Electrical and Computer Engineering
Graduate School of Engineering and Management
Air Force Institute of Technology
Air University
Air Education and Training Command
In Partial Fulfillment of the Requirements for the
Degree of Doctor of Philosophy

James A. Louthain, B.S.E.E., M.S.E.E.
Lieutenant Colonel, USAF


December 2008

APPROVED FOR PUBLIC RELEASE; DISTRIBUTION IS UNLIMITED

INTEGRATED APPROACH
TO
AIRBORNE LASER COMMUNICATION

James A. Louthain, B.S.E.E., M.S.E.E.
Lieutenant Colonel, USAF

Approved:



Major Jason D. Schmidt, PhD
(Chairman)

10 Dec 08
Date




Dr. Michael A. Temple
(Member)

10 Dec 08
Date



Dr. Richard K. Martin
(Member)


10 Dec 08
Date



Dr. Matthew C. Fickus
(Member)

10 Dec 08
Date

Accepted:



M.U. Thomas
Dean, Graduate School of
Engineering and Management

16 Dec 08
Date

Abstract

Lasers offer tremendous advantages over RF communication systems in terms of bandwidth and security due to their ultra-high frequency and narrow spatial beamwidth. Unfortunately, atmospheric turbulence significantly increases the received power variation and bit error rate (BER) in free-space optical communication (FSOC) systems. Further, airborne optical communication systems require special considerations in size, complexity, power, and weight.

If two or more laser beams are sufficiently separated so that their turbulence effects are uncorrelated (i.e. anisoplanatic), they can effectively “average out” turbulence effects. This requisite separation distance is derived for multiple geometries, turbulence conditions, and optical properties. In most cases and geometries, the angles ordered from largest to smallest are: phase uncorrelated angle (equivalent to the tilt uncorrelated angle and phase anisoplanatic angle), tilt isoplanatic angle, phase isoplanatic angle, scintillation uncorrelated angle (or scintillation anisoplanatic angle), and scintillation isoplanatic angle ($\theta_{\psi_{ind}} > \theta_{TA} > \theta_0 > \theta_{\chi_{ind}} > \theta_{\chi_0}$). Conventional adaptive optics (AO) systems only correct for phase and cannot correct for strong scintillation, while multiple-transmitter systems use several transmission paths to “average out” effects of the strong scintillation by incoherently summing up the beams in the receiver.

Since all three airborne geometries (air-to-air, air-to-ground, and ground-to-air) are studied, a comparison of multiple-beam airborne laser communication system performance is presented for the first time. Wave optics simulations show that a combination of transmitter diversity, receiver and transmitter trackers, and adaptive thresholding can significantly reduce BER in an air-to-air FSOC system by over 10,000 times. As demonstrated in this work, two transmitters alone separated by only 31 cm (100 km path length, 1.55 μm wavelength, 4 km in altitude) provide a significant

BER improvement over one transmitter, especially for the strong turbulence regime where the required SNR for a fixed BER is reduced by 9 dB. Including the tracking and adaptive thresholding techniques, resulted in a 13 dB overall improvement. Two beams also reduce the fade length, suggesting even greater improvement can be obtained when interleaving and forward error correction coding is implemented.

To my daughters. May they always desire to learn...

Acknowledgements

Research by its very nature is truly a collaborative effort. Pushing the state of the art in any field requires a starting point built upon previous research. Thankfully, a lot of smart people have worked in this area before me, because I would not have known where to begin.

First and foremost, I thank my advisor Major Jason Schmidt for his ruthless editing and our several thought-provoking discussions. He hit the ground running with me after my previous advisor transferred. In addition, there were a couple of occasions when I doubted the feasibility of my approach, but each time Jason Schmidt set me back on the path.

The PhD process is similar to running a marathon. I thank Lt Col Matt Goda for starting me off on the right track with airborne laser communication, but unfortunately he was transferred. Thankfully, Dr. Mike Temple was there to hand me water and point me in the right direction as my Pro Tem Advisor and committee member. Major Schmidt also knew when to hand me water and how to keep me on the road, since he had just finished his marathon.

I thank my other committee members Dr. Richard Martin and Dr. Matt Fickus, and Dean's Representative Dr. Richard Cobb for their review of this document. I extend many thanks to my fellow PhD students here at AFIT for their mutual support and camaraderie over the past three years. I am very grateful to all of my teachers throughout my life. I thank my wife for her support and help during this process. Finally, I thank my family for their love and support.

James A. Louthain

Table of Contents

	Page
Abstract	iv
Acknowledgements	vii
List of Figures	ix
List of Tables	xi
List of Symbols	xii
List of Abbreviations	xv
I. Introduction	1
1.1 Motivation and challenges	1
1.2 Spatial diversity and redundancy	2
1.3 Adaptive system for temporal signal fluctuations	3
1.4 Scope and assumptions	3
1.5 Summary of main results	5
1.6 Dissertation organization	7
II. Background	8
2.1 Propagation of Gaussian-beam waves	8
2.2 Atmospheric turbulence effects	10
2.2.1 Index of refraction fluctuations in the atmosphere	10
2.2.2 Turbulence models and moments	16
2.2.3 Atmospheric phase parameters	18
2.2.4 Atmospheric beam wander and beam spreading	19
2.2.5 Beam wandering and spreading effects on laser communication	22
2.3 Amplitude effects	26
2.3.1 Strong fluctuation theory	29
2.3.2 Temporal effects	30
2.4 Layered atmosphere model	31
2.4.1 PDF of the scintillation	34
2.5 The PDF of intensity for multiple transmitters	36
2.6 Digital communication and detection theory	43
2.6.1 Modulation	43
2.6.2 Noise sources and measured signal probability density functions	45
2.6.3 Detection theory	45

	Page
III. Previous Work	48
3.1 Optical transmitter and receiver design	48
3.2 Wavefront control	50
3.3 Diversity techniques	53
3.4 Modulation techniques	54
3.5 Signal processing techniques	56
3.6 Assessment of best areas for further research	57
IV. Anisoplanatic Turbulence Effects	59
4.1 Uncorrelated paths	60
4.1.1 Phase isoplanatism	62
4.1.2 Angular phase independence of two beams	63
4.1.3 Parallel path isoplanatism	65
4.1.4 Tilt isoplanatism	66
4.1.5 Scintillation anisoplanatism	70
4.1.6 Considerations of isoplanatic and anisoplanatic effects	71
4.2 Simulation set-up and validation	74
4.2.1 Simulation set-up	76
4.2.2 Validation of simulation results	78
4.3 Modeling optical receiver signals and noise sources	80
4.4 Simulation approach	82
4.5 Simulation results	84
4.5.1 Differential irradiance and tilt variance	85
4.5.2 Bit error rates for independent realizations	87
V. Temporal Analysis and Signal Processing	94
5.1 Spatial statistics	94
5.1.1 Anisoplanatic effects	95
5.2 Temporal considerations	96
5.2.1 Frequency of the turbulence effects	97
5.2.2 Threshold determination	98
5.3 Simulation set-up	105
5.3.1 Modeling the turbulence	105
5.3.2 Temporally modeling tracker jitter	105
5.3.3 Modeling fiber coupling	106
5.4 Temporal results	108
5.4.1 Fade statistics	108
5.4.2 Bit error rate	110

	Page
VI. Conclusion	116
6.1 Challenges met	116
6.2 Key results	118
6.2.1 Anisoplanatic effects	118
6.2.2 Temporal aspects and fade statistics	120
6.2.3 Optimal fixed and adaptive thresholding	120
6.3 Recommendations for future work	121
6.3.1 Diversity techniques	121
6.3.2 Optical receiver design	122
6.3.3 Signal processing techniques	122
6.3.4 Tracking systems	123
6.3.5 Large communication system design	123
Bibliography	125

List of Figures

Figure		Page
1	Airborne Laser Communication Scenario	4
2	Collimated Beam Propagation	9
3	Inner Scale vs. Altitude.	15
4	Turbulence Profile.	17
5	Turbulence induced short-term beam spread for the 100 km air-to-air path with $C_n^2 = 10^{-17} \text{ m}^{-2/3}$	22
6	Long-term spot size.	23
7	PDF of Collected Power	25
8	CDF of Collected Power	26
9	PDF of sum of lognormal RVs and single lognormal variable	43
10	PDF of a single gamma-gamma RV and the PDF of the sum of 5 gamma-gamma RVs	44
11	Decision Threshold.	47
12	Isoplanatic angle geometry.	62
13	Phase Independence Distance Vs. Propagation Distance	65
14	Phase and log-amplitude structure functions for 100km path	73
15	Isoplanatic and anisoplanatic angles multiple turbulence scenarios .	75
16	Vacuum propagation compared to analytic solution	78
17	Comparison of phase screen structure functions with analytic calculation	79
18	Focal spot size in turbulence	83
19	Ground-to-Ground propagation differential irradiance and tilt variance	86
20	100km Air-to-air propagation differential irradiance variance	87
21	Differential irradiance variance for two angularly separated beams .	88
22	BER for a ground-to-ground link for angularly and parallel separated beams	89
23	BER for ground-to-air link for two angularly separated beams . . .	90

Figure		Page
24	BER for ground-to-air link with two parallel separated beams . . .	91
25	BER for Air-to-Air link for two angularly separated beams	92
26	Received signal PSD for a 100 km path at 4km in altitude	99
27	Phase and log-amplitude structure functions for 100km path	100
28	Adaptive threshold estimator.	104
29	Fade Definition using measured received signal for Scenario 5 (HHL)	109
30	Scenario 2 (HLL). The mean fade length (a) and number of fades per second (b)	110
31	Scenario 4 (HHH). The mean fade length (a) and number of fades per second (b)	111
32	Scenario 5 (HHL). The mean fade length (a) and number of fades per second (b)	111
33	Discretized PDFs of the received signals due to turbulence $p(i_s)$. .	112
34	BER for fixed and adaptive threshold systems for scenarios 1-5. . .	115

List of Tables

Table		Page
1	Required beam separation for averaging.	74
2	Atmospheric parameters for the scenarios used in the BER calculations.	76
3	Optimal separation distances for multiple Tx systems.	93
4	Atmospheric parameters for the scenarios used in the simulations. The optical wavelength was $\lambda = 1.55 \mu\text{m}$	95

List of Symbols

Symbol		Page
W_0	transmitter beam $1/e$ radius	8
F_0	transmitter beam radius of curvature	8
λ	optical wavelength (μm)	8
z	propagation distance	8
$W(z)$	laser beam spot size radius at z	9
$F(z)$	laser beam radius of curvature at z	9
n	index of refraction	10
$B(\mathbf{r}_1, \mathbf{r}_2)$	auto-covariance	11
$\langle \cdot \rangle$	ensemble average	11
$\Phi_f(\boldsymbol{\kappa})$	power spectral density (PSD) of f	11
$D_f(\mathbf{r})$	structure function	12
$\Phi_n^K(\kappa, z)$	Kolmogorov 3-D refractive index turbulence power spectrum .	12
L_0	outer scale	12
l_0	inner scale	12
$C_n^2(z)$	refractive index structure parameter	13
$\Phi_n^V(\kappa, z)$	von Kármán 3-D refractive index turbulence power spectrum .	13
h	height above the ground	16
μ_m	full turbulence moment	16
L	propagation path length	17
μ_m^-	lower turbulence partial moment	17
μ_m^+	upper turbulence partial moment	17
r_0	coherence diameter or Fried parameter	18
$r_{0,pw}$	plane-wave coherence diameter	18
$r_{0,sw}$	spherical-wave coherence diameter	18
$k = 2\pi/\lambda$	optical wave number	19
θ_0	phase isoplanatic angle	19

Symbol		Page
ξ	zenith angle	20
$\sigma_{x_c}^2$	turbulence-induced variance of the beam centroid in x	20
$\sigma_{y_c}^2$	turbulence-induced variance of the beam centroid in y	20
W_{ST}	turbulence-induced short-term beam radius	21
W_{LT}	turbulence-induced long-term spot size	21
\mathcal{R}	Rytov number	27
σ_χ^2	log-amplitude variance	27
σ_R^2	Rytov variance	29
f_G	Greenwood frequency	30
f_T	Tyler frequency	30
$E[\cdot]$	expectation operation	37
$\text{VAR}[\cdot]$	variance operation	37
\otimes	convolution operation symbol	41
\mathcal{F}	Fourier transform operator	41
\mathcal{F}^{-1}	inverse Fourier transform operator	41
$\mathcal{F}_{k,n}$	DFT operator	41
$\mathcal{F}_{k,n}^{-1}$	inverse DFT operator	41
$p(i_m H_1)$	PDF of the measurement of a ‘1’	46
$p(i_m H_0)$	PDF of the measurement of a ‘0’	46
$\theta_{\psi_{ind}}$	phase independence angle	63
Δx_0	parallel phase isoplanatic distance	66
ρ_0	spatial coherence radius	66
Δx_{ind}	plane-wave independent phase separation distance	66
θ_{TA}	tilt isoplanatic angle	68
ρ_{cw}	scintillation correlation width	70
ρ_c	scintillation correlation width scaling parameter $(L/k)^{1/2}$	70
$\theta_{\chi_{ind}}$	scintillation independence angle	71
$D_\chi(d)$	log-amplitude structure function	71

Symbol		Page
$D_\psi(d)$	phase structure function	71
σ_1^2	noise variance for the measurement of a ‘1’	81
σ_{elec}^2	thermal (or Johnson) noise	81
σ_{shot}^2	shot noise variance	81
σ_{ASE}^2	ASE noise variance for the EDFA	81
σ_j^2	error in the Tx tracker	83
$\tau_{\chi_{ind}}$	anisoplanatic irradiance time constant	97
τ_{irr}	isoplanatic irradiance time constant	98
i_T	threshold current (μA)	101
P_e	probability of an error	102
P_{md}	probability of a missed detection	102
P_{fa}	probability of a false alarm	102
Δ_m	differential of the measured signal	104
\hat{i}_s	estimated signal	104

List of Abbreviations

Abbreviation		Page
RF	radio frequency	1
FSOC	free-space optical communication	1
BER	bit error rate	3
HV-21	Hufnagel-Valley turbulence profile with $W = 21$ m/s	3
dB	decibels $\text{dB} = 10 \log_{10}(X)$	6
TEM	transverse electro-magnetic wave's laser beam shape mode	8
WSS	wide-sense stationary	11
rms	root-mean square	16
PDF	probability density function	20
CDF	cumulative density function	20
AOA	angle-of-arrival	24
Tx	transmitter	31
Rx	receiver	31
AO	adaptive optics	31
iid	independent identically distributed	37
RV	random variable	37
CLT	central limit theorem	40
DFT	discrete Fourier transform	41
EDFA	Erbium-doped fiber amplifier	49
ASE	amplified spontaneous emission	49
MIMO	Multiple-input and multiple-output	53
BPSK	binary phase-shift keying	54
OOK	on/off keying	55
PolSK	polarization shift keying	55
FEC	forward error correction code	56
APD	avalanche photo diode	82

Abbreviation		Page
PiN	P-type, intrinsic, and N-type layered diode	82
NA	numerical aperture of an optical fiber	82
SNR	signal-to-noise ratio	84
LRT	likelihood ratio test	101

INTEGRATED APPROACH
TO
AIRBORNE LASER COMMUNICATION

I. Introduction

1.1 Motivation and challenges

Laser communications offer tremendous advantages over radio frequency (RF) in bandwidth and security due to the ultra-high frequencies and point-to-point nature of laser propagation. In addition, optical transmitters and receivers are much smaller and lighter than their RF counterparts and operate at much lower power levels. Current airborne sensors are collecting data at an ever-increasing rate. With the advent of hyperspectral imaging systems and other sensors, this trend will continue as two-dimensional data are replaced by three-dimensional data cubes at finer resolutions. Current RF communication systems cannot keep up with this trend. In addition, free-space optical communication (FSOC) systems could provide covert, difficult to jam or intercept, high-speed, broadband connectivity to airborne (especially low-observable) platforms [86].

However, airborne laser communications are severely affected by clouds, dust, and atmospheric turbulence, causing deep, long fades at the receiver. Ultimately a hybrid communication system which includes RF communication is necessary, since clouds, fog, or dust occasionally obstructs the path for laser communication. Even when the channel is clear, the same atmospheric turbulence effects that limit the resolution of optical systems and make the stars twinkle can severely reduce the received power, causing long deep fades. This atmospheric turbulence in the propagation path causes the laser beam to wander, spread and break up. These effects can cause the received signal power to drop below the receiver's threshold for milliseconds at a time. For a 10 Gbit/s binary FSOC system, a millisecond fade means at least 5 million bit

errors. Since the turbulence of an air-to-air link extends along the entire path and causes long, deep fades, simply turning up the power would not be effective. In addition, airborne FSOC systems require special considerations in size, complexity, power, and weight.

There are essentially two different ways to improve this condition: increase the signal diversity to average out the effects or compensate for the turbulence conditions in real time. The first approach is implemented in this research by designing a multiple-transmitter system where the uncorrelated effects of each path are averaged at the receiver.

1.2 Spatial diversity and redundancy

In the night sky, objects like the moon and the planets do not twinkle like the stars. The uncorrelated amplitude fluctuations of the optical wavefronts from these extended incoherent objects are received by our eyes and these scintillation effects are averaged out. Multiple laser transmitters incoherent with each other and adequately separated act in much the same way.

Atmospheric turbulence causes random fluctuations of a wavefront's phase and amplitude in space and time due to the winds and platform velocities. Two beams traveling along the same path experience correlated effects, but as the separation distance increases these effects decorrelate. If these beams are separated so that the effects are relatively uncorrelated, each path experiences fades at different moments in time, allowing a multi-path system to "average out" the fades. As with a system where redundancy is built in to bypass a failure of a particular system, a multiple transmitter system provides multiple paths for the information to reach the receiver. This research analytically determines the requisite separation distances for uncorrelated phase and amplitude effects and verifies the results and improvements in simulation for an air-to-air FSOC system.

1.3 Adaptive system for temporal signal fluctuations

Once the system receives the signal, a binary digital receiver must determine if a ‘1’ or ‘0’ was sent by measuring the signal and determining whether that signal level is more indicative of a ‘1’ or a ‘0’. This is accomplished by using an appropriate threshold to decide if a ‘1’ or a ‘0’ was sent. Specifically, if the signal exceeds the threshold, it registers a ‘1’ and if it does not, it registers a ‘0’. For a digital communication system, a bit error occurs when a ‘1’ is transmitted and a ‘0’ is detected or when a ‘0’ is transmitted and a ‘1’ is detected. Optimal threshold determination depends upon the conditional probabilities of the signal level at the receiver for each symbol transmitted [82]. Since atmospheric random fluctuations cause these conditional probabilities to vary over time, it is beneficial to adaptively change the threshold given the current signal level to provide the maximum-likelihood optimal solution for each time slice [14, 18, 47]. The rate at which the turbulence causes fades and bit errors at the receiver is much slower than the data rate, thus a system can be designed to adaptively change this threshold with time. This research designs and tests by simulations realistic adaptive threshold systems and measures the bit error rate (BER) performance improvement.

1.4 Scope and assumptions

The links tested in this research are primarily: air-to-air links at distances of no more than 100 km at 10 km in altitude and air-to-ground and ground-to-air links (surface to 10 km) at elevation angles between 20 and 90 degrees. The simulations use the Hufnagel-Valley turbulence profile with $W = 21$ m/s (denoted by HV-21) [66]. These links are shown graphically in Fig. 1 and the HV-21 turbulence profile is shown in Fig. 4 in Chapter 2. Most regimes tested in this research are in the weak-turbulence regime where there is little-to-no saturation of the intensity variations. In the moderate-to-strong turbulence regime the amplitude effects (intensity variations, or scintillation) of the turbulence saturate, whereas the phase effects do

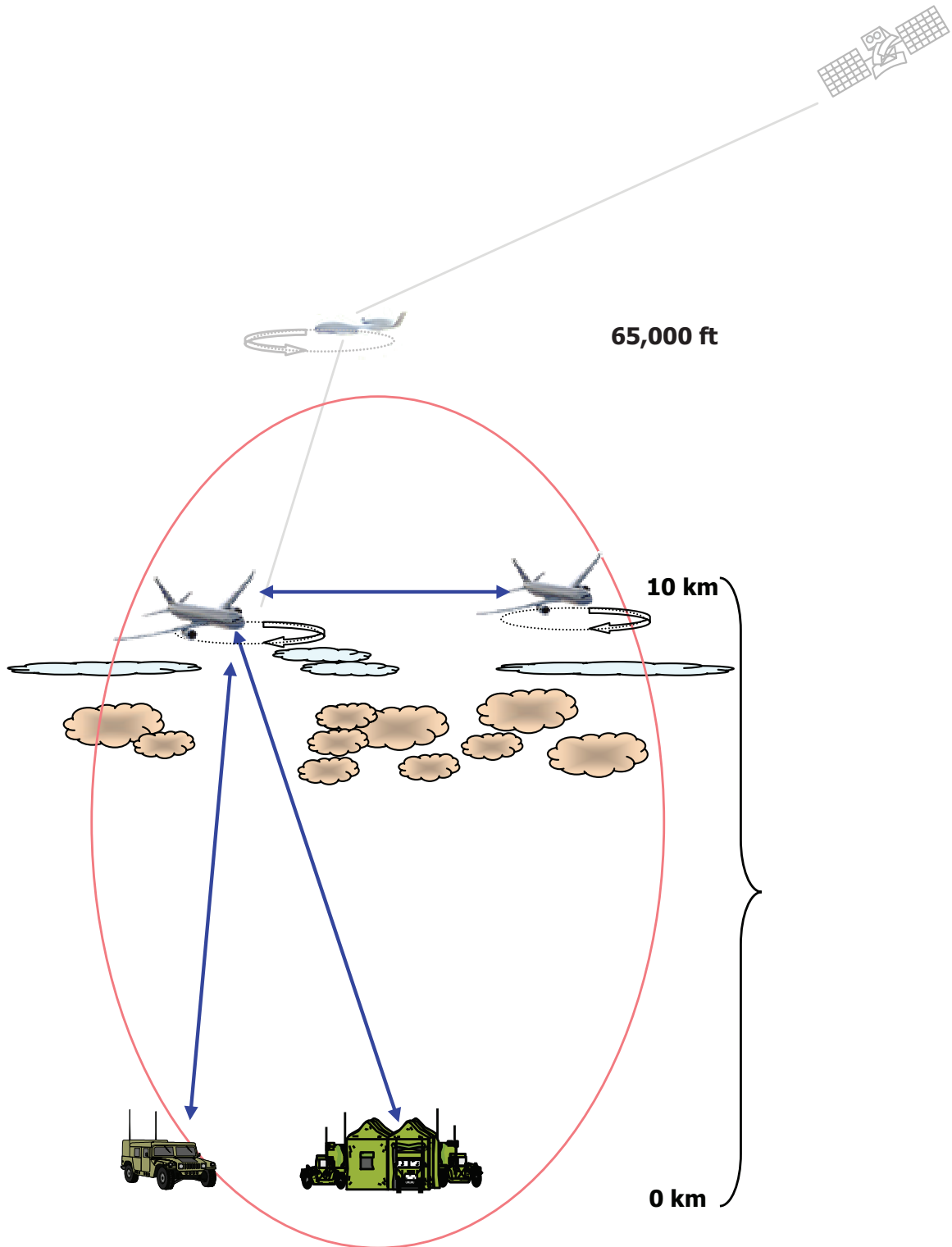


Figure 1: Airborne laser communication link scenarios tested in this research. Air-to-air links of 100 km at 10 km in elevation. Surface to 10 km: air-to-ground and ground-to-air links at elevation angles of: 20-90 degrees [20].

not. Moderate-to-strong turbulence regimes are identified and handled on a case-by-case basis.

In most cases, the atmospheric turbulence is assumed to be isotropic (statistical properties independent of direction) and homogeneous (statistical properties independent of position). The strength of turbulence varies with altitude. At each altitude the turbulence is assumed to be isotropic and homogeneous [2, 66, 69].

The turbulent air around an aircraft is neither isotropic nor homogeneous and cannot be modeled in the same way as atmospheric turbulence. Detailed analysis of aero-optic effects have not been covered in this research. Losses due to atmospheric absorption and extinction are estimated and attributed as a loss when calculating the received power.

To compare transmitter systems, one receiver size is used for all investigations. In practice, the collection optic should be made as large as possible. Not only do larger telescopes collect more power, the angle-of-arrival and intensity variations decrease as well. However, the larger the aperture the worse the effects due to higher-order phase perturbations. Aperture averaging of the intensity occurs when the receiver aperture is larger than the correlation width ρ_{cw} (i.e. characteristic size of highly correlated intensity at the receiver) [2].

1.5 Summary of main results

The goal of this research is to develop techniques and systems to improve two-way free-space laser communication between a ground station and an airborne platform and among airborne platforms. The techniques developed in this research are designed to minimize the complexity, size, weight, and power requirements, especially for airborne platforms.

Significant reductions in bit error rate are attained by implementing optimized multiple-transmitter systems to average out the deleterious effects of turbulence. Through analysis and simulation, optimal separations for double-transmitter sys-

tems for various geometries and tracking systems were determined. This research derived for the first time the optimal angular separations for multiple transmitter systems for airborne FSOC systems. A majority of previous research on multiple transmitters focused on satellite communications (where the turbulence is only present over a small part of the propagation path) or constant turbulence strength C_n^2 paths [4, 5, 29, 59, 60, 68]. The angular separations for all three airborne geometries (air-to-air, air-to-ground, and ground-to-air) are determined.

Previous research on isoplanatism defined the *maximum angle* over which the turbulence effects between two paths is relatively *similar* [26, 69]. These isoplanatic angles have been determined for the tilt variance, higher-order phase variance, and the scintillation (intensity variance). Here, that work is extended to determine the *minimum angle* at which the paths are relatively *different*. The less the effects between the paths are correlated, the better the averaging effect of multiple beams. Since all three airborne geometries are studied, a comparison of multiple-beam airborne laser communication system performance is presented for the first time.

Using these optimal separation distances, the temporal impacts of multiple transmitters are studied along with an adaptive threshold system. Wave-optics simulations show multiple transmitters, receiver and transmitter trackers, and adaptive thresholding significantly reduces BER (by a factor of 10,000). Two transmitters alone provide a significant BER improvement over one transmitter, especially for the strong turbulence regime with up to a 9-decibel (dB) improvement gain. Adaptive thresholding systems provide significant improvement over optimal fixed thresholds for both single- and double-transmitter systems, providing an additional 3-4 dB over both systems. This indicates that the improvement provided by these multiple techniques can be combined to provide even further improvement. There are further trickle-down effects, since two beams also reduce the fade length, indicating they would likely provide even greater improvement with interleaving and forward-error-correction coding.

1.6 Dissertation organization

Background on atmospheric turbulence effects and the impacts on digital laser communication are covered in Chapter II. Next, Chapter III examines what others have done to address the challenges of laser communication. Chapter IV derives the requisite separation distances and angles for averaging the effects by determining the minimum separation for uncorrelated phase and amplitude effects. In Chapter V, this separation is implemented in a time series simulation to determine the fade statistics as well as the tracking system performance. In addition, an ideal and realistic adaptive threshold system is implemented and compared with an optimal fixed threshold system. Finally, in Chapter VI conclusions for the research effort are summarized and recommendations for future research are discussed.

II. Background

This chapter briefly describes laser propagation through atmospheric turbulence and optical digital communication. The reader is referred to [2, 66, 69] for a more complete treatment of atmospheric turbulence effects and [1, 56] for additional considerations of optical communications. In addition, subsequent chapters of this dissertation describe in more detail special considerations and assumptions used to study these effects.

2.1 Propagation of Gaussian-beam waves

This first section describes how a laser beam propagates in a vacuum. Laser beams can propagate in different modes. In most cases, the lowest-order transverse electro-magnetic (TEM) Gaussian-beam mode TEM₀₀ is a good mode to work with, because the limiting cases include an infinite plane wave and a spherical wave. This research concentrates its analysis on this lowest-order TEM₀₀ mode.

A Gaussian laser beam is parameterized by its $1/e$ radius W_0 , its radius of curvature F_0 , and the optical wavelength λ . The initial optical field $U_0(r, 0)$ of the TEM₀₀ wave exiting the laser at $z = 0$, centered on the optical axis ($r = 0$) is [2]

$$U_0(r, 0) = a_0 \exp\left(\frac{-r^2}{W_0^2}\right) \exp\left(-jk\frac{r^2}{2F_0}\right), \quad (1)$$

where $r = (x^2 + y^2)^{1/2}$ is the radial distance from the optical axis and a_0 is optical field amplitude in $(\text{W}/\text{m}^2)^{1/2}$. The respective amplitude and phase of the Gaussian-beam wave are

$$A_0 = a_0 \exp\left(\frac{-r^2}{W_0^2}\right), \quad (2)$$

$$\phi_0 = -k\frac{r^2}{2F_0}. \quad (3)$$

Solving the wave equation for the Gaussian beam propagation results in [2]

$$U_0(r, z) = \frac{1}{\sqrt{\Theta_0^2 + \Lambda_0^2}} \exp\left[jkz - j \tan^{-1}(\Lambda_0/\Theta_0) - \frac{r^2}{W^2} - \frac{jk}{2F}r^2\right], \quad (4)$$

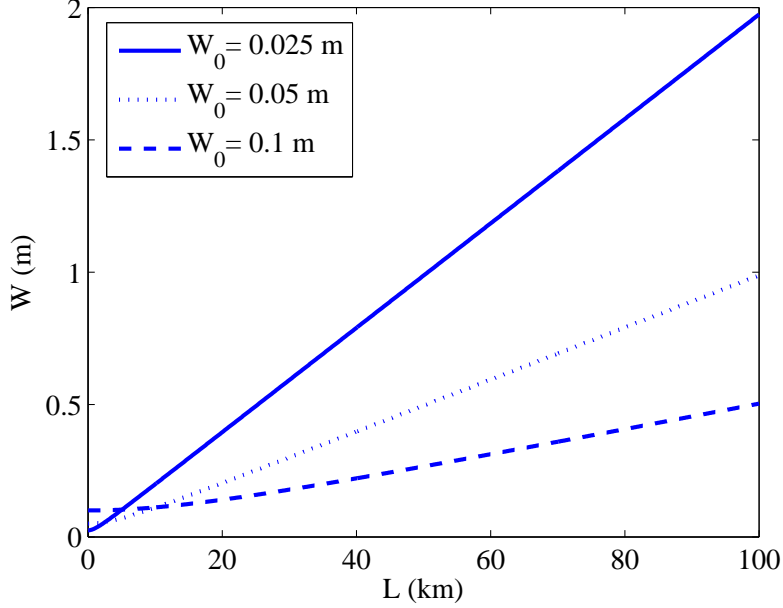


Figure 2: Diffraction effects on collimated laser beams of different beam widths.

where Θ_0 and Λ_0 are the set of input plane beam parameters defined by [2]

$$\Theta_0 = 1 - \frac{z}{F_0}, \quad \Lambda_0 = \frac{2z}{kW_0^2}. \quad (5)$$

The new spot size radius $W(z)$ and the new radius of curvature $F(z)$ at z and can be described by the input-plane beam parameters as [2]

$$W = W_0(\Lambda_0^2 + \Theta_0^2)^{1/2} \quad (6)$$

and

$$F = \frac{F_0(\Theta_0^2 + \Lambda_0^2)(\Theta_0 - 1)}{\Theta_0^2 + \Lambda_0^2 - \Theta_0}. \quad (7)$$

Figure 2 shows the spot size radius of three different size collimated beams (i.e. $F_0 \rightarrow \infty$) for a propagation distance out to $L = 100$ km. The plot shows the very strong inverse relationship of input beam size on the beamwidth for long laser propagations.

2.2 Atmospheric turbulence effects

2.2.1 Index of refraction fluctuations in the atmosphere. The atmospheric index of refraction fluctuations occur due to temperature and velocity differences caused by turbulent air movement. Optical waves that propagate through the atmosphere are distorted by these temporal and spatial refractive index fluctuations. These optical wave distortions make the stars twinkle, limit the resolution of imaging systems, and degrade the propagation of lasers.

This atmospheric turbulence caused by the heating and cooling of the earth and its atmosphere lead to large-scale variations in the air temperature. Kolmogorov's theory explains how these temperature differences cause winds that break up the large scale inhomogeneities into smaller ones as the laminar flow transitions to turbulent flow. This turbulent flow causes random pockets of temperature differences that vary randomly in time and space.

The index of refraction n is sensitive to temperature differences. At optical frequencies, the index of refraction as a function of air pressure (which drives the air density) and temperature is determined by [36]

$$n = n_0 + \frac{77.6P}{T} \times 10^{-6}, \quad \lambda = 500 \text{ nm} \quad (8)$$

where $n_0 = 1$, T is the temperature in Kelvins, and P is the air pressure in millibars. The temperature fluctuations normally dominate the index variations, although some turbulence around airframes might provide significant air density changes to appreciably affect the index of refraction.

Over the last 50 years since the invention of the laser in 1958 [71] and the first infrared sensors, modeling optical propagation through atmospheric turbulence has become increasingly important. Since the turbulence is random and cannot be predicted, several models have been developed to statistically characterize how the turbulence fluctuates. A.N. Kolmogorov's theory is the most widely accepted, due to

its simplicity and consistent agreement with observations [41]. Much of the research since is based on his theory.

Air masses of uniform index of refraction are commonly referred to as turbulent eddies. Kolmogorov assumed that these eddies are statistically homogeneous and isotropic. Assuming homogeneity and isotropy allow relations to be developed in the spatial and spectral domains to characterize the statistical nature of the fluctuations as random processes. Three relations in particular are used to characterize the random processes that describe turbulence: the three-dimensional covariance, structure function, and power spectral density (PSD).

First, consider a time-varying complex random process $f(\mathbf{r})$, where \mathbf{r} is a three-dimensional spatial vector. In many cases, the three-dimensional (3-D) auto-covariance $B(\mathbf{r}_1, \mathbf{r}_2)$ defined by

$$B_f(\mathbf{r}_1, \mathbf{r}_2) = \langle [f(\mathbf{r}_1) - \mu(\mathbf{r}_1)][f^*(\mathbf{r}_2) - \mu^*(\mathbf{r}_2)] \rangle, \quad (9)$$

is sufficient to describe a stationary random process, where $\mu(\mathbf{r}_i)$ is the expected value of $f(\mathbf{r}_i)$ and $\langle \cdot \rangle$ refers to the ensemble average. A wide-sense stationary (WSS) random process is a system where the variance and mean remain constant and do not vary with time. Any strictly stationary process which has a mean and a covariance is also WSS. If a WSS random process's temporal variance and mean can be approximated by the ensemble's variance and mean, it is said to be ergodic in the variance and mean.

The relation that links the spectral representation to the spatial one is the Wiener-Khinchin theorem. It basically states the power spectral density of a WSS random process is equal to the Fourier transform of the autocovariance function. The PSD $\Phi_f(\boldsymbol{\kappa})$ of f is given by

$$\Phi_f(\boldsymbol{\kappa}) = \left(\frac{1}{2\pi} \right)^3 \int B_f(\mathbf{r}) \exp(-j\boldsymbol{\kappa} \cdot \mathbf{r}) \, d\mathbf{r}, \quad (10)$$

where $\boldsymbol{\kappa}$ is the 3-D angular spatial frequency vector. If a random process $f(\mathbf{r})$ has a slowly varying mean, it cannot be represented by the auto-covariance. If, for small separations r , the process is homogeneous in the mean, it is said to have stationary increments. Accordingly, the 3-D structure function $D_f(\mathbf{r})$ adequately describes this process and is denoted by

$$D_f(\mathbf{r}) = \langle |f(\mathbf{r}_1) - f(\mathbf{r}_1 + \mathbf{r})|^2 \rangle. \quad (11)$$

Furthermore, if the process is homogenous expanding the structure function yields the following convenient relationship to the auto-covariance:

$$\begin{aligned} D_f(\mathbf{r}) &= \langle f^2(\mathbf{r}_1) \rangle + \langle f^2(\mathbf{r}_1 + \mathbf{r}) \rangle - 2 \langle f(\mathbf{r}_1)f(\mathbf{r}_1 + \mathbf{r}) \rangle \\ &= 2 [B_f(0) - B_f(\mathbf{r})]. \end{aligned} \quad (12)$$

If the medium is isotropic, meaning the relationships are the same regardless of the direction, the vector equations can be converted to scalar separation distances. For the isotropic case, the structure function is determined by

$$D_f(r) = 8\pi \int_0^\infty \Phi_f(\kappa) \left[1 - \frac{\sin(\kappa r)}{\kappa r} \right] d\kappa. \quad (13)$$

The inverse relationship is

$$\Phi_f(\kappa) = \frac{1}{4\pi^2\kappa^2} \int_0^\infty \frac{d}{dr} \left[r^2 \frac{d}{dr} D_f(r) \right] \frac{\sin(\kappa r)}{\kappa r} dr. \quad (14)$$

The refractive index 3-D turbulence power spectrum $\Phi_n^K(\kappa, z)$ is a function of both the turbulence along the path and the spatial frequency. The variable z represents the location along the propagation path, and κ denotes the spatial frequencies of the turbulence. The smaller frequencies are bounded by $\kappa_0 = 2\pi/L_0$ where L_0 is the outer scale, representing the largest sizes of turbulence. The larger frequencies are bounded by $\kappa_m = 2\pi/l_0$, where l_0 is the inner scale. As the name suggests, the

inner scale refers to the smallest portions of the turbulence. If the turbulence's spatial frequency is in the range $2\pi/L_0 \leq \kappa \leq 2\pi/l_0$, the turbulence power spectrum can be represented by the Kolmogorov turbulence power spectrum [36]

$$\Phi_n^K(\kappa, z) = 0.033C_n^2(z)\kappa^{-11/3}, \quad (15)$$

where $C_n^2(z)$ is the refractive index structure parameter. The modified von Kármán spectrum $\Phi_n^V(\kappa, z)$ takes the inner and outer scales into account and is represented by [36]

$$\Phi_n^V(\kappa, z) = 0.033C_n^2(z) \frac{\exp\left(-\frac{\kappa^2}{\kappa_m^2}\right)}{(\kappa^2 + \kappa_0^2)^{11/6}}, \quad (16)$$

where $\kappa_m = 2\pi/l_0$ and $\kappa_0 = 2\pi/L_0$. The original von Kármán spectrum does not include the exponential factor for the inner scale. Both spectrums are used in this research depending upon which is appropriate. If the turbulence is limited to the range $2\pi/L_0 \leq \kappa \leq 2\pi/l_0$, the Kolmogorov turbulence power spectrum is used. Otherwise, the von Kármán spectrum is used.

The inner scale plays a large part into determining the scintillation, since these small scale variations break up the wavefront and cause amplitude variations. The inner scale length varies with altitude. Holding the energy dissipation rate constant, the inner scale varies nearly inversely with the air density [85]

$$l_0 \propto \rho^{-3/4}. \quad (17)$$

At ground level, inner scale measurements typically range from 2 mm to 9 mm [85]. A comprehensive study accomplished over White Sands, NM determined the inner scale length increased exponentially from $l_0 = 1$ cm at 5 km to $l_0 = 8$ cm at 19 km [21, 85]. Applying the model in Eq. (17) and $l_0 = 1$ cm at 5 km a model for the inner scale variation with altitude was determined. Since the air pressure at 5 km is approximately 54 kPa, this equates to an air density ρ at 5 km of 0.843 kg/m³. The equation for inner scale used in this research is determined by solving for the constant multiplier

in Eq. (17), leading to

$$\begin{aligned} l_0 &= \frac{C_{l_0}}{\rho^{3/4}} \\ 0.01 &= \frac{C_{l_0}}{0.843^{3/4}} \end{aligned} \quad (18)$$

where the air density is (assuming an ideal gas)

$$\rho = \frac{PM}{RT}, \quad (19)$$

and P is the air pressure in pascals, $M = 0.0289644$ kg/mol is molecular weight of dry air, $R = 8.31447$ is the universal gas constant in J/(mol K), and T is the temperature in Kelvins. Solving for the constant yields $C_{l_0} = 0.0088 \text{ m}^{-5/4} \text{ kg}^{3/4}$, which is used to determine the inner scale for the simulations performed in this research, as shown in Fig. 3.

Large-scale turbulence affects the phase, and following this trend, the largest scale turbulence affects the wavefront tilt (i.e. largest scale phase effects) and causes laser beams to randomly wander. This outer scale denoted by L_0 varies with altitude and tends to be an ellipsoidal function of zenith angle. Near the ground $L_0 \approx 0.4h$, where h denotes the altitude, as shown in Fig. 3. At higher altitudes, the outer scale is determined by the vertical outer scale and the horizontal outer scale. The vertical outer scale $L_{0\text{vert}}$ typically varies from 10 m to 70 m [21]. The horizontal outer scale is very large. Aircraft measurements have determined it can be over hundreds of kilometers [85]. For horizontal propagation, an infinite outer scale is used in this research. However, for slant ranges, the outer scale is determined by taking a slice through the vertical outer scale

$$L_0 = \frac{L_{0\text{vert}}}{\cos(\xi)}. \quad (20)$$

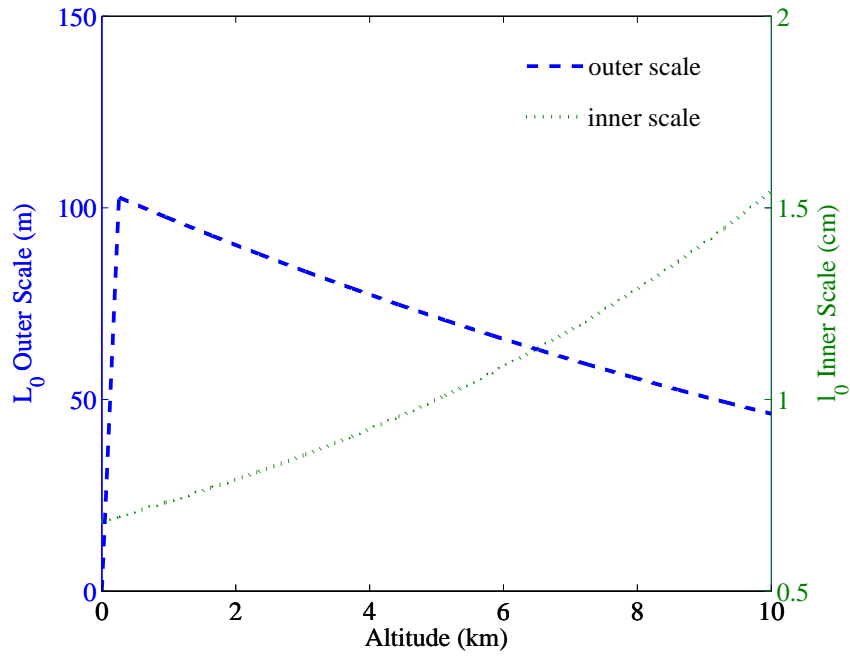


Figure 3: This plot shows the inner scale as it varies with altitude calculated from Eq. (17), calibrated by $l_0 = 1$ cm at 5 km altitude from measurements taken at White Sands Missile Range, NM. The outer scale L_0 was determined from the approximation of $L_0 \approx 0.4h$ and the measurements at White Sands [21].

2.2.2 *Turbulence models and moments.* The refractive index structure parameter characterizes the strength of atmospheric turbulence. There are many different models used to describe the effects of atmospheric turbulence as they vary with altitude. A very common model that is used throughout this work to describe the turbulence strength $C_n^2(h)$ is the Hufnagel-Valley model. This turbulence profile is described by [66]

$$C_n^2(h) = 5.94 \times 10^{-53} \left(\frac{v}{27}\right)^2 h^{10} \exp\left(-\frac{h}{1000}\right) + 2.7 \times 10^{-16} \exp\left(-\frac{h}{1500}\right) + A \exp\left(-\frac{h}{100}\right), \quad (21)$$

where h is the height above the ground in meters, A in $\text{m}^{-2/3}$ sets the turbulence strength near the ground, and v represents the high-altitude root-mean square (rms) wind speed in m/s. To change the strength of turbulence at high altitudes, the v term is typically varied. This research uses the common value for A of $1.7 \times 10^{-14} \text{m}^{-2/3}$ and sets the v variable to 21 m/s which is often referred to as either HV-21 or HV_{5/7}. The 5 and 7 in HV_{5/7} refer to a coherence diameter of $r_0 = 5$ cm and an isoplanatic angle of $\theta_0 = 7 \mu\text{rad}$ at a wavelength of $0.5 \mu\text{m}$ for zenith imaging through the atmosphere.

The rms wind speed v in Eq. (21) is calculated from [2]

$$v = \left[\frac{1}{15 \times 10^3} \int_{5 \times 10^3}^{20 \times 10^3} V^2(h) dh \right]^{1/2} \quad (22)$$

and substituted back into Eq. (21). The propagation path moments μ_m frequently appear in equations that describe specific atmospheric turbulence effects. The full moments for ground-to-space propagation are [31, 69]

$$\mu_m \equiv \int_0^\infty C_n^2(z) z^m dz = \sec^{m+1}(\xi) \int_0^\infty C_n^2(h) h^m dh, \quad (23)$$

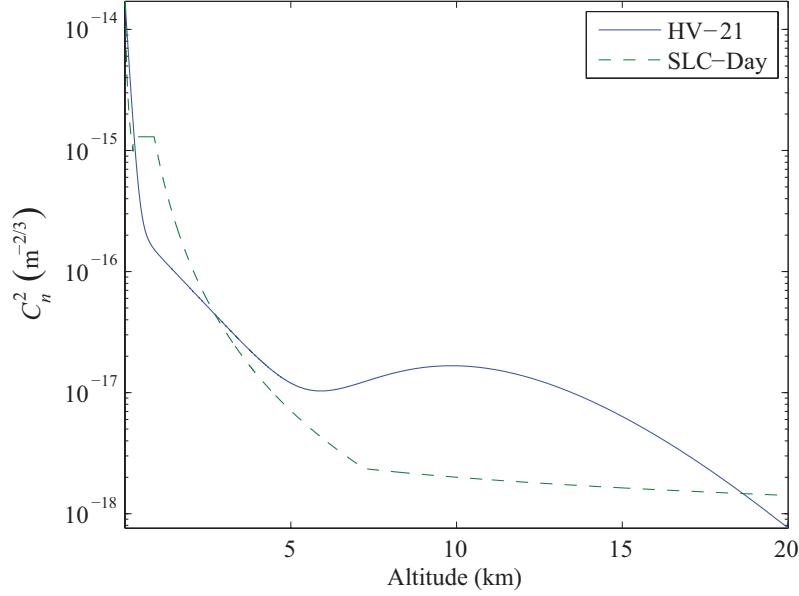


Figure 4: HV-21 and the SLC-Day strength of turbulence profile models.

where ξ is the zenith angle. For horizontal propagation or constant turbulence strength, the moments simplify to

$$\mu_m = C_n^2 L^{(m+1)} / (m + 1), \quad (24)$$

where L is the propagation path length. For a slant propagation path length L through the atmosphere to a height H , where $L = \sec(\xi) H$, the turbulence moments can be broken into these partial moments [69]

$$\mu_m^- \equiv \int_0^L C_n^2(z) z^m dz = \sec^{m+1}(\xi) \int_0^H C_n^2(h) h^m dh, \quad (25)$$

$$\mu_m^+ \equiv \int_L^\infty C_n^2(z) z^m dz = \sec^{m+1}(\xi) \int_H^\infty C_n^2(h) h^m dh. \quad (26)$$

The equations for μ_m^- and μ_m^+ above apply to a flat-earth model. The curvature of the earth must be included when propagating long distances at low elevation angles, especially when propagating horizontally. Since light travels along geodesics,

the propagation path cuts through turbulence at a lower altitudes, causing stronger turbulence in the middle of the path. To consider these differences, the values for h in the turbulence profiles would include $h(z)$ as a function of the propagation distance location z [69]. For the propagations and profiles modeled in this work, the difference in the strength of turbulence $C_n^2(z)$ for flat earth and curved earth models are negligible.

2.2.3 Atmospheric phase parameters. Diffraction and turbulence significantly affect laser beam propagation. Whether the beam propagates through air or through space, the beam diffracts and spreads as it propagates. Through the air, thermal mixing of the air causes random index of refraction variations leading to random phase fluctuations of optical beams. These random fluctuations cause laser beams to spread, randomly wander, and scintillate.

These turbulence effects also limit the resolution of imaging systems. Without atmospheric turbulence, the resolution of an imaging system improves as the receiver aperture increases, commonly referred to as the diffraction-limited resolution. In turbulence, the imaging system is approximately limited to the diffraction-limited resolution of a r_0 -diameter aperture. For a plane-wave source, this coherence diameter (a.k.a. Fried parameter) $r_{0,pw}$ is [69]

$$r_{0,pw} = \left[0.423k^2 \int_0^L C_n^2(z) dz \right]^{-3/5} \quad (27)$$

$$= (0.423k^2 \mu_0^-)^{-3/5} \quad (28)$$

and for a point source (spherical wave), $r_{0,sw}$ is defined as

$$r_{0,sw} = \left[0.423k^2 \int_0^L C_n^2(z) \left(\frac{z}{L} \right)^{5/3} dz \right]^{-3/5} \quad (29)$$

$$= \left(0.423k^2 \mu_{5/3}^- \right)^{-3/5} . \quad (30)$$

where $k = 2\pi/\lambda$ is the wave number and λ is the optical wavelength. The isoplanatic angle θ_0 defines the angular separation between beams where the higher order phase effects are relatively correlated. This angle is used to determine the maximum angular separation between a reference beam and the transmission beam to measure the higher-order phase effects. It is defined as [69]

$$\theta_0 = \left[2.91k^2 \int_0^L C_n^2(z)(L-z)^{5/3} dz \right]^{-3/5}. \quad (31)$$

In each case the light propagates from the source at $z = 0$ to the receiver at $z = L$ [27].

2.2.4 Atmospheric beam wander and beam spreading. In free-space laser communications when the laser beam wanders off the receiver due to turbulence, a fade occurs. For constant C_n^2 (as in horizontal propagation), the Gaussian-beam wander was characterized by Andrews and Phillips by the second moment of the beam's hot-spot displacement for the infinite outer scale case as [2]

$$\langle r_c^2 \rangle = 2.42C_n^2L^3W_0^{-1/3} {}_2F_1\left(\frac{1}{3}, 1; 4; 1 - |\Theta_0|\right), \quad (32)$$

where ${}_2F_1$ is the hypergeometric function, Θ_0 is defined in Eq. (5). The equation can be simplified for a collimated beam

$$\begin{aligned} \langle r_c^2 \rangle &= 2.42C_n^2L^3W_0^{-1/3} \\ &= 0.0657 \text{ m}^2 \end{aligned} \quad (33)$$

and for a focused beam

$$\begin{aligned} \langle r_c^2 \rangle &= 2.72C_n^2L^3W_0^{(-1/3)}, \\ &= 0.0738 \text{ m}^2, \end{aligned} \quad (34)$$

where W_0 is the effective beam radius and L is the propagation length. The numeric answer given above is for an air-to-air 100 km path with $C_n^2 = 10^{-17} \text{ m}^{-2/3}$ for an infinite outer scale (i.e. Kolmogorov turbulence model) and $W_0 = 2.5 \text{ cm}$. These same parameters are used in simulations in subsequent chapters. For the uplink channel, the rms beam wander is [2]

$$\sqrt{\langle r_c^2 \rangle} = 0.73H \sec(\xi) \left(\frac{\lambda}{2W_0} \right) \left(\frac{2W_0}{r_0} \right)^{5/6}, \quad (35)$$

where ξ is the zenith angle.

In order to calculate the centroid location probability density function (PDF), let the received beam's centroid Cartesian components be x_c and y_c . If the turbulence is isotropic, one can assume that x_c and y_c are independent and identically distributed random variables with a Gaussian PDF. The PDF of r_c can be calculated by first determining the x and y contributions to the PDF and using those in a jointly Gaussian PDF. Since the x and y centroid variances, $\sigma_{x_c}^2$ and $\sigma_{y_c}^2$, are equal, they can be determined by

$$\sqrt{\langle r_c^2 \rangle} = \sqrt{\sigma_{x_c}^2 + \sigma_{y_c}^2} = \sqrt{2\sigma_{x_c}^2}, \quad (36)$$

resulting in $\sigma_{x_c}^2 = \sigma_{y_c}^2 = \langle r_c^2 \rangle / 2$. Using the x and y centroid variances, the centroid location PDF takes the form

$$f_{x_c y_c}(x, y) = \frac{1}{2\pi\sigma_{x_c}\sigma_{y_c}} \exp \left\{ -\frac{1}{2} \left[\left(\frac{x}{\sigma_{x_c}} \right)^2 + \left(\frac{y}{\sigma_{y_c}} \right)^2 \right] \right\} \quad (37)$$

$$= \frac{1}{2\pi\sigma_{x_c}^2} \exp \left(-\frac{x^2 + y^2}{2\sigma_{x_c}^2} \right). \quad (38)$$

For the 100 km $C_n^2 = 10^{-17} \text{ m}^{-2/3}$ air-to-air path $\sigma_{x_c}^2 = \sigma_{y_c}^2 = \langle r_c^2 \rangle / 2 = 0.033 \text{ m}^2$ and the standard deviation is $\langle r_c^2 \rangle^{1/2} = 0.256 \text{ m}$.

Now computing the PDF in terms of $r = (x^2 + y^2)^{1/2}$ requires a transformation of the random variables x and y to r [57]. The cumulative density function (CDF) is

determined by

$$F_r(r) = 1 - \exp\left(-\frac{r^2}{2\sigma_{x_c}^2}\right), \quad r \geq 0 \quad (39)$$

Taking the derivative of the CDF yields the PDF

$$f_r(r) = \frac{r}{\sigma_{x_c}^2} \exp\left(-\frac{r^2}{2\sigma_{x_c}^2}\right), \quad r \geq 0 \quad (40)$$

where $\sigma_{x_c}^2 = \sigma_{y_c}^2 = \langle r_c^2 \rangle / 2$. The turbulence-induced short-term beam radius W_{ST} at the receiver combined with the random centroid locations determines the average power at the receiver. This radius for a collimated beam is [2]

$$W_{ST} = W \sqrt{1 + 1.64C_n^2 k^{7/6} L^{11/6} \Lambda^{5/6} \left[1 - 0.66 \left(\frac{\Lambda_0^2}{1 + \Lambda_0^2}\right)^{1/6}\right]} \quad (41)$$

while for a focused beam the radius is [2]

$$W_{ST} = W \sqrt{1 + 0.43C_n^2 k^{7/6} L^{11/6} \Lambda^{5/6}}, \quad (42)$$

where $\Lambda = z / (kW^2)$. For the 100 km air-to-air path the beam-spreading factor W_{ST}/W does not change much with W_0 . Figure 5 shows the maximum beam-spreading occurs when $W_0 = 0.263$ m with a beam spreading factor of $W_{ST}/W = 1.14$. In this case, for any diameter beam, most of the beam spreading is caused by diffraction not turbulence.

The long-term spot size W_{LT} is calculated using the short-term spot size and the random centroid locations to determine the average power profile at the receiver plane. The analytic long-term field follows a Gaussian shape given by

$$U(x, y) = \frac{1}{2\pi W_{LTx} W_{LTy}} \exp\left[-0.5 \left(\frac{x^2}{W_{LTx}^2} + \frac{y^2}{W_{LTy}^2}\right)\right], \quad (43)$$

$$W_{LTx} = W_{LTy} = \frac{W_{LT}}{2}, \quad (44)$$

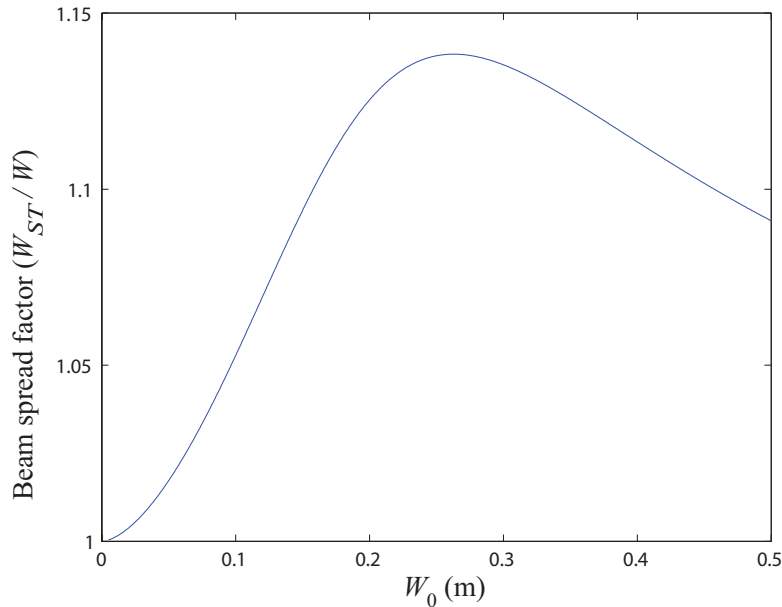


Figure 5: Turbulence induced short-term beam spread for the 100 km air-to-air path with $C_n^2 = 10^{-17} \text{ m}^{-2/3}$.

where [2]

$$W_{LT} = \sqrt{W_{ST}^2 + \langle r_c^2 \rangle} \quad (45)$$

$$= W \sqrt{1 + 1.33\sigma_R^2 \Lambda^{5/6}}. \quad (46)$$

A Monte-Carlo simulation with random draws of centroid locations was performed to verify Eq. (46). As shown in Fig. 6, the simulation matched very closely to the Gaussian profile and the theoretical spot size, since W_{LT} is determined by the W_{ST} and $\langle r_c^2 \rangle$. This also confirms that the PDF used to determine the centroid locations is consistent with the definition.

2.2.5 Beam wandering and spreading effects on laser communication. Next, the beam wandering is combined with the beam spreading to determine the effect on the received power. For this example, the receiver has a circular aperture with a radius of 5 cm, and all the light collected by the aperture is detected. The cumulative probability of collected power is used to determine the probability of fading. The

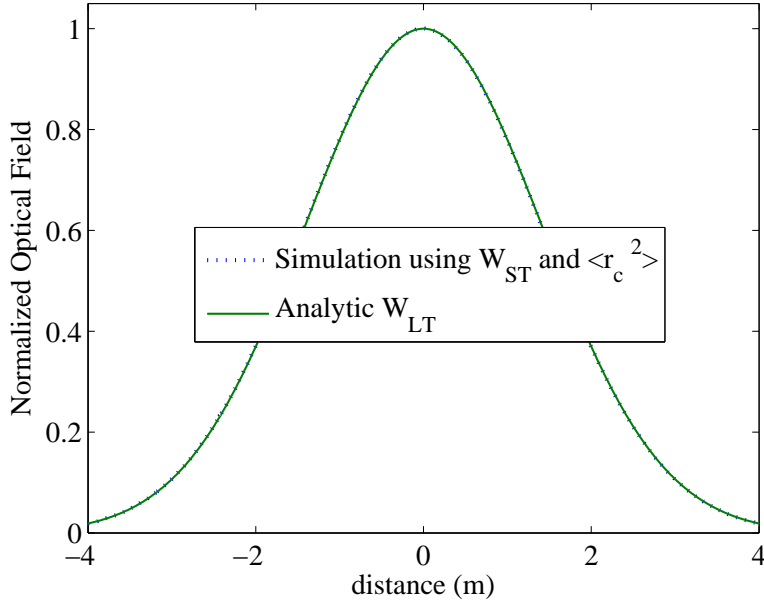


Figure 6: Long-term optical field profile for a $W_0 = 2.5$ cm and a constant $C_n^2 = 10^{-17} \text{ m}^{-2/3}$ air-to-air 100 km path. Plotted using short-term spot size and random centroid locations (using rms beam wander) in a 1000 draw Monte-Carlo simulation and compared to analytic long-term spot size.

highest power in this plot corresponds to a beam received on-axis. Conversely, the lower received powers occur as the beam wanders off axis, corresponding to a fade in a laser communication link. The probability is determined from the hot-spot location PDF and the beam spreading effects mentioned earlier.

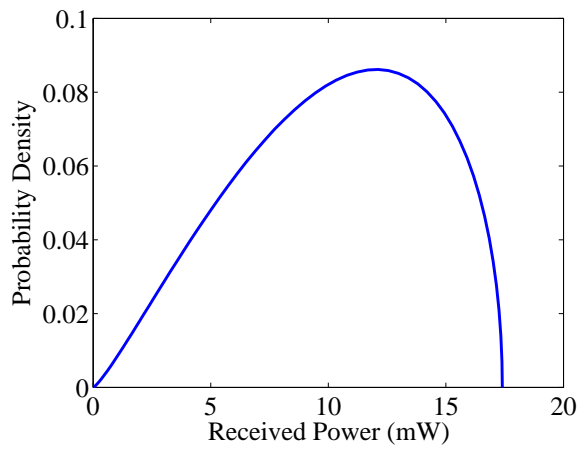
Taking beam spreading and wandering effects into account, it is suspected a smaller W_0 would improve signal fading for the long propagation path of the air-to-air 100-km path. For the case of $W_0 = 10$ cm, the following results were found $W_{ST} = 53$ cm and $\langle r_c^2 \rangle = 521 \text{ cm}^2$. The beam wander for $W_0 = 10$ cm is less than for the $W_0 = 0.05$ cm case, although the received beam size played a much larger factor. The larger the transmit aperture, the smaller the beam size at the receiver. For these smaller received beams, the beams walk off the receiver and deep fades occur. For the larger received beams the maximum power received is less, but the fades are not as deep since the beam does not completely walk off the receiver.

Figures 7 and 8 show how this affects the collected power PDF and CDF. For $W_0 = 10$ cm, the probability that the received power was less than a -47 dBm (150 photons at 1 GBit/sec) threshold was over 10^{12} times higher than the $W_0 = 5$ cm case and 10^{48} times higher than the $W_0 = 2.5$ cm case. To achieve a fade probability of less than 10^{-10} , the $W_0 = 10$ cm transmitter required a threshold 60 times lower than the $W_0 = 5$ cm case and 360 times lower than the $W_0 = 2.5$ cm case. The lower the required threshold, the less the margin for error, leading to deeper fades at the receiver.

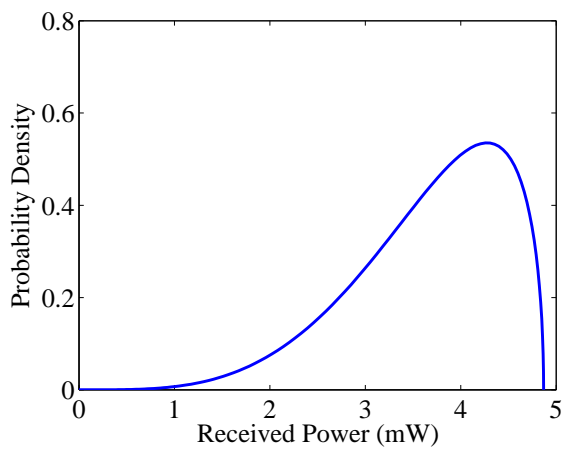
Another approach would be to defocus the beam, spreading the beam out at the receiver and reducing the fades. This effect can be illustrated by comparing the results for a collimated beam and a focused beam. For this long-propagation example, the difference between the beam size at the receiver is still significant enough to affect the results. As expected, the collimated beams performed better, resulting in less fading than the focused beam as shown in Figure 8 for the two $W_0 = 5$ cm cases.

For long-distance propagations, the beam width steadily increases as it propagates due to diffraction. The turbulence also spreads the beam width even more, but the primary cause for the extended turbulence scenario is diffraction. Narrow beam widths tend to wander more than wide beam widths since the average tilt across these narrow beams is higher. Referring back to Figure 2 on beam spread due to diffraction, it is clear that if the strength of turbulence varies over the path, this beam width affects the turbulence-induced beam wander and beam spread. Turbulence-induced phase tilts at the beginning of the propagation result in larger beam wander due to the long lever arm of the turbulence and small beam size at the transmitter.

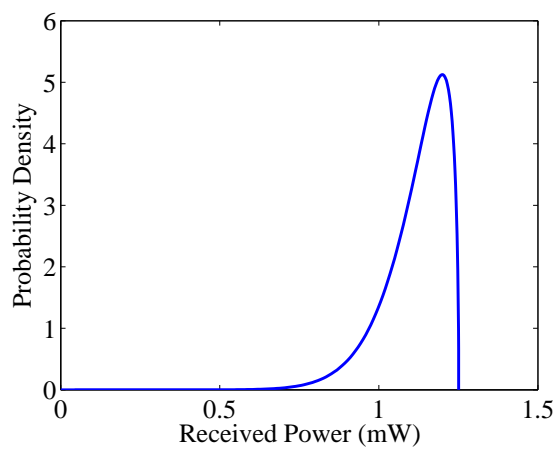
One phenomenon not considered in this analysis is the beam's angle of arrival (AOA) variance. Typically the receiver will have a large collection optic that focuses the beam onto the detector. As the AOA varies, the irradiance on the detector also



(a)



(b)



(c)

Figure 7: 100 km Air-to-Air Scenario. Collected power PDF in milliwatts for (a) $W_0 = 10$ cm; (b) $W_0 = 5$ cm; and (c) $W_0 = 2.5$ cm.

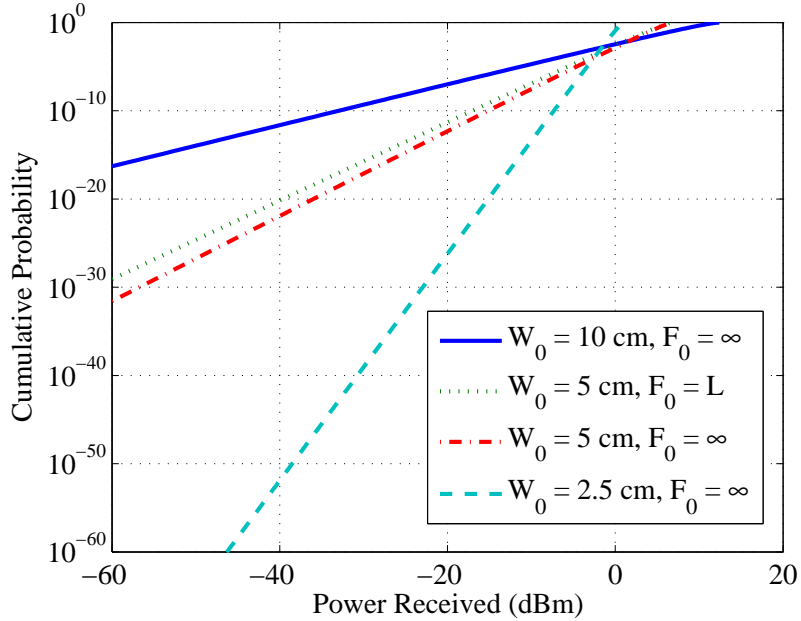


Figure 8: 100 km Air-to-Air Scenario. Collected power CDF for $W_0 = 10$, $W_0 = 5$, and $W_0 = 2.5$ cm. A cumulative probability of 1 is reached at the maximum collected power.

varies. The Rx AOA variance in radians squared is [69]

$$T_t^2 = \frac{6.08}{D^{1/3}L^2} \int_0^L z^2 C_n^2(z) dz, \quad (47)$$

where D is the receiver diameter. The rms image jitter is just the focal length times the rms angle of arrival, fT_t , which determines an additional received power variation. This image jitter decreases as the receiver optic size increases, since the variances in the phase average over a larger optic. Small receiver optics may encounter large image jitter due to turbulence and usually require a receiver tracker. The more the incident light is angularly off-axis, the less power is received at the detector.

2.3 Amplitude effects

There is another critical effect that the model in the previous section of beam spreading and wandering does not include that must be considered when determin-

ing signal fading. That effect is beam's temporal and spatial intensity variance (or scintillation). Not only does the beam spread out, it also varies in intensity significantly over the entire beam. These intensity variations increase with propagation distance through the turbulence and are more significant the further off the beam center. These variations are also more significant for wider beams than for narrower beams, leading to more pronounced fluctuations as the beam widens due to diffraction. To determine the optimum beam size, diffraction and the turbulence effects of beam wander, beam spread, *and scintillation* must be considered.

As the beam propagates, the phase aberrations cause intensity variations at the receiver. These effects are particularly important in a laser communication system, since these variations can cause fades and bit errors. This turbulence effect can be characterized by the log-amplitude variance, often referred to as the Rytov number \mathcal{R} , as it is calculated using the Rytov approximation. The Rytov-theory expressions for the scintillation discussed here are only valid for log-amplitude variances less than 0.25. Beyond this value, the scintillation begins to saturate. This saturation value is typically between 0.3 and 0.4 [69]. The plane-wave log-amplitude variance σ_χ^2 at the receiver is [2]

$$\sigma_{\chi,pw}^2 = 0.5631k^{7/6} \int_0^L C_n^2(z)(L-z)^{5/6} dz, \quad (48)$$

and the spherical-wave log-amplitude variance is

$$\sigma_{\chi,sw}^2 = 0.5631k^{7/6} \int_0^L C_n^2(z)(z/L)^{5/6}(L-z)^{5/6} dz. \quad (49)$$

Specifically, for a plane-wave space-to-ground propagation [2]

$$\sigma_{\chi,pw}^2 = 0.5631k^{7/6} \mu_{5/6}, \quad (50)$$

while for ground-to-space propagation

$$\sigma_{\chi,pw}^2 = 0.5631k^{7/6} \sec^{11/6}(\xi) \int_0^H C_n^2(h)(H-h)^{5/6} dh, \quad (51)$$

and for horizontal propagation with a uniform C_n^2 profile

$$\sigma_{\chi,pw}^2 = 0.3071k^{7/6}C_n^2L^{11/6}. \quad (52)$$

The spherical wave Rytov number is

$$\mathcal{R}_{sph} = 0.5631k^{7/6} \int_0^L C_n^2(z)(L-z)^{5/6} \left(\frac{z}{L}\right)^{5/6} dz \quad (53)$$

$$\approx \sigma_{\chi,sw}^2 \quad \mathcal{R}_{sph} \lesssim 0.25. \quad (54)$$

For weak turbulence, the spherical wave Rytov number \mathcal{R}_{sph} is equal to the log-amplitude variance $\sigma_{\chi,sw}^2$. Since the scintillation saturates with strong turbulence, the Rytov number does not equal the log-amplitude variance for $\mathcal{R}_{sph} \gtrsim 0.25$.

The detector at the receiver ultimately measures the irradiance. Under weak turbulence, the normalized irradiance variance (referred to as the scintillation index, i.e. the irradiance variance over the average irradiance $I/\langle I \rangle$), is [2]

$$\sigma_{\frac{I}{\langle I \rangle}}^2(r) = \frac{\langle I^2(r) \rangle}{\langle I(r) \rangle^2} - \frac{\langle I(r) \rangle^2}{\langle I(r) \rangle^2} = \frac{\langle I^2(r) \rangle}{\langle I(r) \rangle^2} - 1 \quad (55)$$

$$= \exp[\sigma_{\chi}^2(r)] - 1 \quad (56)$$

$$\cong 4\sigma_{\chi}^2(r) \quad \text{for } \sigma_{\chi}^2 < 0.25 \quad (57)$$

$$\cong \sigma_{\ln I}^2(r) \quad \text{for } \sigma_{\chi}^2 < 0.25, \quad (58)$$

where r is the radial distance from the optical axis and $\sigma_{\ln I}^2(r)$ is the log-irradiance variance. Given this relationship, the plane-wave scintillation index is

$$\sigma_{\ln I}^2 = 2.251k^{7/6} \int_0^L C_n^2(z)(L-z)^{5/6} dz, \quad (59)$$

and for spherical-wave propagation, it is

$$\sigma_{\ln I}^2 = 2.251k^{7/6} \int_0^L C_n^2(z)(z/L)^{5/6}(L-z)^{5/6} dz. \quad (60)$$

Andrews and Phillips define the plane-wave scintillation index for a constant C_n^2 profile as the Rytov variance σ_R^2 [2]. From the above relations, the Rytov variance is defined as

$$\sigma_R^2 = 1.23k^{7/6}C_n^2L^{11/6}. \quad (61)$$

For example, the Rytov variance for the air-to-air 100 km path for $C_n^2 = 10^{-17} \text{ m}^{-2/3}$ is $\sigma_R^2 = 0.924$.

2.3.1 Strong fluctuation theory. The previous section's relations for amplitude and intensity variations were valid for weak turbulence only. They were computed through Rytov theory. In strong turbulence, the phase variance continues to increase, while the scintillation or variance in the amplitude and irradiance saturates. There are multiple theories used to predict the behavior as the Rytov number increases [2]. Extended Rytov theory describes the scintillation by breaking it up into large- and small-scale amplitude variations. These irradiance variances use the gamma-gamma distribution to describe the irradiance variation PDF. The irradiance variance due to turbulence for spherical, planar, and Gaussian beams can be described by [2]

$$\sigma_I^2(L) = \exp(\sigma_{\ln X}^2 + \sigma_{\ln Y}^2) - 1, \quad (62)$$

where $\sigma_{\ln X}^2$ and $\sigma_{\ln Y}^2$ are the variances in the small- and large-scale irradiance fluctuations, respectively. The equations for these variances differ depending upon the type of source. In the limiting case of Kolmogorov turbulence (i.e $l_0 = 0$ and $L_0 = \infty$) for spherical waves, the large and small-scale log variances are represented by [2]

$$\sigma_{\ln X}^2 = \frac{0.20\sigma_R^2}{\left(1 + 0.19\sigma_R^{12/5}\right)^{7/6}} \approx \begin{cases} 0.20\sigma_R^2, & \sigma_R^2 \ll 1, \\ \frac{1.37}{\sigma_R^{4/5}}, & \sigma_R^2 \gg 1. \end{cases} \quad (63)$$

$$\sigma_{\ln Y}^2 = \frac{0.20\sigma_R^2}{\left(1 + 0.23\sigma_R^{12/5}\right)^{5/6}} \approx \begin{cases} 0.20\sigma_R^2, & \sigma_R^2 \ll 1, \\ \ln 2, & \sigma_R^2 \gg 1. \end{cases} \quad (64)$$

For planar wavefronts these equations become [2]

$$\sigma_{\ln X}^2 = \frac{0.49\sigma_R^2}{\left(1 + 1.11\sigma_R^{12/5}\right)^{7/6}} \approx \begin{cases} 0.49\sigma_R^2, & \sigma_R^2 \ll 1, \\ \frac{0.43}{\sigma_R^{4/5}}, & \sigma_R^2 \gg 1. \end{cases} \quad (65)$$

$$\sigma_{\ln Y}^2 = \frac{0.51\sigma_R^2}{\left(1 + 0.69\sigma_R^{12/5}\right)^{5/6}} \approx \begin{cases} 0.51\sigma_R^2, & \sigma_R^2 \ll 1, \\ \ln 2, & \sigma_R^2 \gg 1. \end{cases} \quad (66)$$

2.3.2 Temporal effects. To represent the temporal statistics accurately, the temporal frequency of the turbulence must be modeled appropriately. The two quantities used to describe the turbulence frequency are the Greenwood frequency f_G and the Tyler frequency f_T . They are given by [66]

$$f_G = 0.2542 \left[\int_0^L C_n^2(z) |V(z)|^{5/3} dz \right]^{3/5} \quad (67)$$

$$= 0.426 \frac{|V|}{r_0} \quad (68)$$

and

$$f_T = 0.0586 D^{-1/6} k \left[\int_0^L C_n^2(z) |V(z)|^2 dz \right]^{1/2} \quad (69)$$

$$= 0.0902 \left(\frac{r_0}{D}\right)^{1/6} \left(\frac{|V|}{r_0}\right), \quad (70)$$

respectively. These are the temporal power spectrum “break frequencies.” A majority of the tilt jitter is below the Tyler frequency. Most of the frequencies for the higher- and lower-order phase disturbances are below the Greenwood frequency.

The wind velocity $V(h)$ in (21) is frequently described by the Bufton wind model [2]

$$V(h) = \omega_s h + V_g + 30 \exp \left[- \left(\frac{h - 9400}{4800} \right)^2 \right], \quad (71)$$

where V_g is the ground wind speed and ω_s is the slew rate of a ground transmitter (Tx) tracking an aerial receiver (Rx).

2.4 Layered atmosphere model

Simulations are often used to study atmospheric turbulence effects on imaging, communication, and beam-projection systems. Analytic solutions to wave propagation oftentimes require assumptions that limit the validity of the results, like the Rytov approximation that limits the turbulence to weak fluctuations. Not only that, adaptive optics (AO) systems and diversity techniques such as multiple-transmitter performance cannot be calculated in closed form. The turbulence effects in these simulations can be represented by optical field screens placed along the propagation path having the appropriate statistics.

If the layered model matches the refractive index spectrum and the phase variance of the propagation path, it can be used in analytic calculations, computer simulations, and experiments. The layers are chosen to represent the continuous model as closely as possible so that several low-order moments of the layered model match the continuous model

$$\int_0^L C_n^2(z) z^m dz = \sum_{i=1}^N C_{n_i}^2 z_i^m \Delta z_i, \quad (72)$$

where N is the number of phase screens being used and $C_{n_i}^2$ is the effective turbulence strength, Δz_i is the turbulence layer thickness, and z_i is the location of the i^{th} screen [66]. The atmospheric parameters for the layered turbulence model are

$$r_{0,pw} = \left(0.423k^2 \sum_{i=1}^N C_{n_i}^2 \Delta z_i \right)^{-3/5}, \quad (73)$$

$$r_{0,sw} = \left[0.423k^2 \sum_{i=1}^N C_{n_i}^2 \left(\frac{z_i}{L} \right)^{5/3} \Delta z_i \right]^{-3/5}, \quad (74)$$

$$\sigma_{\chi,pw}^2 = 0.5631k^{7/6} \sum_{i=1}^N C_{n_i}^2 (L - z_i)^{5/6} \Delta z_i, \quad (75)$$

$$\sigma_{\chi,sw}^2 = 0.5631k^{7/6} \sum_{i=1}^N C_{n_i}^2 \left(\frac{z_i}{L} \right)^{5/6} (L - z_i)^{5/6} \Delta z_i, \quad (76)$$

$$\theta_0 = \left[2.91 \sum_{i=1}^N C_{n_i}^2 (L - z_i)^{5/3} \Delta z_i \right]^{-3/5}, \quad (77)$$

which are analogous to the continuous model versions in Eqs. (28), (30), (48), (49), and (31). The full path r_0 can be determined by the phase screens' r_{0_i} along the path by

$$r_{0_{sw}}^{-5/3} = \sum_{i=1}^N r_{0_i}^{-5/3} (z_i/L)^{5/3}. \quad (78)$$

The screen r_{0_i} value is related to C_n^2 by

$$r_{0_i}^{-5/3} = 0.423k^2 C_n^2(z_i) \Delta z_i. \quad (79)$$

Equations (73) - (77) can be written in terms of r_{0_i} , which simplifies the method of choosing screen properties and screen locations.

To determine the temporal performance for layered models in terms of the Greenwood and Tyler frequencies use

$$f_G = 0.2542k^{6/5} \left[\sum_{i=1}^N C_n^2(z_i) |V(z_i)|^{5/3} \Delta z_i \right]^{3/5} \quad (80)$$

and

$$f_T = 0.0586kD^{-1/6} \left[\sum_{i=1}^N C_n^2(z_i) |V(z_i)|^2 \Delta z_i \right]^{1/2}, \quad (81)$$

respectively.

Many methods have been developed to generate phase screens. The methods can be broken into two mathematical approaches. The first approach represents the wavefront phase with a 2-dimensional rectangular grid of points — a sampled-based approach. In the second approach, the screen is represented as a sum of orthogonal basis functions or a modal basis. The most common method is the sample-based screen representation in which the fast Fourier transform (FFT) is used to compute the screen realizations. The FFT technique is direct and computationally efficient. The problem with FFT based methods is that the energy of low spatial frequencies in the screen is under-represented. The low spatial frequencies (e.g., tilt) contain a large fraction of the power for atmospheric-turbulence-induced-wavefront perturbations. A modal-based approach allows for much better low frequency representation [48,66,83]. Other FFT techniques with low-order boost (such as sub-harmonic or Zernike) work well for static simulations but large screens must be created (and stored) for long time series simulations due to discontinuities at the edges.

The Fourier-series (FS) phase screen generation approach allows flexibility in choosing the lowest and highest spatial frequencies sampled independent of the phase screen grid sampling. The modal method used here follows Welsh's development based on the FS [83]. A FS expansion of the wavefront phase over a square area is used as the basis for representing the phase screen. This approach much more accurately represents the low spatial frequencies than the sample-based approach. The modal phase screen is defined for all space and need only be evaluated at the grid points of interest. Shifting the phase screen to non-integer multiples of samples is as easy as evaluating the FS on the shifted grid, using the same FS coefficients. This approach is particularly effective since the fields of the multiple widely spaced beams must be

calculated over long periods of time. Here, *logarithmically* spaced frequencies are used, as recommended in an MZA report by Magee [50].

The FS expansion can be approximated by truncating the summations to a finite number of terms. The truncated expansion for the phase is [83]

$$\begin{aligned}
\hat{\phi}(\mathbf{x}) &= \sum_{n=-(N-1)}^{N-1} \sum_{n'=-(N-1)}^{N-1} c_{n,n'}^{\phi} \exp \left\{ j2\pi \left(\frac{nx}{D_p} + \frac{n'y}{D_p} \right) \right\} \\
&= 2\text{Re} \left[\sum_{n=0}^{N-1} \sum_{n'=0}^{N-1} c_{n,n'}^{\phi} \exp \left\{ j2\pi \left(\frac{nx}{D_p} + \frac{n'y}{D_p} \right) \right\} \right. \\
&\quad \left. + \sum_{n=1}^{N-1} \sum_{n'=-1}^{-1} c_{n,n'}^{\phi} \exp \left\{ j2\pi \left(\frac{nx}{D_p} + \frac{n'y}{D_p} \right) \right\} \right], \quad (82)
\end{aligned}$$

where the phase is represented in a square of dimension D_p and $c_{n,n'}^{\phi}$ is the FS coefficient for the spatial frequency $\mathbf{f} = \hat{x}n/D_p + \hat{y}n'/D_p$. The terms \hat{x} and \hat{y} are the x - and y -directed unit vectors, and x and y are the components of the spatial vector \mathbf{x} . The continuous model atmospheric parameters are matched to the layered turbulence model for the isoplanatic angle θ_0 , Rytov number \mathcal{R} , and coherence diameter r_0 .

2.4.1 PDF of the scintillation. The irradiance variations at the receiver, also called scintillation, include temporal variations as well as spatial variations, but for now, only the spatial variations are considered. In Section 5.4.2, the PDFs are calculated for different scenarios in temporal simulations. Many atmospheric turbulence experiments under weak turbulence conditions have shown that the natural log of the intensity is approximated by a Gaussian distribution, i.e. [56]

$$f(\ell) = \frac{1}{\sqrt{2\pi\sigma_{\ell}^2}} \exp[-(\ell - \langle \ell \rangle)^2/2\sigma_{\ell}^2] \quad (83)$$

$$= \frac{1}{\sqrt{2\pi\sigma_{\ell}^2}} \exp[-(\ell + \sigma_{\ell}^2/2)^2/2\sigma_{\ell}^2]. \quad (84)$$

Above, $\ell = \ln(I/\langle I \rangle)$ is the log intensity, I is the optical intensity at a point, and σ_{ℓ}^2 is the variance of the log intensity. After performing a transformation of random

variables, Eq. (84) takes on the familiar lognormal PDF

$$f(I) = \frac{1}{\sqrt{2\pi\sigma_\ell^2}} \frac{\langle I \rangle}{I} \exp\left[-\frac{[\ln(I/\langle I \rangle) + \sigma_\ell^2/2]^2}{2\sigma_\ell^2}\right], \quad (85)$$

where the log-intensity mean is $\langle \ell \rangle = -\sigma_\ell^2/2$. The log intensity variance follows directly from the log-amplitude variance which depends upon the strength of the optical turbulence along the path. Therefore, for a uniform horizontal path, as shown earlier, the on-axis log intensity variance is

$$\sigma_{\ln I}^2 = \sigma_R^2 = 4\sigma_\chi^2 = \begin{cases} 1.23C_n^2 k^{7/6} L^{11/6}, & \text{plane-wave} \\ 0.496C_n^2 k^{7/6} L^{11/6}, & \text{spherical wave} \end{cases}. \quad (86)$$

The intensity variations across the receiver pupil were characterized in Andrews and Phillips' book by the following general expression for the scintillation index of a Gaussian beam [2] :

$$\sigma_{\ln I}^2(r, L) = 3.62k^{7/6} L^{5/6} \Lambda^{5/6} \frac{r^2}{W^2} \int_0^L C_n^2(z) (1 - z/L)^{5/3} dz, \quad r < W \quad (87)$$

in general and

$$\sigma_{\ln I}^2(r, L) = 1.11\sigma_R^2 \Lambda^{5/6} \frac{r^2}{W^2}, \quad r < W \quad (88)$$

for a constant- C_n^2 path. It is clear from these expressions that scintillation increases with distance from the beam center.

Another PDF used to model the variance in the intensity due to stronger atmospheric turbulence conditions is the gamma-gamma PDF. The gamma-gamma PDF was developed under the assumption that large- and small-scale irradiance fluctuations are governed by the following gamma distributions [2]

$$p_X(X) = \frac{(\alpha X)^\alpha}{X \Gamma(\alpha)} \exp(-\alpha X) \quad (89)$$

$$p_Y(Y) = \frac{(\beta Y)^\beta}{Y \Gamma(\beta)} \exp(-\beta Y), \quad (90)$$

where α and β are parameters related to the large- and small-scale scintillations. They are determined by

$$\alpha = \frac{1}{\sigma_X^2} = \frac{1}{\exp(\sigma_{\ln X}^2) - 1} \quad (91)$$

$$\beta = \frac{1}{\sigma_Y^2} = \frac{1}{\exp(\sigma_{\ln Y}^2) - 1}, \quad (92)$$

where $\sigma_{\ln X}^2$ and $\sigma_{\ln Y}^2$ relate to the intensity variance caused by the large- and small-scale irradiance fluctuations shown in Eqs. (63) - (66).

For the varying turbulence profiles of the air-to-ground and ground-to-air link, the log-intensity variance $\sigma_{\ln I}^2$ can be substituted for the Rytov variance σ_R^2 . Putting it all together, the gamma-gamma PDF for the irradiance fluctuations is [2]

$$p(I) = \frac{2(\alpha\beta)^{(\alpha+\beta)/2}}{\Gamma(\alpha)\Gamma(\beta)I} \left(\frac{I}{\langle I(0, L) \rangle} \right)^{(\alpha+\beta)/2-1} K_{\alpha-\beta} \left(2 \left[\frac{\alpha\beta I}{\langle I(0, L) \rangle} \right]^{1/2} \right), \quad I > 0, \quad (93)$$

where the on-axis mean irradiance $\langle I(0, L) \rangle \neq 1$ and $K_\nu(x)$ is the modified Bessel function of the first kind.

2.5 The PDF of intensity for multiple transmitters

What happens to the irradiance distribution if multiple beams are received through independent turbulence realizations? It is a reasonable hypothesis that there should be a significant variance reduction and ultimately a much lower bit error rate. There is no closed-form solution for the distribution of the sum of multiple lognormal distributions or for even identically distributed ones. If these multiple laser sources

are sufficiently separated they could be considered independent identically distributed (iid) random variables (RV) in the limiting case. A number of folks have attempted to estimate the distribution of the sum of lognormal variables and in most cases have used a lognormal PDF in the estimate. Filho et al. presented a very accurate estimate by matching the first two moments of the inverse of the exact sum with those of the lognormal approximation inverse, i.e. [22]

$$\mathbb{E} [X^{-1}] = \mathbb{E} [S^{-1}] \text{ and} \quad (94)$$

$$\mathbb{E} [X^{-2}] = \mathbb{E} [S^{-2}], \quad (95)$$

where S is the sum of M lognormal variables and X is the proposed approximation to S and $\mathbb{E}[\cdot]$ is the expectation operation. Using the fact that the lognormal distribution k^{th} moment is given by

$$\mathbb{E} [X^k] = e^{k\mu+k^2\sigma^2/2}, \quad (96)$$

they solve for μ and σ , resulting in

$$\mu_s = 0.5 \ln \mathbb{E} [S^{-2}] - 2 \ln \mathbb{E} [S^{-1}] \quad (97)$$

$$\sigma_s^2 = \ln \mathbb{E} [S^{-2}] - 2 \ln \mathbb{E} [S^{-1}]. \quad (98)$$

This estimate is accurate for moments much higher than the second moment. The problem with this approach is there is no closed-form solution to the moments $\mathbb{E} [S^{-1}]$ and $\mathbb{E} [S^{-2}]$.

A straightforward approach to determine the distribution of the sum of iid signals up to the second moment can be determined since the sum of lognormals follows an approximately lognormal-type distribution. For the sum, $s = \sum_{i=1}^M x_i$ of independent signals x_i , the variance of s is the sum of the individual variances $\text{VAR}[x_i]$, and the mean is the sum of the individual means $\mathbb{E}[x_i]$, where $\text{VAR}[\cdot]$ is

the variance operation. That is to say [57]

$$\mathbb{E}[s] = \sum_{i=1}^M \mathbb{E}[x_i] \quad (99)$$

$$\text{VAR}[s] = \sum_{i=1}^M \text{VAR}[x_i], \quad (100)$$

and when they are independent and identically distributed (i.e. iid) they become

$$\mathbb{E}[s] = M \cdot \mathbb{E}[x_i] \quad (101)$$

$$\text{VAR}[s] = M \cdot \text{VAR}[x_i]. \quad (102)$$

Lognormally distributed independent variables have the PDF [57]

$$f(x_i) = \frac{1}{\sqrt{2\pi}x_i\sigma_i} \exp\left[-\frac{(\ln(x_i) - \mu_i)^2}{2\sigma_i^2}\right], \quad x_i > 0, \quad (103)$$

with

$$\mathbb{E}[x_i] = e^{(\mu_i + \sigma_i^2/2)} \quad (104)$$

and

$$\text{VAR}[x_i] = (e^{\sigma_i^2} - 1) e^{2\mu_i + \sigma_i^2}. \quad (105)$$

Therefore, the mean and variance of the sum of M iid variables are

$$\mathbb{E}[s] = M e^{(\mu_i + \sigma_i^2/2)} \quad (106)$$

and

$$\text{VAR}[s] = M (e^{\sigma_i^2} - 1) e^{2\mu_i + \sigma_i^2}. \quad (107)$$

Assuming the approximation of the sum of lognormally distributed independent variables is also lognormally distributed, the parameters μ_s and σ_s can be represented in terms of the $\mathbb{E}[s]$ and $\text{VAR}[s]$. Using the general form of a lognormal distribution,

the parameters μ_s and σ_s are represented by

$$\mu_s = \ln(\mathbb{E}[s]) - \frac{1}{2} \ln \left(1 + \frac{\text{VAR}[s]}{\mathbb{E}[s]^2} \right) \quad (108)$$

and

$$\sigma_s^2 = \ln \left(1 + \frac{\text{VAR}[s]}{\mathbb{E}[s]^2} \right). \quad (109)$$

Therefore, in general for $s = \sum_{i=1}^M x_i$, where x_i are lognormally distributed independent variables with parameters μ_i and σ_i^2 , the PDF of s can be approximated as

$$f_s(s) = \frac{1}{\sqrt{2\pi s \sigma_s}} \exp \left[-\frac{(\ln(s) - \mu_s)^2}{2\sigma_s^2} \right], \quad s > 0, \quad (110)$$

where

$$\mu_s = \ln \left(\sum_{i=1}^M e^{\mu_i + \sigma_i^2/2} \right) - \frac{1}{2} \ln \left[1 + \frac{\sum_{i=1}^M (e^{\sigma_i^2} - 1) e^{2\mu_i + \sigma_i^2}}{\sum_{i=1}^M e^{\mu_i + \sigma_i^2/2}} \right] \quad (111)$$

and

$$\sigma_s^2 = \ln \left[1 + \frac{\sum_{i=1}^M (e^{\sigma_i^2} - 1) e^{2\mu_i + \sigma_i^2}}{\left(\sum_{i=1}^M e^{\mu_i + \sigma_i^2/2} \right)^2} \right]. \quad (112)$$

For iid signals, the parameters μ_s and σ_s^2 can be further simplified to

$$\mu_s = \ln \left[M e^{\mu_i + \sigma_i^2/2} \right] - \frac{1}{2} \ln \left(1 + \frac{(e^{\sigma_i^2} - 1)}{M} \right) \quad (113)$$

and

$$\sigma_s^2 = \ln \left(1 + \frac{(e^{\sigma_i^2} - 1)}{M} \right). \quad (114)$$

As M gets large, the distribution approaches a Gaussian distribution, as it should according to the central limit theorem (CLT)¹. The CDF of a lognormal RV is

$$F(x_i) = \int_{-\infty}^{z_i} \frac{1}{\sqrt{2\pi}} e^{-\frac{\xi^2}{2}} d\xi \quad (115)$$

$$= 1 - Q(z_i), \quad (116)$$

where

$$Q(z_i) = \int_{z_i}^{\infty} \frac{1}{\sqrt{2\pi}} e^{-\frac{\xi^2}{2}} d\xi \quad (117)$$

and

$$z_i = \frac{\ln(x_i) - \mu_i}{\sigma_i}. \quad (118)$$

Similarly, the CDF of the sum of lognormal variables is given by

$$F(s) = \int_{-\infty}^{z_s} \frac{1}{\sqrt{2\pi}} e^{-\frac{\xi^2}{2}} d\xi \quad (119)$$

$$= 1 - Q\left(\frac{\ln(s) - \mu_s}{\sigma_s}\right), \quad (120)$$

where μ_s and σ_s are defined in Eq. (111) and Eq. (112).

The problem with this approach is that it is only accurate for the first two moments of the lognormal PDF and breaks down for higher-order moments. These higher-order moments tend to affect the tails of the distribution. As seen earlier for the beam wander and beam spreading example in Section 2.2.5, the tails of the distribution significantly affect the cumulative distribution used to calculate the fade probability.

¹The central limit theorem states that the distribution of the sum of a sufficient number of independent RVs with finite mean and variance is approximately normally distributed. The CLT explains why the Gaussian RV adequately describes so many different natural random processes [57, 74].

Going back to the fundamental approach, the PDF for the sum of M independent RVs can be determined by the convolution of the PDFs of the individual PDFs, noted by [57]

$$f_s = f_1 \circledast f_2 \circledast \cdots \circledast f_n, \quad (121)$$

where the convolution operation symbol is \circledast . The convolution can be calculated by Fourier transforming the PDFs, multiplying the resultant functions and inverse transforming the result as follows

$$p_s = p_1 \circledast p_2 \circledast \cdots \circledast p_M \quad (122)$$

$$= \mathcal{F}^{-1} \left\{ \prod_{i=1}^M \mathcal{F} \{p_i\} \right\}, \quad (123)$$

where \mathcal{F} is the Fourier transform operator and \mathcal{F}^{-1} is the inverse Fourier transform operator. Since there is no closed-form solution to the Fourier transform of the log-normal PDF, one can use the discrete Fourier transform (DFT) to approximate the result, where $\mathcal{F}_{k,n}$ is the DFT operator and $\mathcal{F}_{k,n}^{-1}$ is the inverse DFT operator. Using the DFT, the distribution can be approximated by

$$p_s(x_k) = \left(\frac{1}{\Delta x} \right)^{M-1} \mathcal{F}_{k,n}^{-1} \left\{ \prod_{i=1}^M \mathcal{F}_{k,n} [p_i(x_k)] \right\}, \quad (124)$$

where $p_i(x_k)$ are the discretized independent PDFs (sampled N times) of the multiple transmitters and

$$x_k = k \left(\frac{1}{\Delta x} \right) = k \left(\frac{N}{\max(x)} \right), \quad 0 \leq k \leq N - 1. \quad (125)$$

The DFT operation, $\mathcal{F}_{k,n}$, and inverse DFT operation, $\mathcal{F}_{k,n}^{-1}$, are defined by

$$\mathcal{F}_{k,n} \{p_i(x_k)\} = \sum_{k=0}^{N-1} p_i(x_k) e^{-j2\pi nk/N} \quad (126)$$

and

$$\mathcal{F}_{k,n}^{-1}\{\cdot\} = \frac{1}{N} \sum_{n=0}^{N-1} \{\cdot\} e^{j2\pi nk/N}, \quad (127)$$

respectively. The finer the sampling of the individual PDFs, the more accurate the PDF estimate of the sum. This relation applies to independent random variables, assuming the TxS are adequately spaced to be independent. The intensity distribution of each independent laser path varies depending upon how far off axis they are located. As M gets large, the distribution approaches a Gaussian distribution, as it should, according to the CLT.

Due to the periodic nature of the DFT, any aliasing must be mitigated. In this case, one needs to ensure there is finite support to the PDF and that the PDF is “zero-padded” so that the PDF extends to at least 2 times the support, to ensure minimal wrap-around.

To test the accuracy of this approach, the PDF is calculated for the sum of independent lognormal variables in a Monte-Carlo simulation and compared to the DFT approach mentioned here. This was accomplished by generating 5 independent lognormal random variables (RVs), adding them together, and calculating the resulting PDF. In Fig. 9 the average intensity of the sum of the lognormal variables is compared to a single lognormal variable. The means of the lognormal variables used in the sum were 1/5 the mean of the individual lognormal variable. The plot shows that for the sum of the RVs the mode is greater and the variance has been reduced as well. As M gets very large the PDF of the sum looks Gaussian with a mean centered around $I/\langle I \rangle = e$. In most practical cases the turbulence effects of two or more beams are partially correlated. The less correlated the effects, the more these multiple beams will reduce signal variability.

This DFT approach also works with the gamma-gamma PDF. Here, the probability of a fade for a 100 km FSOC system operating a horizontal link with a $C_n^2 = 10^{-17} \text{ m}^{-2/3}$ is calculated. The transmitter uses a $W_0 = 2 \text{ cm}$ collimated beam operating at a wavelength $\lambda = 1.55 \text{ }\mu\text{m}$ and a receiver aperture $D_G = 10 \text{ cm}$ for

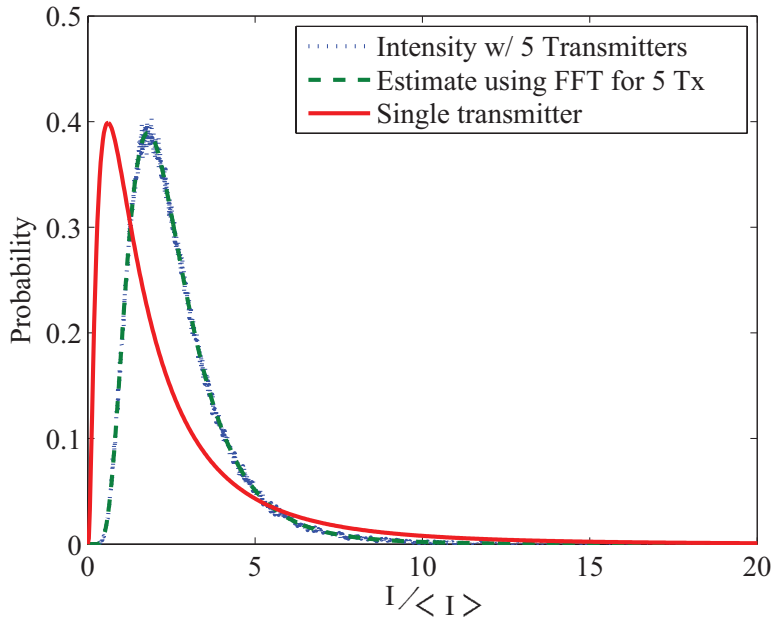


Figure 9: The average sum of lognormal RVs is compared with a single lognormal variable. $\sigma_i^2 = 1$, $\mu_i = 1/2$, $M = 5$ RVs, and with the PDF sampled $N = 10000$ times.

the Kolmogorov turbulence spectrum. The total transmitted power of the single-Tx and five-Tx systems were identical. A fade in this example is defined as when the signal drops 6 dB below the mean. The probability of a fade for a single-Tx system is 0.019. Assuming independent transmitters, the probability of a fade for the five-Tx case is approximately 6.6×10^{-7} , reducing the fade probability by a factor of over 28,000. These results are shown graphically in Fig. 10 where, distinctly, the single transmitter has much higher probability of being to the left of the threshold than the five-Tx case. Clearly, multiple-Tx systems can provide significant improvement.

2.6 Digital communication and detection theory

2.6.1 Modulation. With any communication system, the signal at the transmitter (Tx) must be modulated (i.e. varied in some way) to efficiently represent the information and propagate it effectively through the channel to the receiver (Rx). At the Rx, the signal is received, demodulated, and detected to extract the information

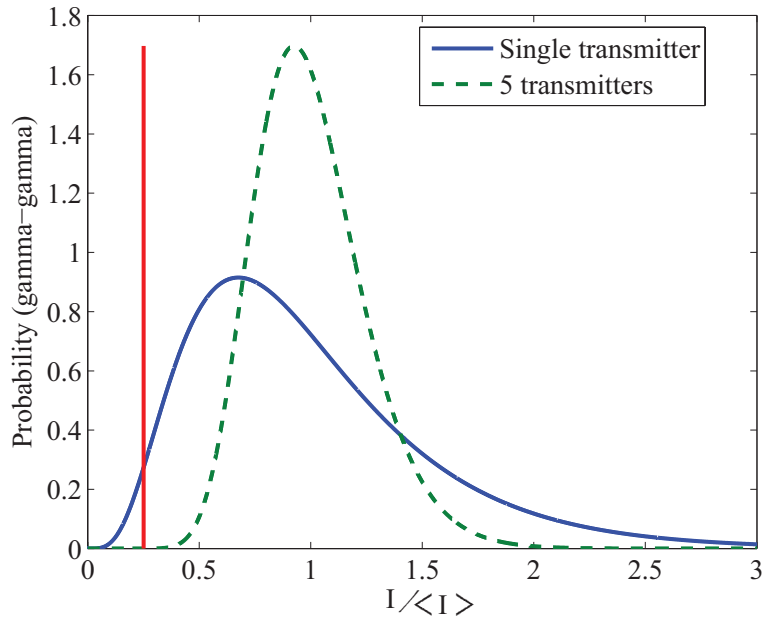


Figure 10: PDF of a single gamma-gamma RV (solid line) and a PDF of a sum of 5 gamma-gamma RVs (dashed line). The gamma-gamma RV models the received intensity for a 100 km $C_n^2 = 10^{-17} \text{ m}^{-2/3}$ path for a $W_0 = 2 \text{ cm-Tx}$ and a $D = 10 \text{ cm-diameter Rx}$. The threshold F_T is a solid vertical line 6 dB below the mean. Multiple Tx's are scaled to one fifth the power of the single Tx.

from the signal. The information can be represented by binary (2 symbols) or M-ary (M symbols) modulation. The information can be encoded on the frequency, polarity, signal level, phase, the pulse width of the signal, etc., or with any combination of these used to represent 2 to M symbols. This research effort uses the binary modulation scheme of on/off keying (OOK), which is accomplished by turning on the laser to transmit a ‘1’ and turning off the laser to transmit a ‘0’.

2.6.2 Noise sources and measured signal probability density functions. The process of measuring the signal at the receiver is inherently noisy. That is, there are multiple factors that contribute to the measured signal uncertainty at the Rx for each symbol. Each symbol transmitted has a different PDF associated with the measured receiver signal. The Gaussian distribution is often used to model system noise because of the CLT, defined in footnote 1. Even if the individual noise sources are not Gaussian, often the total noise can be approximated as Gaussian [74].

There are many potential noise sources in the optical measurement process, such as electronic thermal (or Johnson) noise, photon (or shot) noise, generation recombination noise, 1/f noise, background noise, dark current, amplifier noise etc. [18, 19]. More detail is given in Section 4.3. For optical receivers there are typically three sources of noise that dominate: thermal noise, shot noise, and amplifier noise. Thermal noise is caused by thermal motion of the electrons in the wires and resistor in a system. Shot noise is caused by the random arrival of photons at the receiver and is characterized by a Poisson distribution, which can be approximated by a Gaussian distribution if the signal levels are large enough. Inherently there are noise sources in amplifiers, and optical amplifiers are no exception. In the case of erbium doped fiber amplifiers (EDFAs), they exhibit amplified spontaneous emission (ASE) noise [1].

2.6.3 Detection theory. For the binary OOK modulation, the laser turns on to transmit a ‘1’ and turns off to transmit a ‘0’. The transmission of a ‘1’ or ‘0’ is equally likely and denoted by the events H_1 and H_0 , respectively. The likelihood ratio test (LRT) determines the optimal decision threshold based upon the PDFs of the

measured signal level i_m for the transmission of a ‘1’ $p(i_m|H_1)$ and the transmission of a ‘0’ $p(i_m|H_0)$. In general, the likelihood ratio test is [82]

$$\Lambda(i_m) = \frac{p(i_m|H_1)}{p(i_m|H_0)} \underset{\text{pick } H_0}{\overset{\text{pick } H_1}{\geq}} \frac{P(H_0)}{P(H_1)}. \quad (128)$$

For the equally likely case, since the a priori probabilities are $P(H_0) = P(H_1) = 0.5$, the above inequality simplifies to

$$\text{if } p(i_m|H_1) > p(i_m|H_0) \text{ pick } H_1 \quad (129)$$

or

$$\text{if } p(i_m|H_0) > p(i_m|H_1) \text{ pick } H_0. \quad (130)$$

The optimum detection criteria can best be described graphically. Given equally likely signaling, the optimum detection criterion is simply the point at which the two probability densities intersect as shown in Fig. 11. This maximum-likelihood solution minimizes the total probability of an error. The PDF of the receipt of a ‘0’ is relatively constant, whereas the PDF for the receipt of a ‘1’ depends upon the channel conditions. This channel could be affected by an obstruction, the weather (clouds, rain, fog, etc.), or changes in atmospheric turbulence conditions. These turbulence conditions vary significantly over time and thus could benefit from a threshold that varies with the optical signal level [13,18]. The optimal fixed threshold is determined in Section 5.2.2.1 and implemented in Section 5.4. The optimal adaptive thresholds are determined in Section 5.2.2.2 and implemented in Section 5.4.

This chapter described how FSOC systems are hampered by atmospheric turbulence. The next chapter summarizes the state-of-the-art in FSOC research and lays the groundwork for the research described in Chapters IV through VI.

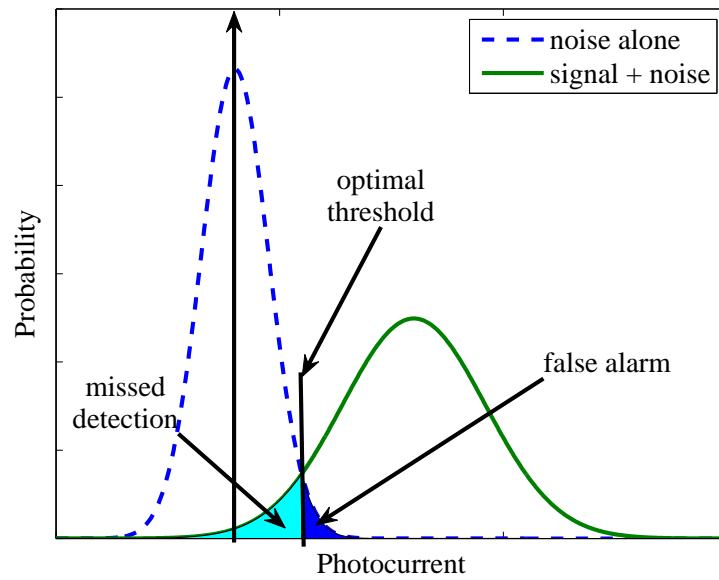


Figure 11: Decision threshold for an OOK digital receiver. If a signal is detected above the threshold it is called a '1' and below the threshold it is called a '0'. The shaded regions indicate the probability of an error.

III. Previous Work

FSOC research is broad and extensive, but it rarely focuses on airborne scenarios. Small-size and low-weight constraints are imperative for making airborne laser communication feasible. The key to this research is to use an integrated approach to engineer systems with as minimal hardware complexity while achieving acceptable performance. At each step along the way, the technique is optimized to address the appropriate system effect. This chapter surveys current free-space laser communication research and identifies opportunities for the greatest improvement for the least cost in size, weight, and complexity.

Sections 3.1 - 3.3 describe Tx and Rx designs that increase Rx power and decrease power fluctuations in atmospheric turbulence. In Section 3.4, modulation techniques are identified with the goal of finding one that is less sensitive to low power and large fluctuations. Finally, Section 3.5 delineates different signal processing techniques to determine how to decipher the bits more accurately.

3.1 Optical transmitter and receiver design

Transmitter and receivers need to be designed for a particular scenario and range of atmospheric conditions. Much of the research has been focused on the ground-to-space and the ground-to-ground propagation paths, rarely covering the air-to-air scenario.

Transmitter size. The transmitter aperture size and divergence drives the size of the beam at the receiver due to diffraction and plays a large part in the type and degree of intensity variations caused by atmospheric turbulence. Atmospheric turbulence causes the beam to wander, spread out, and break up, resulting in intensity variations at the receiver. The larger the beam, the less the beam wanders, but the more the beam breaks up and the lower the average received power. Churnside determined a relation for beam wander in weak turbulence [16]. Yenice and Evans proposed adaptive adjustment of the beam size to reduce the intensity fluctuations on a ground-to-satellite laser uplink [88]. They mentioned a beam size adjustment of

no more than a factor of two could be feasible and effective [88, 89]. This technique requires real-time knowledge of the atmospheric conditions, but one lesson from their research is to properly design and optimize the transmit beam size for the type of turbulence most likely encountered in the link. A transmitter could be defocused to increase the beam size at the receiver thereby reducing signal fades due to beam walk-off, but as the beam size increases the intensity fluctuations of the beam also increase. As always, a trade-off must be made between beam walk-off, average received power, and intensity fluctuations [75]. Using the analysis accomplished in Section 2.2.5 and Yenice's work on adaptive Tx beam size [88, 89], a $W_0 = 2.5$ cm collimated source optimized for the 100 km air-to-air path is used for the individual Tx size, which meets requirements for smaller and lighter weight components.

Partially coherent beams. The intensity fluctuations of an optical field after propagating through turbulence depend upon the turbulence along the path and the spatial coherence of the source. Therefore, one approach to reduce these fluctuations is to decrease the spatial coherence of the beam by placing a phase diffuser in front of the transmitting beam [64, 65]. Reducing the coherence of the beam not only spreads out the beam, but also reduces the intensity fluctuations caused by the interference (often referred to as laser speckle) of the coherent beam. This technique is very effective for short propagation paths, but for long propagation paths the beam spreading and power reduction can be quite severe. Therefore, it is not appropriate for the air-to-air scenario.

Optical amplification. An Erbium-doped fiber amplifier (EDFA) could reduce the power required at the detector [29]. As with any amplifier, it must be analyzed and optimized so as not to amplify the noise level so much that it becomes counter-productive. Razavi and Shapiro studied the link margin improvement of an amplified spontaneous emission (ASE) optical preamplifier, varied the receiver size and number of receivers, and tested OOK and binary pulse position modulation schemes with adaptive and constant thresholds [63]. They showed optical pre-amplification of 30 dB was sufficient to overcome thermal noise, increasing the receiver sensitivity by over

20 dB. The sensitivity was still below the shot-noise-limited case by about a 5 to 8 dB due to the noise figure of the amplifier (primarily driven by the ASE noise). Oftentimes, an amplifier is used at the transmitter end to reduce unwanted amplification of noise sources like ASE noise. An EDFA was used in this research due to its low-noise performance and bandwidth capability in the Terahertz [28].

Receiver aperture size (aperture averaging). As the receiver optic size increases, more power is collected at the receiver. In addition, the total received power fluctuation also decreases, especially when the size of the receiver increases beyond the correlation width. The correlation width is $\rho_{cw} = 1$ to $3[L\lambda/(2\pi)]^{1/2}$ for weak turbulence. For apertures larger than ρ_{cw} , different parts of the beam experience uncorrelated variations in intensity over the aperture. As a result, the aperture essentially averages these variations by focusing the intensity pattern onto the detector, commonly referred to as aperture averaging. Many have studied this phenomenon in regard to FSO performance [2, 15, 24, 63, 91–94]. This research uses the principle of reciprocity to determine the optimal separation distance for multiple transmitters using ρ_{cw} . This approach is first discussed in Section 4.1.5.

To collect as much power as possible and reduce intensity variations, the receiver optic should always be made as large as practical for any given system. In this research a single nominal receiver size is used to evaluate multiple-transmitter system designs.

3.2 Wavefront control

Wavefront-control systems measure and correct for fades in real time. Typically, wavefront sensors measure the real-time aberrations of the propagation path, and a closed-loop AO system applies a correction to pre-compensate the beam in real time. Most simple wavefront-control systems require the following: a beacon on the receiver station, a sensor, and a feedback loop to adjust/control the transmitted signal in real time to improve the link. The simplest of these systems involves only a tracking system with a fast-steering mirror to keep the beam centered on the receiver. Beam

walk-off results in the deepest fades, and therefore a system to keep the beam centered on the receiver can significantly improve performance.

Tracking and Pointing. *Tracking* refers to the real-time estimation of the transmitter direction needed to center the beam on the receiver. *Pointing* refers to the actual transmitter direction which includes the jitter of the transmitter platform and the tilt compensation applied to a fast-steering mirror to account for the atmospheric turbulence. For long transmission lengths, seemingly *minor* platform vibrations and errors in the control system at the transmitter can have a significant effect on the direction of the transmitted beam. This overall error in the tracking-control system is referred to as *jitter*. For a 100 km path an uncontrolled vibration on the order of 10 μrad at the transmitter translates into a 1 meter beam movement at the receiver. Jet Propulsion Laboratory and the California Institute of Technology presented their approach for a tracking and pointing system for a FSOC system for the International Space Station (ISS) in 2000 [44]. Their goal was a downlink capability of rates up to 2.5Gbit/s using adaptive optics, tracking, and pointing systems to compensate the beam for the turbulence effects [8, 32, 33, 44]. Many others have studied and designed various tracking systems for FSOC systems [35, 62, 79].

Platform jitter control. In Arnon's research on receiver jitter, he assumed the beam-tracking sensor and the data receiver used the same detector [6]. The satellite vibrations at the Tx caused the beam to non-uniformly spread across the tracking/-data detector array. Since the data receiver used the same detector as the tracker, he was able to vary the gain of the four detectors in his quad cell sensor depending upon the received tracker signal, improving communication system performance. As mentioned earlier, jitter at the transmitter can be very severe. For instance, the primary cause of beam pointing error for the proposed ISS downlink is platform jitter, not the atmosphere [44]. This is due to the long propagation length and the turbulence layer near the receiver, not the transmitter. Toyoshima determined the optimal ratio of the beam divergence to the angular platform jitter to reach the desired BER [75]. Sophisticated tracking systems have been used in previous research,

but for the multiple-transmitter case, a simple centroid tracker is used as a baseline from which to compare future work. Many more sophisticated tracking systems are used to help counter scintillation effects. Here, the multiple Tx's help to alleviate those effects. In addition, this research implements a Rx tracker which is especially important, since the Rx aperture is smaller than coherence diameter r_0 (defined in Eq. (30)) and encounters significant AOA variations.

AO systems. Higher-order phase aberrations cause the beam to break up and spread out and can be measured with a wavefront sensor and corrected by a deformable mirror [66, 69, 80]. Some researchers have proposed complicated wavefront control systems to sense and correct the transmitted signals in real time to reduce fading at the receiver [7, 33, 77, 78]. Tyson et al. reduced the BER by a factor of 41 in a hardware-in-the-loop experiment using AO wavefront control [81]. These bulky AO systems were used in high phase perturbation cases of $D/r_0 = 2$ to 9 often found in near field turbulence regimes. These phase correction systems would not be effective for the air-to-air case studied here, where $D/r_0 = 1/2$.

Receiver adaptive optic systems. Wavefront-sensorless systems reduce AO system complexity by removing the requirement for a wavefront sensor. These AO systems attempt to maximize the received power by optimally adjusting an adaptive element. Booth proposed an efficient method to measure the wavefront Zernike modes and optimally control the receiver AO [9]. Others have proposed other methods and techniques [53, 54, 87]. With these systems there are no complicated adaptive elements on the transmitter, significantly reducing transmitter size and weight. However, both types of higher order AO systems only correct for the phase cannot correct the strong scintillation in the air-to-air scenario. The multiple-Tx approach used here averages out the strong scintillation effects.

3.3 Diversity techniques

To avoid these bulky control systems, diversity techniques (i.e. multiple Tx's and Rx's, and interleaving) have been used in the literature to average out the spatial and temporal variations at the receiver. Each path should be separated from the others to maximize the differential variance between them. Much of the research has focussed on multiple Rx's. Some research has been accomplished on multiple-Tx systems, but surprisingly little research can be found on the theoretical angular separation required to take full advantage of these spatial diversity techniques, especially for the airborne application [34,58,59,68]. Rather, most literature on differential statistics for angular separations is concerned with an isoplanatic angle (relatively similar paths) for sensing and wavefront control.

Diversity techniques take advantage of the atmosphere's randomness by propagating through different atmospheric conditions and averaging the result. Multiple-transmitter systems take advantage of uncorrelated spatial atmospheric effects to average out the phase and amplitude variations at the receiver. This diversity can be accomplished in either time or space. These techniques include multiple transmitters, multiple receivers, and time interleaving. In each case, the goal is to separate the signals far enough apart that the fades are reduced by an averaging effect.

Multiple-input and multiple-output (MIMO) FSOC systems have been studied for both coherent and direct-detection (incoherent) systems. For example, spatial diversity could be accomplished at the receiver by a single large aperture (larger than ρ_c or multiple small apertures [3]. Some researchers have studied multiple-transmitter approaches [34,58,59,68] for the space-to-ground and the ground-to-ground scenarios, but few have studied the air-to-air scenario. Much of the spatial diversity research has focused on MIMO techniques or just multiple receivers to reduce signal fades, without defining the requisite separation distance. In this research, the spatial diversity techniques are optimized for the particular geometry and turbulence profile.

There are some advantages to multiple small apertures on the airborne platform over a single optic since they could be incorporated into conformal optics. Conformal optics lend themselves well to airborne platforms for size, platform aerodynamics, as well as reductions in aero-optic effects around the optic [52].

Fortunately, as this document shows later, multiple-transmitter techniques on airborne platforms are feasible due to the relatively small separation distance required for uncorrelated scintillation effects between the beams (i.e. 31 cm for the 100 km path). Multiple transmitters average out the effects of scintillation rather than using bulky or complicated AO systems that only correct for the phase. The scintillation effects of the extended turbulence for the air-to-air path are very strong (i.e. scintillation effects weighted heavily in the center of the path as shown in (48) and (49)), making this scenario particularly suited for a multiple-Tx system.

3.4 Modulation techniques

Many different modulation schemes can be used to encode the information on an optical signal. There are coherent techniques, direct-detection techniques (incoherent), polarization-modulation schemes, and quantum crypto-keying techniques. Some benefits and drawbacks of these techniques are discussed below.

Coherent techniques require extremely precise timing since optical signals are at extremely high frequencies (for 380-1550 nm wavelengths, the frequencies are 200-800 Terahertz). In 2006, Lange et al. used coherent modulation, namely homodyne binary phase-shift keying (BPSK), in a 142 km link between two islands with a beacon and tracking system. They transmitted 5.625 Gbit/s with a BER that varied between 10^{-4} to 10^{-6} , showing the potential robustness of coherent techniques [42]. They cited its immunity to sunlight interference as a decisive factor in its potential for commercial use. There are coherent techniques that can take advantage of the diversity of multiple-transmitter techniques. For example, Haas showed a marked im-

provement for a coherent heterodyne modulation scheme by using multiple space-time coded transmitters [29].

Direct-detection systems modulate the transmitted power incoherently and do not require the precise timing of coherent techniques. One of the simplest of these incoherent techniques is on/off keying (OOK) [74]. Many have used this binary digital communication technique in FSO systems in which a ‘1’ is represented by a pulse and the ‘0’ is represented by the absence of a pulse [1,39,95]. Another direct-detection technique modulates the polarization state of the transmitted optical signal. One such technique is polarization shift keying (PolSK) [76]. Since turbulence is isotropic and does not appreciably affect the polarization state, it seems to be an ideal modulation scheme at first. In this case when a fade occurs, it affects all symbols equally. Unfortunately, the key problem is during a signal fade the signal might not be high enough to adequately determine which polarization was sent. Often, the signal level required to determine the polarization is much higher than the level needed to determine if the laser is on or off as in OOK.

Another laser communication technique is quantum cryptography with entangled photons, where its promise lies in its security aspects. The polarization state of polarization-entangled-photon pairs is modulated and received. The Heisenberg uncertainty principle guarantees that an eavesdropper disturbs the signal and therefore is detected [38,61,73]. Current systems can only propagate at very low bit rates.

For simplicity, ease of use with multiple-transmitter systems, sensitivity at very low power levels, and to focus on mitigation of turbulence effects, OOK is used exclusively in this research. After implementing these techniques, there are still signal fades that need to be mitigated in some way. Signal processing techniques mentioned in the next section can allay the effects of these fades with little to no added size or weight.

3.5 *Signal processing techniques*

Once the signal has been received, signal-processing techniques like adaptive thresholding, automatic gain control, interleaving, and forward error-correction coding can be used to decipher symbols more accurately, resulting in improved BER. Most of these techniques have been applied to a single-transmitter system, while others have been applied to a coherent phase multiple-transmitter system. Still others have been proposed for the short, constant turbulence strength of the “last-mile” horizontal propagation. These techniques are driven by the temporal statistics and conditional probabilities of the FSOC system.

The BER of a digital communication system depends upon the conditional probability distributions of the received signals [82]. The communication system can be improved by determining the optimum decision threshold. Since these probabilities vary widely (but slowly in time compared with the signal frequency) due to the atmospheric conditions, adaptive detection thresholds can reduce the BER of FSOC systems [12–14, 18]. Researchers have successfully used various estimation techniques to adaptively determine the optimum threshold to include least-mean-square predictors [13], *Kalman filters* [12–14], and maximum likelihood estimators. The temporal statistics of the received signal dictate what type of estimator is adequate. Shown later a low sampling rate *linear* maximum likelihood estimator was sufficient, in this research, since the signal variation was reduced by the multiple-transmitter system. A lower sampling rate leads to a higher SNR, allowing for less signal diverted to the estimator.

Many investigators have proposed forward error correction codes (FECs) and interleavers for FSOC systems. Interleavers rearrange the symbols in time so that the errors caused by a long, deep fade are spread out so the decoder can handle the errors as if they were random errors [74]. Zhu and Kahn determined an upper bound for the code gain of a weak-turbulence optical channel. They considered block, convolutional, and Turbo codes in conjunction with varying the interleaver length and

determined that BER performance continues to improve with increasing interleaver length [96]. However, practical interleaver length is limited due to system complexity and delays in coding and decoding. Turbo codes were shown to out-perform convolutional codes for low signal to noise FSO systems [55]. Yu et al. demonstrated that Reed-Solomon codes could improve performance for log-normal atmospheric intensity variation statistics [90]. Since interleaver length is determined by the duration or span of the channel memory, not the particular statistical nature of the effects, fade statistics can be used to determine interleaver length. In Section 5.4.1 the multiple-Tx approach is shown to significantly reduce fade lengths, thereby reducing the required interleaver length. Interleavers and FEC systems are beyond the scope of this research, but they could be implemented in conjunction with the techniques presented in this research.

Automated gain control (AGC) systems are used to optimize particular detector and digital receiver performance. AGC systems can be either optical or electrical. Power levels at the receiver vary greatly, especially for the long extended turbulence case of air-to-air laser communication. An optical AGC can reduce this fluctuation so that the optical detector can be tailored to a particular optical signal range [10, 37]. Since this research does not prescribe a particular detector, an AGC was not implemented. In addition, the multiple Tx system reduces the variability and the adaptive threshold system adjusts the threshold with time. Therefore, likely reducing the effectiveness and need for an AGC system. The EDFA model used in this research could be refined to include the optical gain saturation inherent in EDFAs, providing some AGC to further improve the bottom-line performance.

3.6 Assessment of best areas for further research

This research strives to reduce the hardware complexity, while maintaining the performance required for an airborne laser communication system. This requires optimization of each subsystem. The goal is to achieve the highest data rate at the lowest BER, while maintaining a level of simplicity (i.e. size, weight, and power)

suitable for an airborne platform. Specifically, the goal of this research is to show how a multiple-beam system coupled with signal processing techniques can attain reliable communication at high-bit rates without requiring complicated higher-order control systems.

The techniques used in this research work well together, since the physical layer improvements reduce the variability of the received power and the signal processing approaches decipher the bits more effectively. The Rx and Tx tracking systems correct for the low-order phase (AOA variance and beam wander), the multiple Tx's correct for the high-order phase and amplitude effects, and the adaptive threshold counters the temporal variations of the signal level regardless of the turbulence severity. As is shown in Section 5.4.2, each of these techniques contributes to improve the performance, pushing the BER for the high-scintillation case below much more benign turbulence cases. All of these approaches improve the performance at the physical layer, so that interleavers and FEC systems could be added to reduce the BER even further.

IV. Anisoplanatic Turbulence Effects

The same atmospheric turbulence effects that limit the resolution of optical systems and make the stars twinkle can severely reduce the amount of power received in an FSOC system. The atmospheric turbulence in the propagation path causes the laser beam to wander, spread, and break up. These effects can cause the received signal power to drop below the receiver's threshold for milliseconds at a time. For an FSOC system, a millisecond fade means millions of bit errors. Since these optical power fades are often very deep, simply turning up the power in this case would not be very effective.

Two different ways to improve this condition are to increase the signal diversity to average out the effects or compensate for the turbulence conditions in real time. In the first approach, the temporal and spatial statistics of the turbulence for the propagation are estimated. Then, techniques are devised to overcome these effects by applying multiple uncorrelated realizations. In the second approach, typically, wavefront sensors measure the real-time phase aberrations, and a closed-loop AO system applies a correction to pre-compensate the transmitted beam's phase in real time.

Multiple-transmitter systems increase signal diversity and average out the deleterious effects of turbulence without bulky, complicated AO systems, making it an appropriate choice for airborne laser communications. In addition, AO systems do not correct for scintillation. Through analysis and simulation, the optimal configurations for multiple-Tx airborne FSOC systems are determined for various geometries and tracking systems.

This research derives the requisite angular and parallel separations for multiple-Tx systems for airborne and ground-to-ground laser communication. A majority of the previous research on multiple transmitters has focused on satellite communications (in which the turbulence is only present over a short part of the propagation path) or ground-based constant-turbulence-strength paths [4, 5, 30, 40, 59, 60, 68]. Here, this work presents these angular separations for three airborne geometries (air-to-air, air-

to-ground, and ground-to-air) through extended turbulence and determines practical configurations. Chapter III provided more details of previous research and other approaches.

Previous research on isoplanatism has defined the *maximum angle* over which the turbulence effects between two paths is relatively *similar* [26,69,70]. These *isoplanatic* angles have been determined for the tilt variance, higher-order phase variance, and scintillation (intensity variance). This research goes further to determine the *minimum angle* at which the paths are relatively *different* (i.e. *anisoplanatic*). The less correlated the amplitude and phase perturbations between the paths, the better the averaging effect for multiple beams.

With these separations computed, wave-optics simulations were conducted to explore how separation distances affect the BER for multiple-Tx FSOC systems. The simulations are performed for multiple scenarios and tracking systems to determine how effective these multiple-Tx techniques might be for airborne platforms.

4.1 *Uncorrelated paths*

This section determines the separation required to attain uncorrelated turbulence effects between two laser beam paths. To investigate this, it is instructive to first determine when the paths are relatively similar. If a system effect is space-invariant, it is called isoplanatic [27]. Therefore, if two laser beam paths are considered isoplanatic in terms of any particular turbulence effect, the effects of the two paths are highly correlated.

Most AO systems have a beacon path to measure the turbulence. Sensors at the imaging system or laser transmitter measure how the turbulence affects the beacon. If the differences between the phase effects (wavefront variations) of the propagation path and beacon path are negligible, the phase correction can potentially be implemented effectively. That is to say, the phase effects of the paths are isoplanatic. The phase isoplanatic angle θ_0 is the largest angle between two paths for which the wave-

front variations in the two paths are relatively similar [66]. The relation for this angle is presented in Eq. (31) in Chapter II. If the paths' effects are significantly different, the paths are anisoplanatic.

There are three different types of isoplanatism of interest in this research: the tilt θ_{TA} , phase θ_0 , and scintillation isoplanatic θ_{χ_0} angles. Tilt refers to the direction of propagation and deals with tracking a wandering beam or a jittering image. Phase incorporates both the tilt and the higher-order phase aberrations. Scintillation corresponds to the variations in intensity over the pupil. Typically, the tilt isoplanatic angle is larger than the phase isoplanatic angle, which is larger than the scintillation isoplanatic angle. Using these isoplanatic conditions as a starting point, the anisoplanatic conditions are determined for the phase and amplitude effects. The phase anisoplanatic angle $\theta_{\psi_{ind}}$ was first derived in support of this research [46, 47, 49].

The refractive-index fluctuations drive the phase and amplitude turbulence effects. For the derivations in this section, the von Kármán refractive index fluctuation PSD models these fluctuations [2, 66]

$$\Phi_n(\kappa, z) = \frac{0.033C_n^2(z)}{(\kappa^2 + \kappa_0^2)^{11/6}}, \quad (131)$$

where κ is the 3-D radial spatial frequency and $\kappa_0 = 2\pi/L_0$. This PSD is equivalent to Eq. (16), with the inner scale l_0 set to zero. This PSD is the most appropriate since it includes the outer scale L_0 which limits the size of the large-scale phase effects (i.e. turbulent eddies) which drive the phase anisoplanatic conditions. The refractive index PSD used to derive the isoplanatic conditions consists of only the numerator in Eq. (131), since the outer-scale does not affect the isoplanatic conditions.

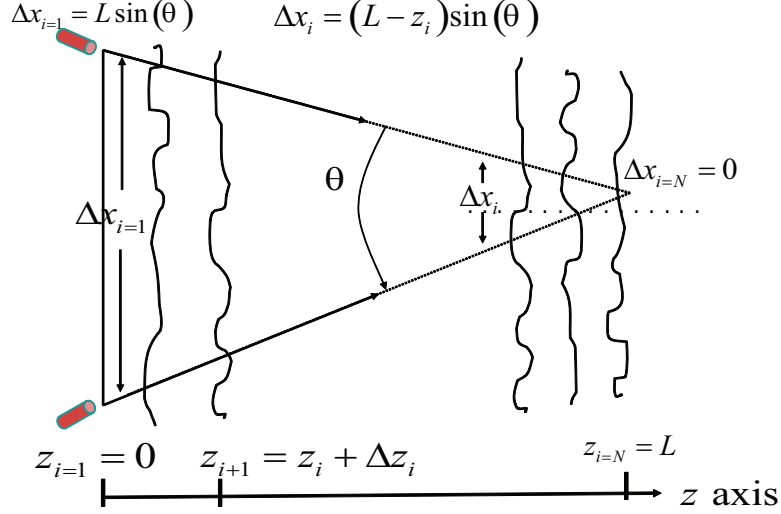


Figure 12: Isoplanatic angle geometry.

4.1.1 *Phase isoplanatism.* Fried derived the phase perturbation structure function in 1966 as [23, 66]

$$D_\psi(\Delta \mathbf{x}) = \langle [\psi(\mathbf{x}) - \psi(\mathbf{x} + \Delta \mathbf{x})]^2 \rangle \quad (132)$$

$$= 2B_\psi(0) - 2B_\psi(\Delta \mathbf{x}), \quad \text{for stationary random processes,} \quad (133)$$

$$= 2.91k^2 (\Delta x)^{5/3} \int_0^L C_n^2(z) dz, \quad (134)$$

where $\langle \cdot \rangle$ is the expectation operator and B_ψ is the auto-correlation. The ψ term denotes the pupil phase perturbation and $C_n^2(z)$ is the strength of turbulence along the path. It can be shown from Eq. (134) that the phase structure function at the receiver for two point sources separated by angle θ as viewed by the receiver is

$$D_\psi(\theta, L) = 2.91k^2 [\sin(\theta)]^{5/3} \int_0^L (L - z)^{5/3} C_n^2(z) dz. \quad (135)$$

This angular separation is shown in Fig. 12. For this geometry, most of the literature has defined the isoplanatic angle to be the angle at which the structure function is

less than or equal to unity [2, 26, 66]. Applying this condition,

$$D_\psi(\theta_0, L) = 1 \text{ rad}^2, \quad (136)$$

and solving for the angle results in the familiar isoplanatic angle relation defined by [26]

$$\theta_0 = \left[2.91k^2 \int_0^L C_n^2(z)(L-z)^{5/3} dz \right]^{-3/5}. \quad (137)$$

It is important to note which isoplanatic-angle definition is used. This definition assumes the two point sources are in the $z = 0$ plane. Many definitions in the literature define the $z = 0$ point as the receiver location [2, 66, 69]. To adjust, let $z' = L - z$ in Eq. (137).

4.1.2 Angular phase independence of two beams. Now, these concepts are applied to the statistical independence to determine the phase independence angle. The phase structure function in Eq. (135) increases with separation angle, approaching a maximum value at two times the mean square phase or $2\sigma_\psi^2$ as the two paths are placed far apart. This time, setting the structure function equal to the *maximum* value for the phase structure function yields [46]

$$D_\psi(\theta_{\psi_{ind}}, L) = 2\sigma_{\psi,pl}^2. \quad (138)$$

Combining Eqs. (136) and (138) leads to a way to solve for the phase independence angle $\theta_{\psi_{ind}}$, yielding [46]

$$\theta_{\psi_{ind}} = 2\sigma_{\psi,pl}^2\theta_0. \quad (139)$$

Using a geometrical optics plane-wave propagation approximation, the phase variance for a point receiver can be written as [2]

$$\sigma_{\psi,pl}^2 \cong 4\pi^2 k^2 \int_0^L \int_0^\infty \kappa \Phi_n(\kappa, z) d\kappa dz \quad (140)$$

$$= 0.78 k^2 \kappa_0^{-5/3} \int_0^L C_n^2(z) dz. \quad (141)$$

For horizontal propagation (i.e. constant C_n^2), the independence angle simplifies to [46, 47, 49]

$$\theta_{\psi_{ind}} = 0.7402 k^{4/5} C_n^{4/5} L^{-3/5} \kappa_0^{-5/3}. \quad (142)$$

As first derived in support of this research [46, 47, 49], this relation for $\theta_{\psi_{ind}}$ defines the angle over which the phase effects between the propagation paths of two point sources are nearly uncorrelated. It follows that the phase-independence separation distance can be defined as $d_{\psi_{ind}} = L\theta_{\psi_{ind}}$. As expected, the phase-independence angle increases with outer scale. At this angular separation, the beams should wander independently, and the higher-order phase perturbations should be uncorrelated as well. At this separation a fixed multiple-transmitter LCS (e.g. last-mile-type communications) could be designed so that at least one beam with sufficient power remains on the receiver at all times without the need for tracking. This independence angle is highly dependent on the outer scale, which varies near the ground as $L_0 \approx 0.4h$ [85]. For example, two $\lambda = 1.55 \mu\text{m}$ transmitters would need to be separated by $d_{\psi_{ind}} = 43 \text{ cm}$ ($\theta_{\psi_{ind}} = 213 \mu\text{rad}$) for a 2 km path located 1 m above the ground with a turbulence strength of $C_n^2 = 1.71 \times 10^{-14} \text{ m}^{-2/3}$. For a 4 km path, that separation would need to approach 65 cm. Figure 13 shows the requisite transmitter separations $d_{\psi_{ind}}(h)$ for four different path lengths given a particular height above the ground for each path.

At high altitudes, the effective outer scale is determined by the vertical outer scale and the horizontal outer scale. The vertical outer scale typically varies from 10 to 70 m [21], while the horizontal outer scale can be much larger. Aircraft measurements have determined the horizontal outer scale can be over hundreds of kilometers [85].

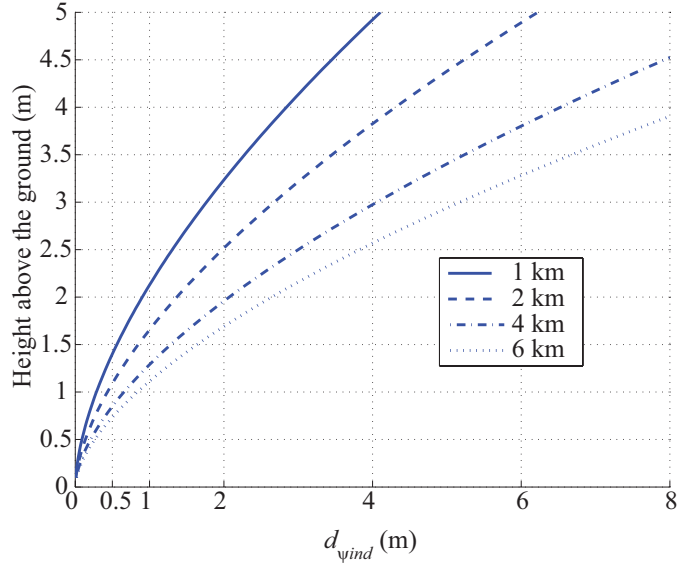


Figure 13: The phase independence distance $d_{\psi_{ind}}$ is plotted versus the height above the ground. Horizontal path with turbulence strength for each path corresponding to the HV57 profile, $L = 1, 2, 4, 6$ km, and $\lambda = 1.55 \mu\text{m}$ [46].

For horizontal propagation simulations in this work at altitude, an infinite outer scale is used because $L_0 \gg D$. When a finite L_0 is needed with slant ranges, the effective outer scale is determined by taking a slice through the vertical outer scale

$$L_0 = \frac{L_{0_{vert}}}{\cos \xi}, \quad (143)$$

where $L_{0_{vert}}$ is the outer scale for vertical propagations and ξ is the zenith angle. Both, the outer scale and inner scale l_0 vary with altitude. In this research, these bounds on the turbulence are consistent with atmospheric data presented by Wheelon [85]. See Section 2.2.3 in Chapter 2 for more details.

4.1.3 Parallel path isoplanatism. Using Eq. (134) again, this work determines the parallel path isoplanatic distance. Referring to the phase structure function at the receiver for two parallel path point sources separated by Δx yields [46, 66]

$$D_{\psi}(\Delta x, L) = 2.91k^2 (\Delta x)^{5/3} \int_0^L C_n^2(z) dz. \quad (144)$$

As for the angular isoplanatic angle condition, one can determine the separation Δx_0 at which the structure function is unity. The parallel isoplanatic distance is [46]

$$\Delta x_0 = \left[2.91 k^2 \int_0^L C_n^2(z) dz \right]^{-3/5} = 0.6611 \rho_0 = 0.3148 r_0, \quad (145)$$

where ρ_0 is the spatial coherence radius. [2, 66] For a constant- C_n^2 path, [46]

$$\Delta x_0 = 0.5268 k^{-6/5} C_n^{-6/5} L^{-3/5} = (3/8)^{3/5} L \theta_0. \quad (146)$$

Interestingly enough, this separation is simply $(3/8)^{3/5}$ times the separation for angularly separated paths. Similar to Eq. (138), the plane-wave independent phase separation distance Δx_{ind} is determined by setting the structure function equal to the maximum value and solving for the separation [46]

$$\Delta x_{ind} = 2\sigma_{\psi,pl}^2 \Delta x_0 = 0.4109 \kappa_0^{-5/3} \left[k^2 \int_0^L C_n^2(z) dz \right]^{2/5}. \quad (147)$$

For a constant- C_n^2 profile, it simplifies to [46]

$$\Delta x_{ind} = 0.4109 k^{4/5} C_n^{4/5} L^{2/5} \kappa_0^{-5/3} = (3/8)^{3/5} L \theta_{\psi_{ind}}. \quad (148)$$

4.1.4 Tilt isoplanatism. Sasiela developed relationships for the differential tilt variance which can also be referred to as the structure function $\sigma_T^2(x) = E[T(x_1) - T(x_1 + x)]^2$ of the Zernike tilt T . This work uses Sasiela's notation to allow the reader to follow this work and refer back to Sasiela's [69]. From those relations, he determined a relation for the tilt isoplanatic angle for an astronomical-seeing geometry. To simplify the relations for tilt, the Kolmogorov refractive index PSD is used since it does not include the outer scale. Sasiela investigated the effect of outer scale on the tilt isoplanatic angle. The outer scale greatly affects tilt variance, but does not appreciably affect tilt isoplanatism (especially when the outer scale is much larger than the receiver aperture) [70]. The differential tilt (i.e. the difference between

the Z-tilts) consisted of two contributions: one for $\Delta x < D$ (beams overlap) called the lower contribution and the other for $\Delta x > D$ (beams do not overlap) called the upper contribution, where D is the receiver diameter. The differential tilt variance differs with each axis: the beam displacement axis is denoted by the parallel symbol (\parallel), and the perpendicular symbol (\perp) denotes the other axis. Even though this difference in tilt variance can be quite significant [49,51,69], often these two orientations are added to determine the total differential tilt, since the tilt effects in the x and y directions are independent [69]. The total differential tilt is the sum of the lower and upper contributions for each axis [69]

$$\begin{bmatrix} \sigma_{\parallel}^2 \\ \sigma_{\perp}^2 \end{bmatrix} = \begin{bmatrix} \sigma_{\parallel}^2 \\ \sigma_{\perp}^2 \end{bmatrix}_L + \begin{bmatrix} \sigma_{\parallel}^2 \\ \sigma_{\perp}^2 \end{bmatrix}_U. \quad (149)$$

Sasiela determines the lower and upper contributions by calculating the differential tilt variance for the lower and upper condition. The lower contribution for $\Delta x < D$ (when the beams overlap) is [69]

$$\begin{aligned} \begin{bmatrix} \sigma_{\parallel}^2 \\ \sigma_{\perp}^2 \end{bmatrix}_L &= \frac{6.08}{D^{1/3}} \int_0^{L_c} C_n^2(z) \\ &\times \left\{ \begin{aligned} &\left[\begin{aligned} &1.316 \left(\frac{\theta z}{D}\right)^2 {}_5F_4 \left[\frac{7}{6}, -\frac{17}{6}, -\frac{5}{6}, \frac{5}{2}, 1; -\frac{1}{3}, 3, \frac{3}{2}, 2; \left(\frac{\theta z}{D}\right)^2 \right] \\ &0.4392 \left(\frac{\theta z}{D}\right)^2 {}_4F_3 \left[\frac{7}{6}, -\frac{17}{6}, -\frac{5}{6}, 1; -\frac{1}{3}, 3, 2; \left(\frac{\theta z}{D}\right)^2 \right] \end{aligned} \right] \\ &+ \left[\begin{aligned} &2.195 \left(\frac{\theta z}{D}\right)^{14/3} {}_4F_3 \left[\frac{5}{2}, -\frac{3}{2}, \frac{1}{2}, \frac{23}{6}, \frac{17}{6}, \frac{13}{3}, \frac{10}{3}; \left(\frac{\theta z}{D}\right)^2 \right] \\ &0.388 \left(\frac{\theta z}{D}\right)^{14/3} {}_3F_2 \left[\frac{5}{2}, -\frac{3}{2}, \frac{1}{2}, \frac{13}{3}, \frac{10}{3}; \left(\frac{\theta z}{D}\right)^2 \right] \end{aligned} \right] dz \end{aligned} \right\}, \quad (150) \end{aligned}$$

where $L_c = D/\theta$ and $H_c = D \cos(\xi)/\theta$. The function ${}_pF_q[(a); (b); z]$ is the generalized hypergeometric function where a and b are p - and q -dimensional arrays, respectively.

The upper contribution for $\Delta x > D$ (beams do not overlap) is [69]

$$\begin{aligned} \begin{bmatrix} \sigma_{\parallel}^2 \\ \sigma_{\perp}^2 \end{bmatrix}_U &= \frac{6.08}{D^{1/3}} \times \left\{ \int_{L_c}^L C_n^2(z) dz \right. \\ &\quad \left. - \int_{L_c}^L C_n^2(z) \begin{bmatrix} 0.531 \left(\frac{D}{\theta z}\right)^{\frac{1}{3}} {}_4F_3 \left[-\frac{5}{6}, \frac{5}{2}, \frac{1}{6}, \frac{2}{3}; 5, 3, -\frac{1}{3}; \left(\frac{D}{\theta z}\right)^2 \right] \\ 0.798 \left(\frac{D}{\theta z}\right)^{\frac{1}{3}} {}_3F_2 \left[-\frac{5}{6}, \frac{5}{2}, \frac{1}{6}; 5, 3; \left(\frac{D}{\theta z}\right)^2 \right] \end{bmatrix} dz \right\}, \end{aligned} \quad (151)$$

where L is propagation length and H is the transmitter height. Above about 30 km the turbulence is small and practically negligible. If the turbulence strength is in terms of the propagation distance z , select $L_c = D/\theta$, and if the relations are in terms of the height h , use $H_c = D \cos(\xi)/\theta$.

Sasiela goes on to derive a relation for the tilt isoplanatic angle θ_{TA} using the lower contribution for an astronomical seeing geometry. For small displacement angles where H_c is higher than the uppermost turbulence, the tilt isoplanatic angle is defined in terms of Eq. (150) using the following differential tilt jitter [69]:

$$\begin{aligned} \sigma_T^2(\theta) &= \frac{2.67\mu_2^-(H_c)}{D^{1/3}} \left(\frac{\theta}{D}\right)^2 \quad (4) \\ &\quad - \frac{3.68\mu_4^-}{D^{1/3}} \left(\frac{\theta}{D}\right)^4 \quad (6) + \frac{2.35\mu_{14/3}^-}{D^{1/3}} \left(\frac{\theta}{D}\right)^{14/3} \left(\frac{20}{3}\right) + \dots \quad (152) \end{aligned}$$

This angle is characterized as the angle in which the differential tilt jitter is equal to one-half the diffraction-limited beam width. For the definitions of the moments of the propagation path μ_m , μ_m^- , and μ_m^+ refer to Eqs. (23) - (26).

Using the first factor in Eq. (152) for $\theta < D/40,000$ and setting $\sigma_T^2(\theta)$ equal to one half of the diffraction-width angle yields

$$\left(\frac{0.61\lambda}{D}\right)^2 = \frac{2.67\mu_2^-}{D^{1/3}} \left(\frac{\theta_{TA}}{D}\right)^2 \quad (4). \quad (153)$$

Solving for θ_{TA} as Sasiela did, the tilt isoplanatic angle is defined as the angle between two sources for which the tilt jitter is equal to one-half the diffraction limited spot

size. Therefore, θ_{TA} is [69]

$$\theta_{TA} = \frac{0.184\lambda D^{1/6}}{(\mu_2^-)^{1/2}}. \quad (154)$$

Using results published by Sasiela for the differential tilt between two beams, i.e. Eqs. (150) and (151), an approximation is developed here for the differential tilt for a constant- C_n^2 profile or horizontal propagation that takes into account both the lower ($\Delta x < D$) and upper ($\Delta x > D$) contributions. Starting with $\Delta x < D$, one must only consider the lower contribution for $\theta < D/L$, where $\theta = \Delta x/z$. After performing the integration over z from 0 to the propagation length L , the differential tilt becomes [46]

$$\begin{aligned} \begin{bmatrix} \sigma_{\parallel}^2 \\ \sigma_{\perp}^2 \end{bmatrix} &= \frac{6.08C_n^2}{D^{1/3}} \times \left\{ \begin{bmatrix} 1.316 \\ 0.439 \end{bmatrix} \left[\left(\frac{\theta}{D}\right)^2 \left(\frac{L^3}{3}\right) - \begin{bmatrix} 2.2955 \\ 1.377 \end{bmatrix} \left(\frac{\theta}{D}\right)^4 \left(\frac{L^5}{5}\right) + \dots \right] \right. \\ &\quad \left. + \begin{bmatrix} 2.195 \\ 0.388 \end{bmatrix} \left[\left(\frac{\theta}{D}\right)^{14/3} \left(\frac{3}{17}\right) L^{17/3} - \begin{bmatrix} 0.1756 \\ 0.1298 \end{bmatrix} \left(\frac{\theta}{D}\right)^{20/3} \left(\frac{3}{23}\right) L^{23/3} + \dots \right] \right\}, \end{aligned} \quad (155)$$

where $\theta_{TA} < D/L$. As θ approaches zero, the differential variance approaches zero, as expected. To define the tilt isoplanatic angle as Sasiela did, the infinite sum's first term is set equal to one half of the diffraction-width angle,

$$\sigma_T^2 = \sigma_{\parallel}^2 + \sigma_{\perp}^2 \approx \frac{6.08C_n^2}{D^{1/3}} \times \left[1.755 \left(\frac{\theta_{TA}}{D}\right)^2 \left(\frac{L^3}{3}\right) \right] = \left(\frac{0.61\lambda}{D}\right)^2. \quad (156)$$

Solving for θ_{TA} yields the tilt isoplanatic angle for horizontal propagation as approximately [49]

$$\theta_{TA} = \frac{0.319\lambda D^{1/6}}{C_n L^{3/2}}, \quad \theta < D/L. \quad (157)$$

This straightforward equation for constant turbulence strength can only be used when the beams overlap and $\Delta x < D$. For the astronomical viewing condition the simplification to only use the lower contribution is valid since turbulence above about 30 km

is negligible. Now for the horizontal propagation, considering $\theta > D/L$, and following Eq. (149), the most significant terms must be added to the lower *and upper* portions to determine the overall differential tilt variance

$$\begin{bmatrix} \sigma_{\parallel}^2 \\ \sigma_{\perp}^2 \end{bmatrix} \approx \frac{6.08C_n^2}{D^{1/3}} \left\{ L \begin{bmatrix} 1 \\ 1 \end{bmatrix} - \begin{bmatrix} 0.7801 \\ 0.9057 \end{bmatrix} \frac{D}{\theta} - \begin{bmatrix} 0.797 \\ 1.197 \end{bmatrix} \left(\frac{D}{\theta}\right)^{\frac{1}{3}} \left[L^{\frac{2}{3}} - \left(\frac{D}{\theta}\right)^{\frac{2}{3}} \right] \right\} \quad (158)$$

The parallel and perpendicular tilt variances are added to determine the overall tilt variance:

$$\sigma_T^2 = \sigma_{\parallel}^2 + \sigma_{\perp}^2 \approx \frac{6.08C_n^2}{D^{1/3}} \left[2L + 0.3077 \frac{D}{\theta} - 1.9935 \left(\frac{D}{\theta}\right)^{1/3} L^{2/3} \right] \quad \theta > D/L. \quad (159)$$

Unlike Eqs. (153) and (156) the terms in Eq. (159) include the upper and lower significant contributions and therefore includes additional terms. As before, one could solve for θ_{TA} , this time numerically, to determine the tilt isoplanatic angle for $\theta > D/L$.

4.1.5 Scintillation anisoplanatism. Stars twinkle, but the moon and even the planets do not twinkle in the night sky because their angular extents are much larger than the scintillation independence angle. In weak turbulence, the angle at which two point sources scintillate independently was postulated by Fried to be $\theta_{\chi_{ind}} = 0.8(Lk)^{-1/2}$, [25] corresponding to a separation distance of $d_{\chi_{ind}} = 0.8(L/k)^{1/2}$. This relation is very similar to the correlation width ρ_{cw} defined as the $1/e^2$ point of the normalized irradiance covariance function. [2] Since ρ_{cw} , for weak turbulence varies between 1 to 3 Fresnel zones $(L/k)^{1/2}$ depending on beam size, ρ_c is referred to in this work as simply [2, 46]

$$\rho_c = \sqrt{L/k}. \quad (160)$$

For strong turbulence ($\mathcal{R}_{sph} \gtrsim 0.25$) the scintillation saturates and the correlation width of irradiance fluctuations ρ_{cw} is driven by the spatial coherence radius ρ_0 and the scattering disk $L/(k\rho_0)$.

The correlation width ρ_{cw} is often used to describe the receiver size at which aperture averaging occurs as the receiver size increases. Here, the principle of reciprocity determines the angular transmitter separation, referring to this relation as the scintillation correlation angle $\theta_{\chi_c} = (Lk)^{-1/2}$. The analogous angular relation to the correlation width ρ_{cw} is the scintillation independence angle $\theta_{\chi_{ind}}$ defined as the angle at which the scintillation between the two paths are relatively uncorrelated. The values of θ_{χ_c} for propagation lengths of 100 km and 29 km at $\lambda = 1.55 \mu\text{m}$ are $1.57 \mu\text{rad}$ and $2.91 \mu\text{rad}$, respectively. The values of $\theta_{\chi_{ind}}$ are determined by simulation in relation to scalar multiples of θ_{χ_c} and ρ_c in Section 4.5.

4.1.6 Considerations of isoplanatic and anisoplanatic effects. As mentioned in Section 4.1.2, the anisoplanatic condition can be determined by analyzing the structure functions of the effects. In previous work, the analytic log-amplitude $D_\chi(d)$ and phase structure functions $D_\psi(d)$ were determined for a horizontal path as [45, 46]

$$D_\chi(d) = 3.089 \left(\frac{L_0}{r_0}\right)^{5/3} \int_0^\infty \left[1 - J_0\left(\frac{\kappa d}{L_0}\right)\right] \left[1 - \frac{2\pi L_0^2}{\lambda L \kappa^2} \sin\left(\frac{\lambda L \kappa^2}{2\pi L_0^2}\right)\right] \frac{\kappa d \kappa}{(\kappa^2 + 4\pi^2)^{11/6}} (161)$$

and

$$D_\psi(d) = 3.089 \left(\frac{L_0}{r_0}\right)^{5/3} \int_0^\infty \left[1 - J_0\left(\frac{\kappa d}{L_0}\right)\right] \left[1 + \frac{2\pi L_0^2}{\lambda L \kappa^2} \sin\left(\frac{\lambda L \kappa^2}{2\pi L_0^2}\right)\right] \frac{\kappa d \kappa}{(\kappa^2 + 4\pi^2)^{11/6}}, (162)$$

where J_0 is the zeroth-order Bessel function of the first kind and the von Kármán PSD from Eq. (131) was used to model the turbulence. The structure functions are plotted with the corresponding isoplanatic and anisoplanatic distances in Fig. 14. Starting with the phase effects plotted against the right scale with a dash dot line, the isoplanatic angle occurs when the phase structure function is unity. As the separation widens, the tilt effects are isoplanatic until the tilt isoplanatic angle is reached. The

only significant difference in these phases is due to the higher-order phase. Finally at separations on the order of about $\rho_{cw} = 2L_0$, all of phase effects including tilt are anisoplanatic between the two paths. The amplitude effects are plotted against the left scale with a solid line. At about $2\rho_c$, the structure function reaches a maximum and settles into a value of two times the mean square log-amplitude variance, as the amplitude effects become uncorrelated. These separations are determined by the Fresnel zone $(L/k)^{1/2}$ and are consistent with results for weak turbulence, [46] i.e. Rytov number $\mathcal{R}_{sph} < 0.25$ mentioned in Section 4.1.5 [2].

Anguita et al. simulated much stronger turbulence in a ground-to-ground propagation scenario where $\mathcal{R}_{sph} = 1.6$. Their uncorrelated separation distances were greater (approximately $6 \rho_c$) due to the long correlation tail of the strong turbulence characterized by the scattering disk $L(k\rho_0)$ [2, 5]. Polynkin and Peleg also simulated strong turbulence in a ground-to-ground configuration to study the scintillation reduction of multiple transmitters, but their research also did not cover the air-to-air turbulence effect regime [59, 60].

The relations for isoplanatic and anisoplanatic effects are compared for different scenarios in Fig. 15. Horizontal propagation near the ground is shown in Fig. 15b. If the transmitters are separated by the phase-independence angle for the ground-to-ground scenario, then tracking might not be required. Provided there is a sufficient number of transmitters, the beams would wander independently with at least one beam on the receiver at any given moment. The fixed pointing angle could be determined by maximizing the long-term irradiance for each beam. The isoplanatic angle and the scintillation correlation angle cross at about 2.5 km. For propagations beyond the cross-over point, scintillation is more correlated than phase effects. In Fig 15c, these terms cross, too, this time after propagating about 100 km. This also corresponds very well with Fig. 14 where the isoplanatic angle and the scintillation correlation angle nearly coincide with θ_0 slightly smaller than θ_{χ_c} for the 100 km air-to-air scenario [46].

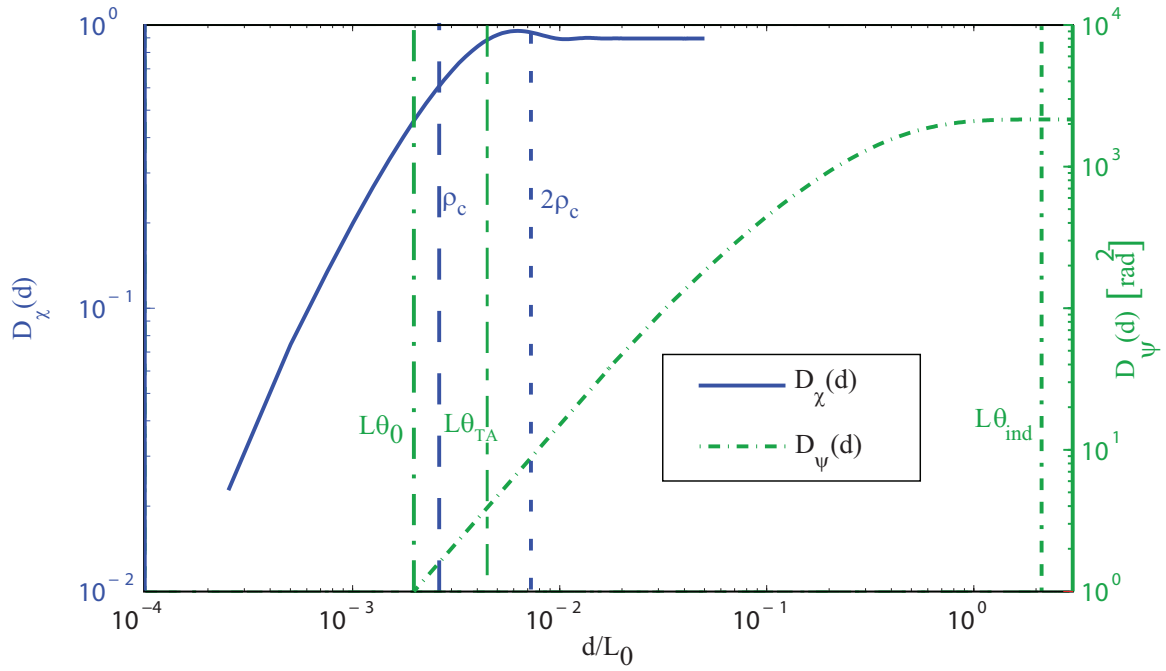


Figure 14: The phase (right scale) and log-amplitude (left scale) structure functions are plotted for a 100 km horizontal propagation at 10 km altitude, with angularly separated beams. The strength of turbulence is $L_0/r_0 = 286$ and $L_0^2/(\lambda L) = 23225$ [46]. Isoplanatic and anisoplanatic separation distances are shown for the amplitude and phase effects.

Table 1: Required beam separation for averaging.

$(\theta_A \geq \theta_{\psi_{ind}} \approx \theta_{T_{ind}} > \theta_{TA} > \theta_B > \theta_0 > \theta_C \geq \theta_{\chi_{ind}} > \theta_{\chi_0})$			
Angular Separation	Technique	Applicable Scenario	Effects Averaged
$\theta_A \approx \theta_{\psi_{ind}}$	Non-tracked Multiple Tx	G-to-G	AOA and beam wander, phase, and amplitude
$\theta_B > \theta_0$	Tracked, Multiple Tx	A-to-A, A-to-G, G-to-A	phase, amplitude
$\theta_C \approx \theta_{\chi_{ind}}$	Tracked, Multiple Tx	A-to-A, A-to-G, G-to-A	amplitude
N/A	Tracked, Parallel Multiple Tx	A-to-A, A-to-G, G-to-A	amplitude

For a mobile Tx and/or Rx, the beams must be tracked. For these tracked-beam cases in Fig. 15c air-to-air path, Fig. 15(d) air-to-ground path, and Fig. 15e ground-to-air path, separations beyond the isoplanatic angle up to approximately the tilt isoplanatic angle should average out the higher-order phase effects. Separations larger than the tilt isoplanatic angle require separate trackers. This occurs for longer propagations and near-transmitter turbulence, since the phase tilt effects are large due to the long lever arm of the turbulence. Small isoplanatic and tilt-isoplanatic angles occur for propagations longer than 100 km in Fig. 15c and for the ground-to-air propagation shown in Fig. 15e. Fig. 15d for the air-to-ground scenario shows that the correlation angles get smaller as the propagations get longer, but as the transmitter altitude gets above the turbulence at about 12 km, the angles remain relatively similar [46].

4.2 Simulation set-up and validation

Simulations of different scenarios and separation distances show how much multiple transmitters improve BER performance. The turbulence effects explored in simulated scenarios were represented by random optical field screens with the correct statistics placed along the path. The layers for this research were chosen to simu-

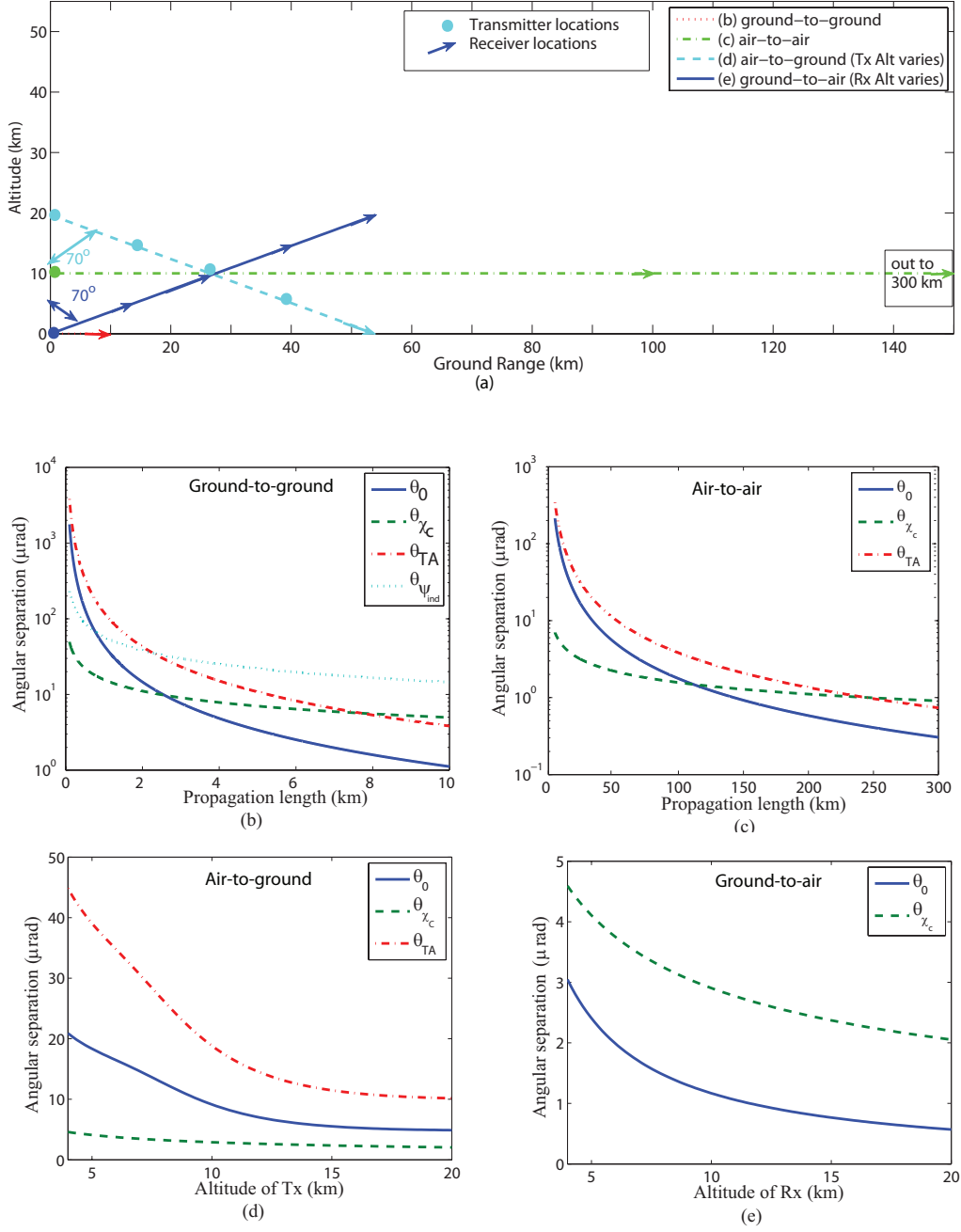


Figure 15: (a) Phase isoplanatic angle (θ_0), scintillation correlation angle (θ_{χ_c}), tilt isoplanatic angle (θ_{TA}), and phase uncorrelated angle ($\theta_{\psi_{ind}}$) are shown for a receiver diameter of $D_R = 20$ cm for HV-57 profile. (b) Horizontal propagation: altitude $h = 1$ m, $L_0 = 40$ cm, $C_n^2 = 10^{-14} \text{ m}^{-2/3}$, and $L = 0$ to 10 km. (c) Horizontal propagation: altitude $h = 10$ km, $L_0 = 100$ km, $C_n^2 = 10^{-17} \text{ m}^{-2/3}$, and $L = 0$ to 300 km. (d) Air-to-ground path: Transmitter height $H_{Tx} = 4$ to 20 km, $\xi = 70^\circ$, and receiver height $H_{Rx} = 0$ km. (e) Ground-to-air path: $H_{Tx} = 0$ km, $\xi = 70^\circ$, and $H_{Rx} = 4$ to 20 km [46].

Table 2: Atmospheric parameters for the scenarios used in the BER calculations.

Scenario	$r_{0_{pl}}$ (cm)	$r_{0_{sph}}$ (cm)	\mathcal{R}_{pl}	\mathcal{R}_{sph}	θ_0 (μrad)	θ_{TA} (μrad)	Λ_0
G-to-G	2.5	4.5	1.08	0.437	3.5	11.7	3.2
G-to-A	10	85	0.911	0.0461	1.2		11
A-to-A	23	41	0.384	0.155	1.3	3.0	79

late the continuous model so that several low-order moments of the layered model accurately match the continuous model [46].

4.2.1 Simulation set-up. In this research, 10 random phase screens were used to model the turbulence along varying-turbulence-strength paths and five screens along the constant-turbulence-strength paths. The layered analytic planar and spherical coherence diameter r_0 , planar and spherical Rytov numbers \mathcal{R} , and isoplanatic angle θ_0 matched within 1% of the full path continuous atmospheric turbulence parameters. Table 2 summarizes the atmospheric parameters for the simulations used to calculate the BER. In the simulations that follow, a Gaussian beam with a $1/e$ field radius $W_0 = 2.5$ cm and $\Lambda_0 = 2L/(kW_0^2)$ propagates to the receiver aperture. Andrews and Phillips call beams with $\Lambda_0 \gtrsim 100$ approximately spherical and $\Lambda_0 \lesssim 0.1$ approximately planar. Therefore, the equations in previous sections where a point source or spherical wave are used are a reasonable approximations, especially for the air-to-air propagation. Earlier, the von Kármán turbulence power spectrum was used to model the phase effects [46].

Andrews and Phillips' modified turbulence power spectrum is used in the simulations performed in this research because it includes L_0 and l_0 , and gives the best agreement with collected atmospheric data for phase and *amplitude* effects [2]. The Hufnagel-Valley turbulence profile was used in this research with the parameters set to the HV-57 moderate turbulence strength (i.e. turbulence at the ground is $A = 1.7 \times 10^{-14} \text{m}^{-2/3}$ and the effective wind at altitude is $W = 21$ m/s) [46].

FS-based phase screens were used, since it allows for better low spatial frequency representation than other techniques [45, 48, 66, 67, 83]. This modal phase screen

is defined in terms of the spatial frequencies of the refractive-index PSD and need only be evaluated at the grid points of interest. See Section 2.4 for details. This approach is particularly effective when calculating the fields of widely spaced beams over long periods of time. Although, in this work independent random realizations of turbulence are used in the simulations by assuming the turbulence is an ergodic random process [46].

Split-step Fresnel propagations were performed for the $W_0 = 2.5$ cm collimated Gaussian beam. Great care was taken to adequately sample the Fresnel propagation between the screens as well as the turbulence effects as the beam propagates. First, the geometric constraints must be satisfied to avoid aliasing in the region of interest. Then one must adequately sample the quadratic phase term in the Fresnel propagation so that the phase in that same of region of interest is not corrupted by aliasing. This required satisfying these four sampling constraints:

$$\delta_n \leq \frac{\lambda L - D_{Rx} \delta_1}{D_{Tx}}, \quad (163)$$

$$N \geq \frac{D_{Tx}}{2\delta_1} + \frac{D_{Rx}}{2\delta_n} + \frac{\lambda L}{2\delta_1 \delta_n}, \quad (164)$$

$$\delta_n \leq \left| 1 + \frac{L}{R} \right| \delta_1 - \frac{\lambda z}{D_{Tx}}, \quad (165)$$

$$N \geq \frac{\lambda L}{\delta_1 \delta_n}, \quad (166)$$

where δ_1 is the sampling size in the transmitter plane and δ_n is the sampling size in the receiver plane [17]. Additionally, D_{Rx} is the receiver diameter, D_{Tx} is the transmitter diameter, L is the propagation length, R is the beam's radius of curvature, and λ is the laser wavelength. The fourth and most restrictive constraint listed above Eq. (166) was satisfied by performing multiple partial propagations (sometimes referred to as split step propagations) to propagate the full distance. Finally, the turbulence must be adequately sampled and the wandering and beam spreading must be taken into account by choosing large enough screens.

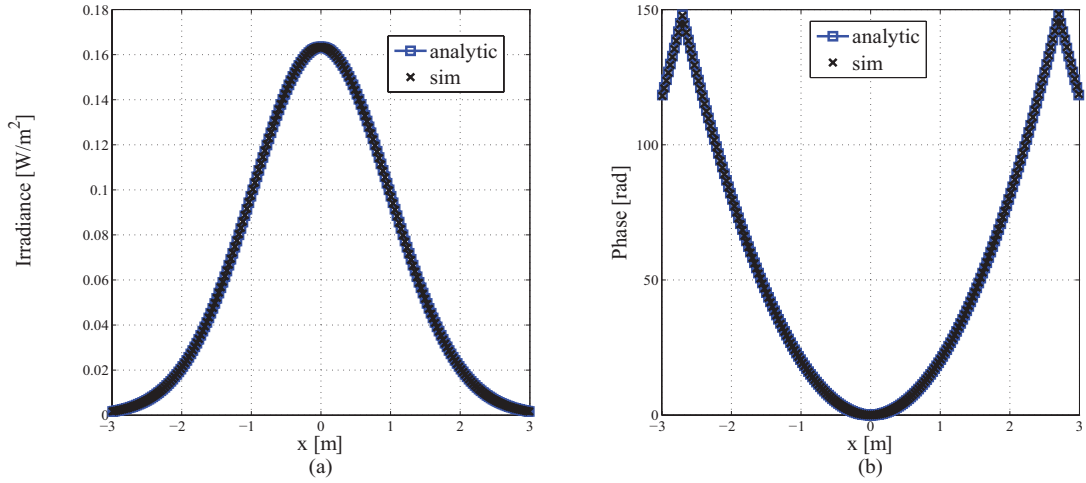


Figure 16: The plot shows the irradiance and the phase of a Gaussian beam with $W_0 = 2.5$ cm after propagating 100 km with no turbulence using the propagation code, compared against the analytic solution.

4.2.2 Validation of simulation results. Validating simulations is important to ensure the calculations and simulations accurately predict the diffraction and atmospheric turbulence effects. Figure 16 shows the irradiance and phase of a $W_0 = 2.5$ cm e^{-1} field radius Gaussian beam after propagating 100 km through vacuum using the propagation code compared with the analytic solution. The two discontinuities in the derivative of the phase show the boundary of accurate phase representation. Beyond that width there is aliasing in the quadratic phase factor, but it is beyond the region of interest and does not affect the signal received by the 20 cm aperture. Now that correct propagation is demonstrated, the atmospheric effects are verified. The structure function of each of the phase screens was consistent with the theoretical values. Figure 14 shows the structure function averaged over 40 screen realizations compared to the theoretical value for different turbulence strengths.

The long-term spot size W_{LT} is measured by averaging the spot size of a long period of time or over many iid realizations. This spot size was consistent with theory for all scenarios. For the ground-to-air propagation the long term spot size

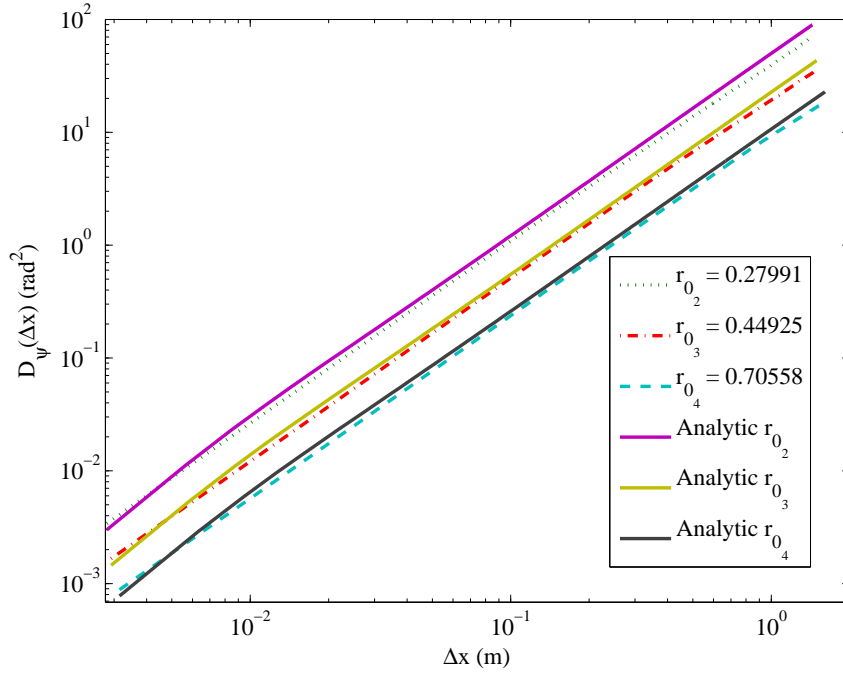


Figure 17: Structure functions of three representative screens averaged for 40 random screen realizations. The analytic structure functions are plotted with solid lines.

was $W_{LT} = 67$ cm using the propagation code, compared to a theoretical spot size using Eq. (46) of 62 cm.

The measured scintillation is consistent with the theoretical values for the spherical and planar Rytov numbers. The theoretical log-amplitude variance is 0.046 for a spherical wave and 0.91 for a planar wave for the 0 to 10 km in altitude propagation at a 70° zenith angle. The centroid-tracked scintillation index for the center pixel was 0.073. For the untracked case the scintillation index was 0.14 which more closely matches the theoretical value of $4 \times 0.046 = 0.18$ [46].

For the 0 to 10 km 70° -zenith-angle propagation path a simulated point source was propagated to the receiver and the statistics were calculated. The scintillation index for the untracked case was 0.12. The scintillation index is a little lower than the theoretical value of $4 \times 0.046 = 0.18$. This might be due to an aperture averaging effect

caused by the resolution of the optical field at the receiver. These results confirm the simulation operates as expected and should adequately model the turbulence [46].

For each propagation length, the irradiance and phase of the Gaussian beams after propagating through a vacuum matched the analytical solution. The structure function of each of the phase screens was also consistent with the theoretical values. The scintillation index at the receiver for a simulated point source was consistent with the Rytov approximation for scintillation. For each turbulence simulation, the measured long-term spot size was consistent with the analytic spot size. These results confirmed the simulation operated as expected and should adequately model the turbulence [46].

4.3 Modeling optical receiver signals and noise sources

The received signal is converted from optical power to receiver current in the detector. The receiver current, which is called the measured current i_m , is the sum of the signal current and noise current and is given by

$$i_m = i_s + i_N. \quad (167)$$

Since simulations are used to “measure” the performance, it is imperative to model these realistically. First, the signal current can be represented by [18, 19]

$$i_s = \frac{\eta q s}{h\nu}, \quad (168)$$

where η is quantum efficiency (electrons/photon), $q = 1.602 \times 10^{-19}$ C is the elementary charge, s is optical power at the detector (Watts), $h = 6.626 \times 10^{-34}$ J·s is Planck’s constant, and ν is optical frequency (Hz). The product $h\nu$ gives the energy in joules of a single photon. The noise current i_N is modeled as a zero-mean Gaussian

random variable with a variance σ_1^2 equal to

$$\text{E} [i_N^2] = \sigma_1^2 = \sigma_{elec}^2 + \sigma_{shot}^2 + \sigma_{ASE}^2, \quad (169)$$

where σ_{elec}^2 is the thermal (Johnson) noise, σ_{shot}^2 is the shot noise, and σ_{ASE}^2 is the ASE noise associated with an EDFA. Since each of these noise current sources are independent the overall noise current variance σ_1^2 is the sum of each noise source variance. Modeling receiver noise sources is essential to accurately represent a communication system. Two fundamental noise sources for optical receivers are the signal-level-dependent shot noise and the temperature-dependent Johnson noise. Shot noise σ_{shot}^2 is fundamentally a Poisson random process as the photo-electrons are generated for random arrivals of photons. The number of photons per bit is well over 100 in all cases studied here. Furthermore, as the captured power approaches zero, the shot noise approaches zero much faster than the signal. Therefore, shot noise current statistics are well approximated as a zero-mean Gaussian random process [1, 3]. The mean-square current due to shot noise is given by [19]

$$\text{E} [i_{shot}^2] = \sigma_{shot}^2 = 2q i_S B = \frac{2\eta q^2 s B}{h\nu}, \quad (170)$$

where B is the electrical bandwidth. The signal current is assumed to be constant during any given integration period corresponding to a single bit. Comparing the frequency of atmospheric change (\approx kHz) with bandwidths studied (\gg MHz), this is a reasonable assumption.

Johnson (thermal) noise current is typically modeled as a zero-mean Gaussian random variable, with mean-square current determined by [19]

$$\text{E} [i_{elec}^2] = \sigma_{elec}^2 = \frac{4KTB}{R}, \quad (171)$$

where $K = 1.381 \times 10^{-23}$ J/K is Boltzmann's constant, T is temperature of the electronics (K), and R is the effective input resistance (ohms). These are the primary noise sources in the receiver.

There is also noise due to the type of amplifier or gain mechanism. In this research, the received optical signal is coupled into an optical fiber to be amplified by an EDFA. The EDFA's advantage is the capability to achieve high gain at very high bandwidths. In addition, the gain in an EDFA saturates, affording some gain control to reduce optical signal variation. This reduces the required dynamic range of the detector. The EDFA's noise is due to amplified stimulated emission and can be modeled as a signal-dependent zero-mean Gaussian noise source given by [1]

$$\begin{aligned} E [i_{ASE}^2] = \sigma_{ASE}^2 &= 4q^2 n_{sp} \eta_{in} \eta_{out}^2 G(G-1) \frac{P}{h\nu} B \\ &= 4n_{sp} \eta_{out} q(G-1) i_s B, \end{aligned} \quad (172)$$

where G is the gain, η_{in} and η_{out} are the input and output losses, and n_{sp} is the spontaneous emission factor. Other gain mechanisms like avalanche photo diodes (APD) are limited to about 100-200 GHz gain-bandwidth product, whereas an EDFA with a PiN photodiode would be at least an order of magnitude higher [1]. For lower bandwidths an APD is advantageous due to a much higher coupling efficiency.

4.4 *Simulation approach*

The receiver consists of a 20-cm-diameter lens with a 1 m focal length focused onto a single-mode optical fiber. The fiber core's diameter was 3 μ m and the numerical aperture (NA) was 0.20, consistent with a commonly available EDFA. For the 100 km propagation, the collimated Gaussian beam at the Rx is much larger than the aperture and since $r_0 > D$ the spot size at the focal plane of the lens is determined by $2.44\lambda f/D$, limited only by diffraction. For the ground-to-ground and ground-to-air cases the turbulence-induced spot size is approximately $2.44f\lambda/r_0$, since $r_0 < D$ for those cases. See Table 2 and Fig. 18.

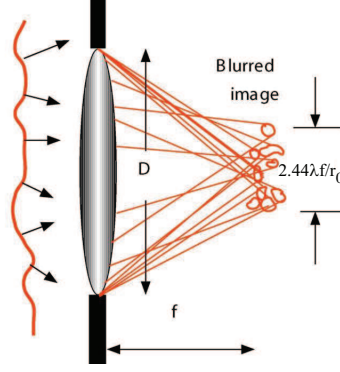


Figure 18: When $D < r_0$, the spot size is determined primarily by diffraction $2.44\lambda f/D$. Where as when $D > r_0$, the spot size spreads primarily due to the turbulence, leading to a much wider spot determined by $2.44\lambda f/r_0$ [46].

For the angularly-separated-beam scenario, two Gaussian beams are displaced half the separation distance in opposite y-directions and a linear phase is applied to “aim” both beams at the center of the receiver aperture. For the parallel-beam case, the two Gaussian beams are displaced, and each beam remains off-axis by half the separation distance.

A coarse tracking system was simulated for the transmitter and receiver for the ground-to-air and the air-to-air paths by implementing an ideal centroid tracker and adding random tracking system errors. The errors in the Tx tracker σ_j^2 are driven by tilt isoplanatism σ_{TA}^2 due to the point-ahead angle, temporal errors σ_{TT}^2 in the controller, platform jitter σ_{PJ}^2 , and measurement error σ_{TM}^2 . Therefore the total transmitter tracker error is [31, 46]

$$\sigma_j^2 = \sigma_{TA}^2 + \sigma_{TT}^2 + \sigma_{PJ}^2 + \sigma_{TM}^2, \quad (173)$$

measured in rad^2 of the tilt angle. The tilt anisoplanatic error is driven by the separation angle size compared to the tilt isoplanatic angle and given by [31]

$$\sigma_{TA}^2 = \left(\frac{kD}{4}\right)^2 \sigma_T^2 \left(\frac{\theta}{\theta_{TA(1 \text{ rad})}}\right)^2, \quad (174)$$

in rad^2 of the tilt angle where θ is the angle between the propagation path and the beacon path. This tilt anisoplanatic error requires a different tilt isoplanatic angle $\theta_{TA(1rad)}$ definition than the one previously mentioned in Eq. (154). This new definition of $\theta_{TA(1rad)}$ is the angle between two beams at which the wavefront phase error due to the tilt anisoplanatism is 1 rad, resulting in

$$\theta_{TA(1 \text{ rad})} = \frac{0.1947\lambda D^{1/6}}{\mu_2^{1/2}}. \quad (175)$$

The required point-ahead angle determines the inherent angular separation of the beacon and the transmit path. The point-ahead angle for the ground-to-air path is [31]

$$\theta_{PA} = \frac{V_p}{c} \sin \xi, \quad (176)$$

where V_p is the platform velocity and c is the speed of light. This angle can be substituted for θ in Eq. (174). The temporal error is [31, 66]

$$\sigma_{TT}^2 = 2 \left(\frac{f_T}{f_{3dB}} \right)^2 \left(\frac{\lambda}{D} \right)^2, \quad (177)$$

and the tilt measurement error is [31]

$$\sigma_{TM}^2 = 2 \left(\frac{3\pi \times 1.4 \times \lambda}{16SNR r_0} \right)^2. \quad (178)$$

The temporal error is dependent on the tracking system bandwidth, and the tilt measurement error depends upon the signal-to-noise ratio (SNR). The platform jitter is driven by the transmitter and receiver's residual vibrations. The receiver tracker error includes the last three terms of Eq. (173).

4.5 *Simulation results*

The simulations used independent random realizations of the appropriate turbulence statistics to determine the optimal separations for a two-transmitter system

in three scenarios: a ground-to-ground fixed transmitter and receiver 4 km link with a Rx and Tx height of 1 m, a ground-to-air ($h = 1$ m to 10 km) 30.2 km path with a zenith angle $\xi = 70^\circ$, and an air-to-air 100 km path at 10 km in altitude [46]. This approach assumes that the turbulence can be approximated by an ergodic random process where the temporal statistics can be approximated by the ensemble statistics.

4.5.1 Differential irradiance and tilt variance. A number of performance measurements were calculated, but the differential irradiance variance between the two beams $\sigma_{\Delta irr}^2 = E[(I_1 - I_2)^2] - E[I_1 - I_2]^2$ best indicated when adequate averaging would occur. [5, 60, 68] The larger the differential irradiance variance, the less correlated the irradiance fluctuations become. For uncorrelated beams this variance should approach two times the irradiance variance of a single beam. If the angular separation is much beyond this point, the power received at the detector or fiber is reduced due to the difference in the AOA of the beams. As parallel beams move farther off-axis, power reduces and the variability of the constituent beams increases. This effect increases the double-Tx system BER, driving the performance below the single-Tx case [46].

A 4 km ground-to-ground propagation was performed with the same beam parameters as the 29.2 km propagation path. This beam wandered off the receiver frequently. The beam walk-off standard deviation was 0.095 m while the short term beam half-width was 0.083 m. Again, the optimal separation for this scenario was about $3\rho_c$. The irradiance variance was much higher than the other scenarios since the beam wandered off the receiver often. In Fig. 19a the differential irradiance variance approached two times the single irradiance variance at about $3\rho_c$. Figure 19b shows that in the y-direction (parallel to the separation) the two beams start to wander independently for narrow separations whereas in the x-direction (perpendicular to the beam separation) the beams wander independently at approximately $d_{\psi_{ind}}/2$. The differential tilt variance approached two times the single tilt variance very quickly in the direction parallel to the separation, but for the perpendicular direction the

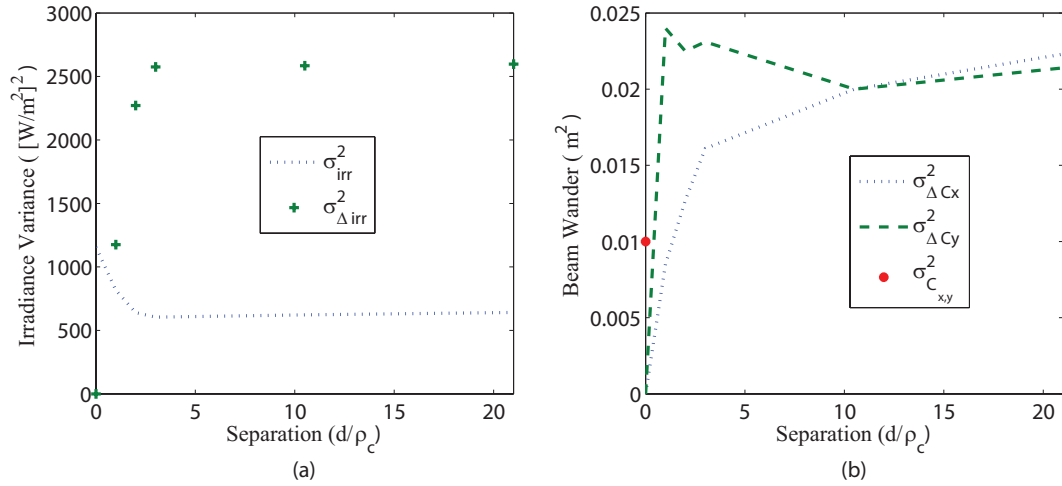


Figure 19: Ground-to-Ground untracked case. Propagation length of 4 km, at 1 m above the ground, collimated beam with $W_0 = 0.025$ m. (a) This plot shows how the differential irradiance variance approaches 2 times the single beam irradiance variance. (b) This plot shows that in the y-direction (parallel to the separation) the two beams start to wander independently for narrow separations whereas in the x-direction (perpendicular to the beam separation) the beams wander independently at approximately $d_{\psi_{ind}}/2$ [46].

required separation distance for uncorrelated phase was 10 to 15 ρ_c or about $d_{\psi_{ind}}/2$. This is consistent with the phase independence angle which includes both separation directions. This is also consistent with Sasiela's relations in Eqs. (150) and (151), where the tilt component parallel to the displacement is 1.73 times the perpendicular component for small displacements and approaches equality for very large displacements [46, 69].

Next, Fig. 20 shows the differential irradiance variance and the differential centroid variance for the air-to-air scenario shown in Table 2. In Fig. 20a at 2 and 3 ρ_c , the differential variance reaches a maximum. Fig. 20b shows the differential centroid variance continues as the separation between the transmitters increases because the outer scale L_0 and corresponding $d_{\phi_{ind}}$ for this propagation is very large [46].

As shown in Fig. 21, beams approached uncorrelated irradiance variance at about 2-3 ρ_c for angularly separated beams for both the air-to-air tracked system and the ground-to-air tracked system. In addition, for the air-to-air scenario the amplitude

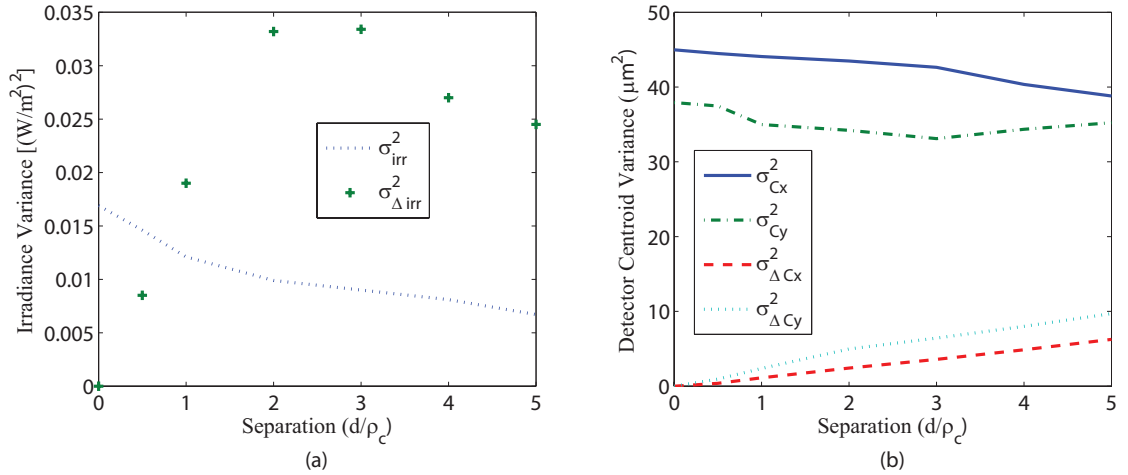


Figure 20: 100km air-to-air propagation path at a 10 km altitude for a collimated $W_0 = 2.5$ cm beam (a) differential beam irradiance variance, and (b) differential centroid location variance [46].

structure function (shown in Fig. 14) has a peak before settling into the asymptotic value of two times the the single-beam irradiance variance [46].

4.5.2 Bit error rates for independent realizations. The BER for the different scenarios, tracking systems, and separation distances are shown in Figs. 22 - 25. The BERs were calculated using the PDF of the measure signal current (determined by the histogram of the received signal), accounting for the shot, thermal, and ASE noise. Since the shot and ASE noise are signal-dependent, their variances changed for each independent realization, while the thermal noise variance was fixed. After solving for the optimal fixed threshold, the probabilities of missed detection and false alarm were determined. The total power in the single-Tx system was 1 Watt, and the total power in the double-Tx system was also 1 Watt (0.5 Watts per transmitter). For the BER plots, the EDFA gain remained constant at 30 dB. The signal level differences shown in the plots vary due to differences in propagation attenuation, coupling efficiencies, transmitter levels, etc., but do not depend on the EDFA gain [46].

First, the BER for the ground-to-ground path for single and double-Tx systems were calculated. No tracking system was used in this case, and the beams walked off

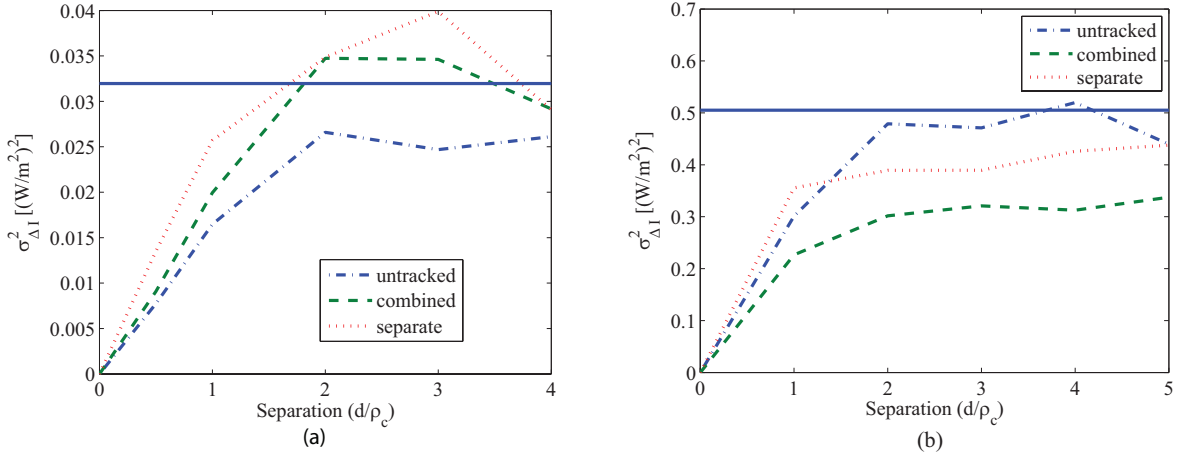


Figure 21: Differential irradiance variance for two angularly separated beams. Irradiance is taken from the center of the untracked beams, separately tracked beams, and a single combined beam tracker. The solid blue line is two times the variance of on-axis irradiance of a single beam. The differential variance approaches two times this value as the separation increases. (a) Air-to-air path angular separation (b) Ground-to-air path angular separation [46].

of the receiver often. To quantify this, note that the beam walk-off standard deviation was 9.5 cm and the short-term beam half-width was 8.3 cm. The differential tilt variance approached two times the single tilt variance in the direction parallel to the separation for very small separations (i.e. 3 cm). However, for the perpendicular direction the required separation distance for uncorrelated phase was about $10 \rho_c$ or about $d_{\psi_{ind}}/2$. This phenomenon is consistent with the differential tilt relations presented by Sasiela [69]. Figure 22 shows slight improvement for the double transmitter case over the single beam when the transmitters propagated in parallel, but no improvement for angular separations. Due to the inherent non-zero mean AOA for angularly separated beams, the focal spots of both beams on average miss the fiber, reducing the coupling efficiencies. If the fiber core is small, as in this case, this could severely limit the coupling of both beams. Whereas with the parallel beams, both focal spots were on average on the center of the fiber, allowing for much better coupling [46].

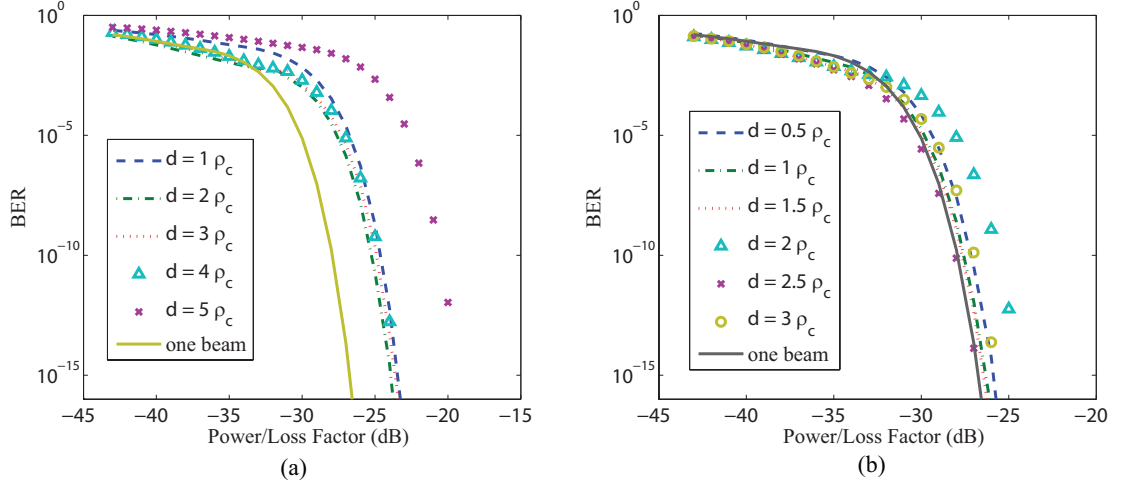


Figure 22: These plots show the BER for a ground-to-ground link. In plot (a) the beams were angularly separated and in plot (b) the beams were separated, but traveled in parallel [46].

Next, the BER plots for the tracked ground-to-air scenario in Fig. 23 show that there is an improvement afforded by using two transmitters of about 3 dB for the ideal tracker. Interestingly, two transmitters also improved performance for the non-ideal case for a tracker error of $\sigma_j = \lambda/(4D)$. Parallel beams were used with a center tracker system. For this case, Fig. 24 shows an improvement again for a tracking system with $\sigma_j = \lambda/(4D)$. This improvement reduces in both cases as the tracking system performance degrades [46].

Finally, the BER plots in Fig. 25 for the air-to-air 100 km path shows the best improvement for a separation distance of 2 to 3 ρ_c . This is consistent with the differential scintillation measurements. The largest improvement (approximately 4 dB) occurs for the finest tracking system. As the tracking degrades, the improvement due to the signal diversity decreases.

For all cases studied here, a separation of a small multiple of ρ_c was sufficient to provide adequate averaging. These separations were consistent with the coherence width described by Andrews and Phillips [2]. The amplitude independence separation distance $\Delta x_{\chi_{ind}}$ and angle $\theta_{\chi_{ind}}$ for these scenarios are approximately $2\rho_c$ and

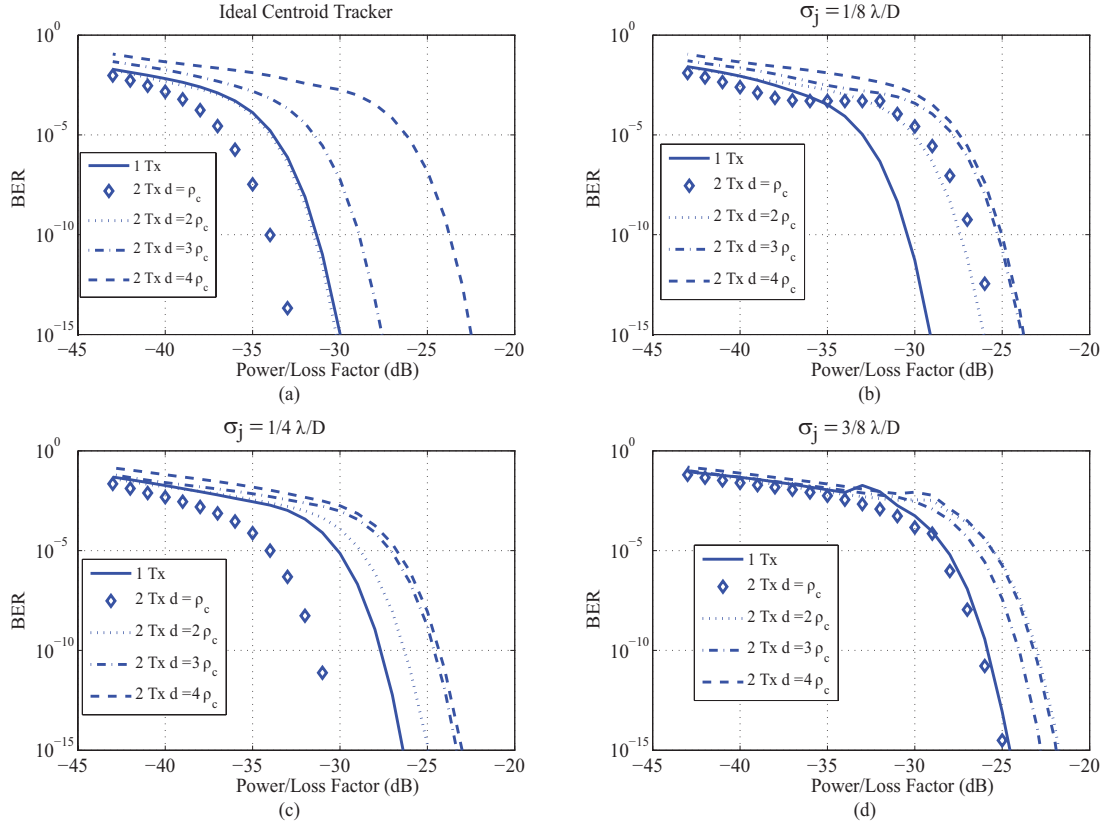


Figure 23: Bit error rate for a ground-to-air link with angularly separated beams using various tracking systems (a) ideal centroid tracker, (b) $\sigma_j = \lambda/(8D)$, (c) $\sigma_j = \lambda/(4D)$, and (d) $\sigma_j = 3\lambda/(8D)$ [46].

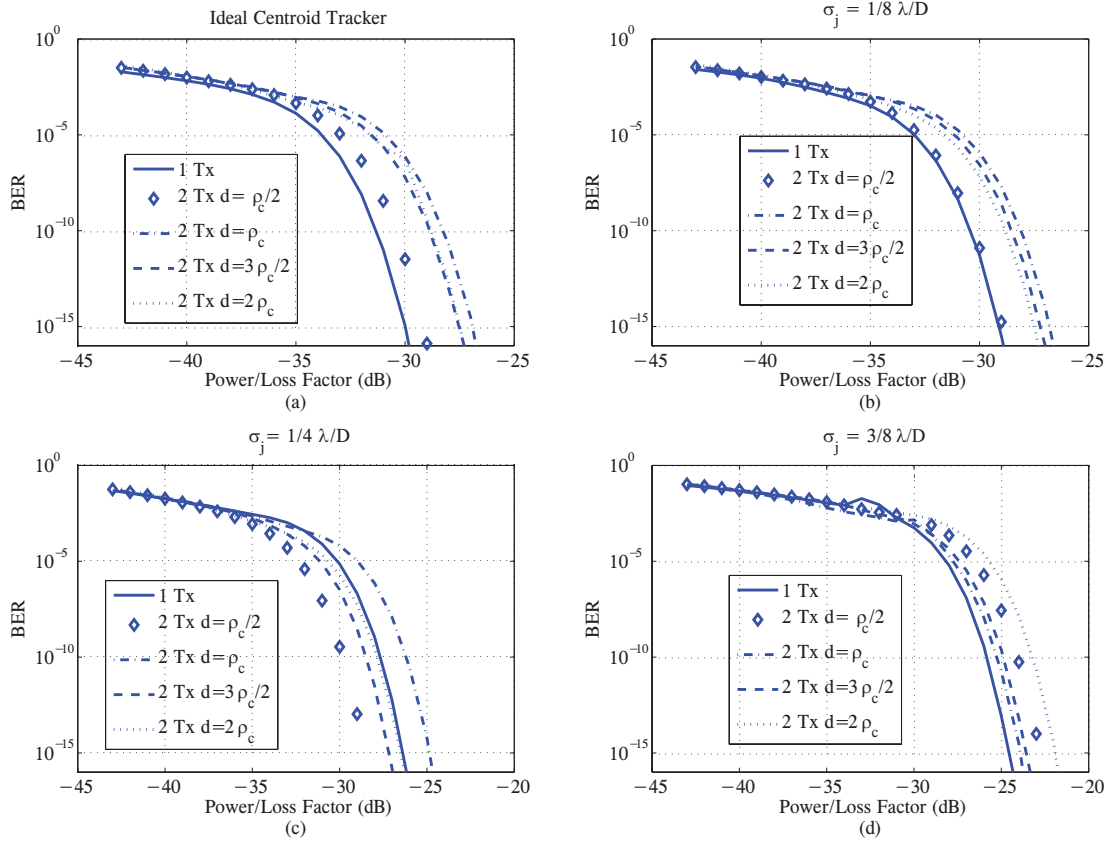


Figure 24: Bit error rate for a ground-to-air link with parallel separated beams using various tracking systems (a) ideal centroid tracker, (b) $\sigma_j = \lambda/(8D)$, (c) $\sigma_j = \lambda/(4D)$, and (d) $\sigma_j = 3\lambda/(8D)$ [46].

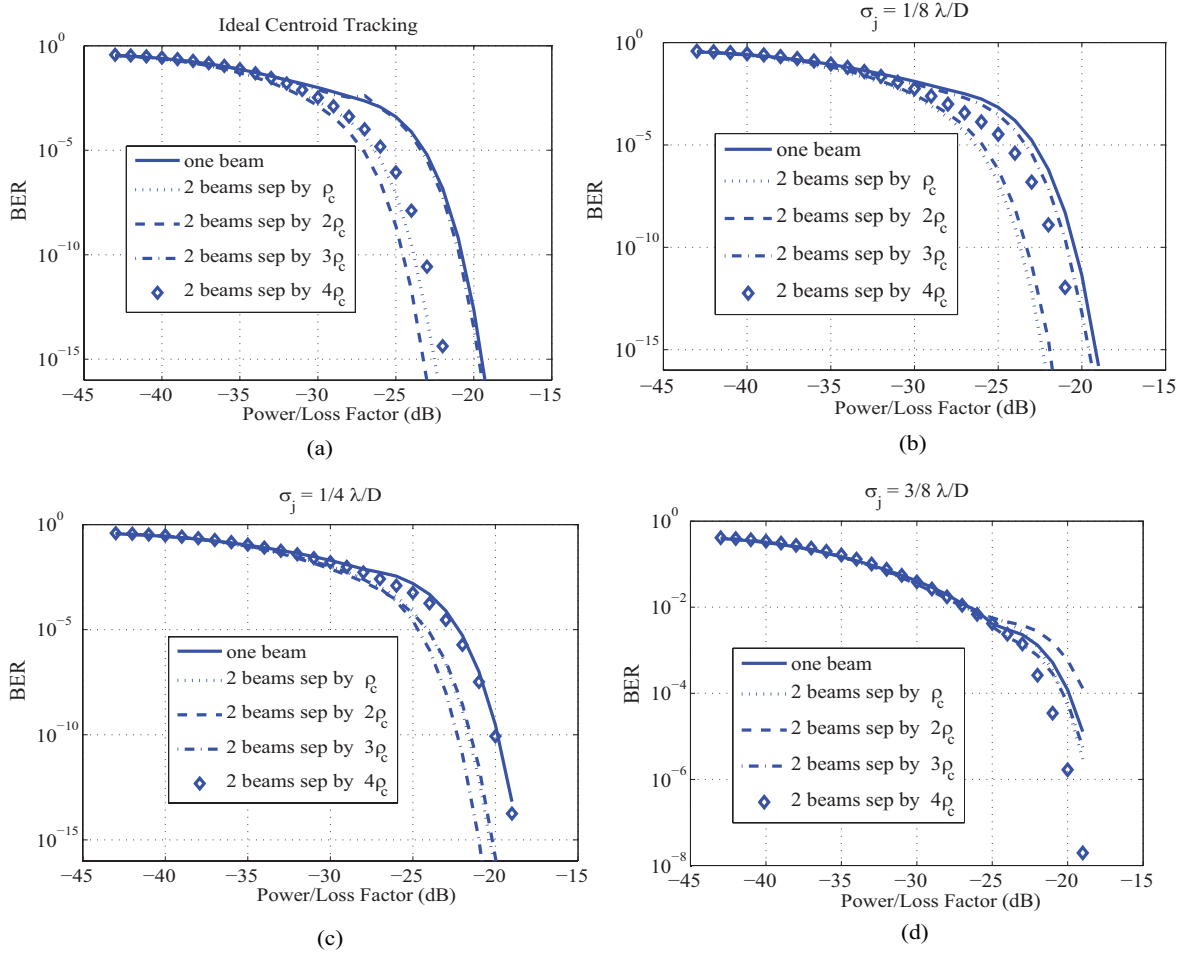


Figure 25: BER for Air-to-air 100km path at 10km altitude using various tracking systems (a) ideal centroid tracker, (b) $\sigma_j = \lambda/(8D)$, (c) $\sigma_j = \lambda/(4D)$, and (d) $\sigma_j = 3\lambda/(8D)$ [46].

Table 3: Optimal separation distances for multiple Tx systems.

Scenario	Tx Alt	Rx Alt (km)	Prop Dist	Best Tx Separation
G-to-G Angular	1 m	1 m	4 km	not conclusive
G-to-G Parallel	1 m	1 m	4 km	$2.5\rho_c = 7.9$ cm
G-to-A Angular	1 m	10 km	29 km	$\rho_c = 8.6$ cm
G-to-A Parallel	1 m	10 km	29 km	$\rho_c/2 = 4.3$ cm
A-to-A Angular	10 km	10 km	100 km	$2\rho_c = 31$ cm

$2(Lk)^{-1/2}$, respectively. Table 3 shows the optimal separation distances for the three scenarios tested in this section.

The optimal separation for the air-to-air 100 km path scenario at 10 km in altitude was only 31 cm. The scintillation for this air-to-air scenario is relatively high at $\mathcal{R}_{sph} = 0.155$ whereas the phase effects characterized by $D/r_{0_{sph}} = 0.49$ are relatively low. This indicates that a technique to reduce scintillation like the multiple-transmitter system tested here in this chapter has advantages over AO systems for the air-to-air scenario. The next chapter studies this air-to-air scenario further by implementing a time-series simulation to study the temporal effects of multiple transmitters. Chapter V also studies the trickle-down effects of additional techniques to include centroid tracking and adaptive-threshold systems.

V. Temporal Analysis and Signal Processing

This research shows how multiple transmitters reduce received signal variability and the length of a fade caused by long propagation paths through extended turbulence in FSOC systems. Many researchers have studied how adaptive optics systems can improve FSOC system performance especially in satellite communications [7,77,81]. These conventional AO systems correct for the phase only and cannot correct for strong scintillation, but here multiple transmitters “average out” strong scintillation effects by incoherently summing up multiple beams at the receiver. Others have done research on MIMO and multiple transmitter FSOC systems [30,43,60], but have not delved into the anisoplanatic separations required and the temporal considerations of tracking systems and fade statistics for the airborne regime.

Here, two mutually incoherent laser beams angularly separated by the irradiance independence (anisoplanatic) angle [46] average the scintillation effects and reduce the fade length, depth, and number per second. Wave-optics simulations show that a combination of transmitter diversity, adaptive thresholding, and tracking systems significantly reduce the BER in air-to-air FSOC. The reduction in fade length indicates multiple beams might provide even greater improvement when coupled with interleaving and FEC coding.

5.1 Spatial statistics

The spatial statistics of the turbulence effects are required to determine the simulation parameters. This research simulates a 100 km air-to-air path and isolates the phase (spherical coherence diameter $r_{0,sp}$) and amplitude (spherical Rytov number \mathcal{R}_{sp}) effects by adjusting the turbulence profile. The \mathcal{R}_{sp} is equal to the spherical log-amplitude variance $\sigma_{\chi,sp}^2$ for weak turbulence [69]. The parameters were chosen to emulate this air-to-air horizontal scenario with aircraft velocities between 56 and 280 m/s and altitudes between 4 and 15 km. These parameter ranges were chosen because of the results in Fig. 25 of Section 4.5 that show a relatively small separation of about 31 cm ($2\rho_c$) is required to average scintillation effects for the air-to-air scenario.

Table 4: Atmospheric parameters for the scenarios used in the simulations. The optical wavelength was $\lambda = 1.55 \mu\text{m}$.

Scenario	Alt. (km)	Velocity (m/s)	Δt (μs)	\mathcal{R}_{sp}	f_G (Hz)	$r_{0_{sp}}$ (cm)
1	15	113	133	0.0596 (L)	117 (L)	74 (H)
2	4	56	137	0.1827 (H)	113 (L)	38 (L)
3	N/A	280	30	0.0854 (L)	518 (H)	38 (L)
4	N/A	280	30	0.1979 (H)	518 (H)	55 (H)
5	4	225	30	0.1827 (H)	518 (H)	38 (L)

The experimental design fully investigates the different scenarios and conditions of an air-to-air scenario. Since $r_{0_{sp}}$, \mathcal{R}_{sp} , and f_G adequately describe the spatial and temporal turbulence effects, the simulated conditions consist of a one half fractional factorial of these three factors. Designing the test in this way enables the determination of the primary driving factors for fades and bit errors. Table 4 summarizes the atmospheric parameters for the simulations. There are five different scenarios with different altitudes (km), air velocities (m/s), sampling times (μs), spherical Rytov numbers \mathcal{R}_{sp} , Greenwood frequencies f_G (Hz), and spherical coherence diameters $r_{0_{sp}}$ (cm).

The spatial statistics of the turbulence effects also determine how far apart the transmitters must be to get good averaging. The farther the two transmitters are separated, the more uncorrelated the effects become (i.e. anisoplanatic). This is important when multiple transmitters are used to average out the turbulence effects. Next, the anisoplanatic phase and amplitude effects are considered.

5.1.1 Anisoplanatic effects. For a multiple-Tx system, the phase and amplitude fluctuations decorrelate as the beam separation increases in distance or angle. Starting at small separations, high-order and low-order phase effects are highly correlated for Tx separations less than or equal to the isoplanatic angle θ_0 . Most of the literature defines this angle as when the phase perturbation structure function is less than or equal to unity, leading to Eq. (137) in Chapter IV [26]. Applying the maximum value of the phase perturbation structure function determines the phase

independence angle. At this separation, the high-order and low-order phase effects of multiple beams are relatively uncorrelated, spreading and wandering independently. This angle was defined in Eq. (139) and shown here again as [46, 49]

$$\theta_{\psi_{ind}} = 2\sigma_{\psi,pl}^2\theta_0, \quad (179)$$

where $\sigma_{\psi,pl}^2$ is the phase variance for a plane-wave source and a point receiver, given in Eq. (140).

As for the amplitude effects, the correlation width ρ_{cw} is often used to determine how large receivers need to be to provide some degree of aperture averaging of the scintillation effects. The correlation width is defined as the $1/e^2$ point of the normalized irradiance covariance function [2]. Since ρ_{cw} for weak turbulence, varies between 1 to 3 Fresnel zones $(L/k)^{1/2}$ depending on beam size, [2] in this work it is referred to as simply $\rho_c = (L/k)^{1/2}$. In recent work, the principle of reciprocity was used to illustrate how ρ_c could determine how far apart transmitters need to be to provide adequate averaging in the receiver [46, 49]. Due to AOA considerations, the increase in off-axis irradiance variance, and negatively correlated amplitude effects near ρ_{cw} , very wide separations are not necessarily the optimal configuration [2, 5, 46, 49, 60]. Therefore, this research separates the beams angularly by $2\theta_{\chi_c} = 2(Lk)^{-1/2}$, or a separation of $2\rho_c$ at the transmitters, as determined in Chapter IV.

5.2 Temporal considerations

Thus far, spatial statistics were used to describe the effects of atmospheric turbulence. In this section, the temporal statistics are considered to determine BER improvement afforded by tracking systems and adaptive thresholding. Taylor’s frozen flow hypothesis states that the turbulence structure is essentially frozen as it moves across the propagation path for small time intervals [66]. The random screens “scroll” across the laser beam at different points along the path to generate a time-series of the turbulence in the simulations described in Sections 5.3 and 5.4.

5.2.1 *Frequency of the turbulence effects.* The first thing to consider when building a temporal simulation is the sampling frequency. One approach is to determine the frequency of the irradiance, given by $f_{irr} = 1/\tau_{irr}$, passing over the Rx aperture where τ_{irr} is the characteristic time of the irradiance. Over the time τ_{irr} the turbulence evolves so that the effects are only slightly different than the previous time slice (isoplanatic time difference). The average time it takes one anisoplanatic irradiance patch to scroll across the aperture is

$$\tau_{\chi_{ind}} \approx \frac{2\rho_c}{|V(z)|} \approx \frac{1}{2.8f_G}, \quad (180)$$

where $|V(z)|$ is the transverse velocity of the turbulence and f_G is the Greenwood frequency (characteristic atmospheric frequency defined in terms of the 3dB bandwidth for a high-order phase controller) [66, 69]. The irradiance at the edges of this time period $\tau_{\chi_{ind}}$ are anisoplanatic. That is to say, after this time period the irradiance is relatively uncorrelated with the previous time slice.

These simulations use a conservative estimate of τ_{irr} to ensure they include all potential signal variations. Using f_G as a reference and varying the temporal sampling frequency of the simulations enables the determination of an adequate sampling rate. The received signal power spectral density (PSD) for increasingly finer resolutions is calculated until the PSD is relatively similar over 20 dB down from the maximum value. This determination is shown graphically in Fig. 26. These PSDs were consistent for different random realizations. The resulting sampling frequency is $f_{sirr} = 64f_G$. At first, it seems like this frequency is very high, but the Greenwood frequency is a measure of the higher-order *phase* temporal variations. *Amplitude* variations occur at much smaller scale than phase effects and therefore require finer spatial and temporal resolutions [2, 46]. These results were determined for a 100 km path with a turbulence velocity of 225 m/s (503 miles/hr) and $f_G = 518$ Hz. Temporal plots of the signal variation appear smooth to the eye, indicating again that the sampling is adequate (see Fig. 29).

How does this temporal separation τ_{irr} relate to the spatial correlation of the irradiance in terms of ρ_c ? To adequately sample the irradiance requires sampling at the Nyquist frequency, which requires

$$f_{s_{irr}} = 2 \times f_{irr}. \quad (181)$$

Since $f_{s_{irr}} = 64f_G$ is known to be adequate from the PSD analysis in Fig. 26, it is instructive to determine what fraction of ρ_c is adequate to satisfy

$$\tau_{irr} = \frac{\rho_c/x}{|V(z)|}. \quad (182)$$

Solving for x in the above equation, results in

$$x = \frac{\rho_c f_{s_{irr}}}{2|V(z)|} = 12. \quad (183)$$

Finally, this yields the following irradiance time constant

$$\tau_{irr} = \frac{\rho_c/12}{|V(z)|}. \quad (184)$$

This relation can be used to determine the sampling rate f_s in simulations with significant irradiance fluctuations without having to calculate the PSD of the receiver irradiance. The separation $\rho_c/12$ is shown in Fig. 27 using the structure functions previously shown in Fig. 14. The separation of $\rho_c/12$ could be considered the scintillation isoplanatic separation distance for angular paths, corresponding to a scintillation isoplanatic angle of $\theta_{\chi_0} = (\rho_c/12)/L$.

5.2.2 Threshold determination. For a binary symbol system like the one used here, once the signal is received a decision must be made based on a threshold whether a ‘1’ or a ‘0’ was sent. The transmitter modulates with OOK, where the laser turns on to transmit a ‘1’ and turns off to transmit a ‘0’. The transmission of a ‘1’ or ‘0’ is equally likely, denoted by the events H_1 and H_0 , respectively. The likelihood

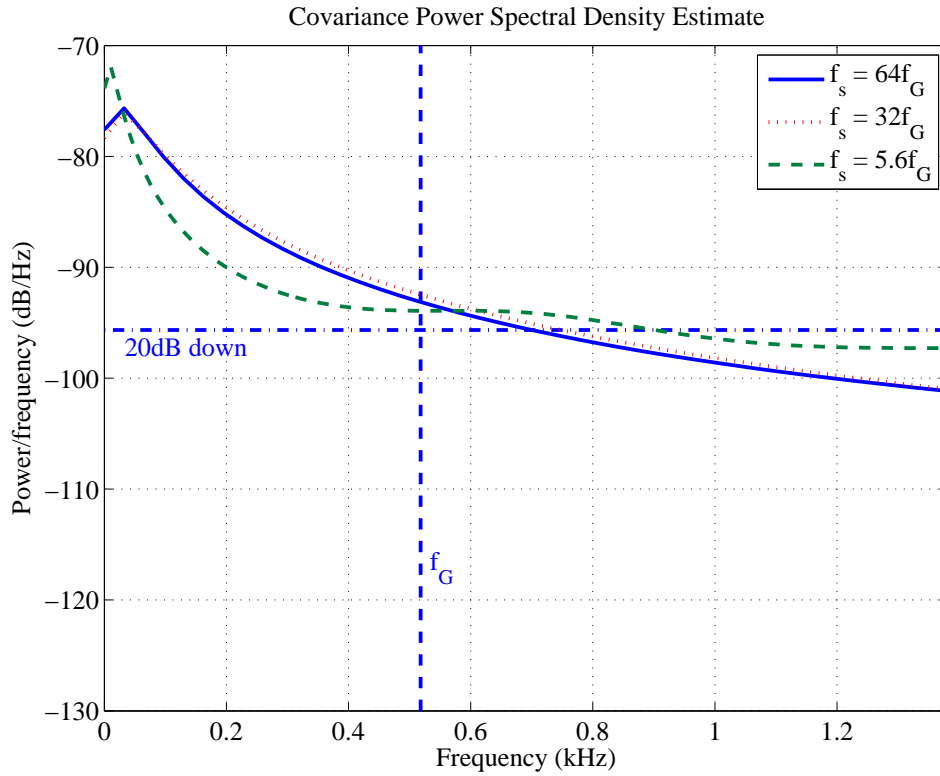


Figure 26: Received signal power spectral density (PSD) for an air-to-air 100 km path at 4km in altitude. The PSD of the signal is sampled at $f_s = 64 \times f_G$ shown with a solid line, at $f_s = 32 \times f_G$ with a dotted line, and at $f_s = 5.6 \times f_G$ with a dashed line. The horizontal dot dash line is 20 dB down from the peak value. The vertical dashed line is the Greenwood frequency f_G .

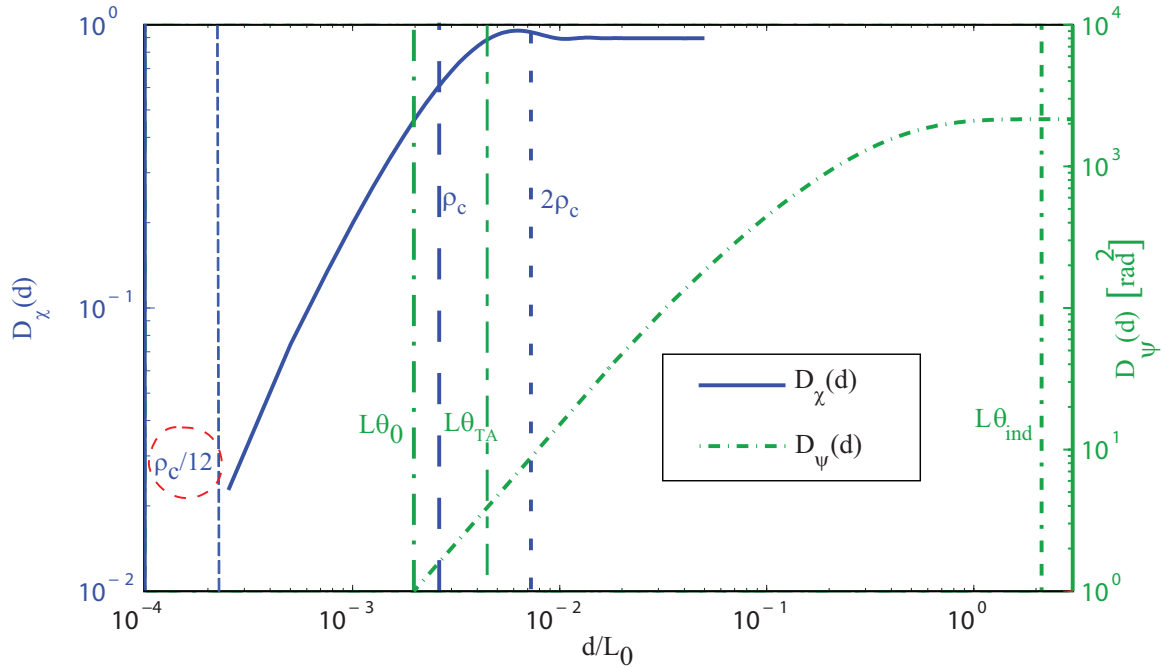


Figure 27: Phase (right scale) and log-amplitude (left scale) structure functions are plotted for a 100 km horizontal propagation at 10 km altitude, with angularly separated beams. The strength of turbulence is $L_0/r_0 = 286$ and $L_0^2/(\lambda L) = 23225$. [46] Isoplanatic and anisoplanatic separation distances are shown for the amplitude and phase effects. The amplitude isoplanatic separation distance, $\rho_c/12$ is circled with a dashed line.

ratio test (LRT) from Eq. (128) determines the optimal decision threshold based upon the discretized PDF of the measured current level i_m of the transmission of a ‘1’ $p(i_m|H_1)$ and transmission of a ‘0’ $p(i_m|H_0)$. Using the LRT and the assumption that $P(H_0) = P(H_1)$ (equally likely signaling) leads to the following two relations; [82] if

$$p(i_m|H_1) > p(i_m|H_0) \quad (185)$$

then the algorithm picks H_1 and if

$$p(i_m|H_1) < p(i_m|H_0) \quad (186)$$

then the algorithm picks H_0 . The optimum detection criteria can best be described graphically as shown in Fig. 11 and reported in Section 2.6.3. These turbulence conditions vary significantly over time and thus could benefit from a threshold that varies with the optical signal level [13, 18].

5.2.2.1 Fixed Threshold. The fixed threshold calculation takes into account the PDF of the signal $p(s)$ due to variations caused by channel conditions. In this case, the channel conditions are dictated by the atmospheric turbulence conditions. To simplify the notation, let $p_1(i_m) = p(i_m|H_1)$ and $p_0(i_m) = p(i_m|H_0)$. The LRT for this scenario is [18, 72]

$$P(H_0)p_0(i_m) = P(H_1) \int_0^\infty p_1(i_m|s)p(s)ds \quad (187)$$

$$\frac{1}{\sigma_{elec}} \exp\left(\frac{-i_T^2}{2\sigma_{elec}^2}\right) = \int_0^\infty \frac{p(s)}{\sigma_1(s)} \exp\left[\frac{-(i_T - i_m(s))^2}{2\sigma_1^2(s)}\right] ds. \quad (188)$$

The threshold i_T current can be solved for numerically whether the PDF of the turbulence induced power fluctuations $p(s)$ is analytic or calculated from the discretized PDF of the simulated received power before the measurement noise is applied. Since this is a simulation, the PDF $p(s)$ is calculated from the raw received signal before the noise is applied. The noise associated with detecting a ‘0’ is primarily due to thermal

noise as shown in Eq. (171). The noise associated with detecting a ‘1’ can be broken into the sum of the thermal, shot, and amplifier noise, defined by

$$\sigma_1^2 = \sigma_{elec}^2 + \sigma_{shot}^2 + \sigma_{ASE}^2, \quad (189)$$

where σ_{shot}^2 is the shot noise due to the random arrival of photons [see Eq. (170)] and σ_{ASE}^2 [See Eq. (172)] is the amplified stimulated emission noise associated with an Erbium-doped fiber amplifier [1,46]. The probability of an error P_e is the probability of a missed detection P_{md} plus the probability of a false alarm P_{fa} :

$$P_e = P(H_1)P_{md} + P(H_0)P_{fa} = \frac{P_{md}}{2} + \frac{P_{fa}}{2}, \quad (190)$$

where

$$P_{md} = \frac{1}{2} \int_0^\infty \text{erfc} \left(\frac{i_m(s) - i_T}{\sqrt{2}\sigma_1(s)} \right) p(s) ds, \quad (191)$$

$$P_{fa} = \frac{1}{2} \text{erfc} \left(\frac{i_T}{\sqrt{2}\sigma_{elec}} \right). \quad (192)$$

The $\text{erfc}(x)$ is the complementary error function in Eqs. (191) and (192).

5.2.2.2 Adaptive threshold. For this temporally varying turbulence, an *ideal* optimal adaptive threshold shows the best possible BER improvement. Since the threshold is determined for each current level, the PDF of the received signal level $p(s)$ is not required for this calculation. Only the estimates of the mean and variance of the two conditions are required to set the threshold. Solving for the optimal adaptive threshold current yields [14,18]

$$i_T = \frac{\mu_0\sigma_1^2 - \mu_1\sigma_0^2}{\sigma_1^2 - \sigma_0^2} + \frac{\sigma_0\sigma_1}{\sigma_1^2 - \sigma_0^2} \sqrt{(\mu_1 - \mu_0)^2 + 2(\sigma_1^2 - \sigma_0^2) \ln \left(\frac{\sigma_1}{\sigma_0} \right)}. \quad (193)$$

The work here assumes $\mu_0 = 0$ and $\sigma_0 = \sigma_{elec}$, since $\sigma_{shot} = \sigma_{ASE} = 0$ when a ‘0’ is sent. This *ideal* adaptive threshold system calculates the optimal adaptive threshold

for each time slice with the corresponding raw received signal level s in the simulation and implements that threshold to determine whether it is a ‘1’ or a ‘0’.

For the adaptive threshold case the probability of a missed detection and the probability of false alarm now have a threshold that varies with the signal level along with all of the other signal dependent terms. The P_{md} becomes

$$P_{md} = \frac{1}{2} \int_0^\infty \operatorname{erfc} \left(\frac{i_m(s) - i_T(s)}{\sqrt{2}\sigma_1(s)} \right) p(s) ds, \quad (194)$$

where the threshold now becomes a function of the received power s . The P_{fa} also becomes a function of s given by

$$P_{fa} = \frac{1}{2} \int_0^\infty \operatorname{erfc} \left(\frac{i_T(s)}{\sqrt{2}\sigma_{elec}} \right) p(s) ds. \quad (195)$$

In a *real* system, an estimator needs to be implemented to determine what threshold \hat{i}_T is used for the next particular time slice. The performance of this estimator is driven by the measurement noise and the estimator’s sampling frequency. Since the mean and variance of the transmission of a ‘0’ are relatively constant (for a fixed temperature), Eq. (193) becomes a function of the mean and variance of the signal level of a ‘1’. Because the variance σ_1^2 is signal-dependent and the signal variation is slow compared to the data rate, the variation in the adaptive threshold is only a function of the signal level for the transmission of a ‘1’. In addition, since the transmission of a ‘1’ or ‘0’ is equally likely, the mean signal level for the transmission of a ‘1’ can be determined by $\mu_1 \approx 2\mu_{rcvd} - \mu_0$, if averaged over a short period of time with respect to the turbulence (i.e. $\tau \leq \tau_{irr}$). Therefore, the estimated optimal adaptive threshold can be deduced in a simulation by using the estimate of the current signal level \hat{i}_s and the estimated measurement noises σ_{elec}^2 and $\hat{\sigma}_1^2$.

In this work, the received power is split into two branches with 99 % of the power used in the digital Rx and 1 % used in the estimator. The estimator measures the current in the previous time slice (i_{E_m-}) and the differential signal in the previous

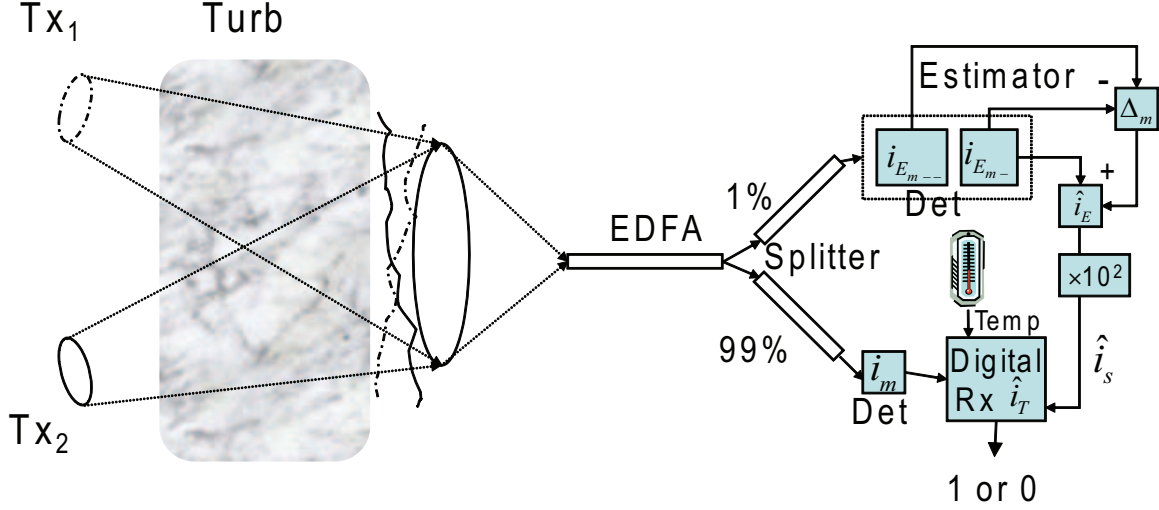


Figure 28: Adaptive threshold estimator.

two measurements ($i_{E_{m--}}$) to determine the estimated signal level. The differential of the measured signal $\Delta_m = (i_{E_{m-}}) - (i_{E_{m--}})$ determines the trend in the previous two estimator measurements $i_{E_{m-}}$ and $i_{E_{m--}}$, respectively, to further refine the estimate. Figure 28 illustrates how it operates. In these simulations the temperature and bandwidth are constant, so σ_{elec}^2 remains constant. The estimated current \hat{i}_s is determined by

$$\hat{i}_s = 100[i_{E-} + n(i_{E-}) + \Delta_m] \quad (196)$$

$$= 100[i_{E_{m-}} + \Delta_m], \quad (197)$$

where the noise in the measurement $n(i_{E-})$ is a zero-mean Gaussian random variable with a variance equal to

$$\sigma_1^2 = \sigma_{elec}^2 + \sigma_{shot}^2 + \sigma_{ASE}^2. \quad (198)$$

The estimator bandwidth and the signal level drive these noise sources in Eq. (198), but since the estimator bandwidth need only be in the kHz range to keep up with the turbulence, the noise power is relatively low. Reducing bandwidth of the estimator further increases the latency of the estimator and degrades the performance of the estimator. If μ_1 in Eq. (193) is set to equal the estimated signal \hat{i}_s and $\mu_0 \approx 0$, the

equation becomes

$$\hat{i}_T = \frac{\hat{i}_s \sigma_{elec}^2}{\sigma_{elec}^2 - \hat{\sigma}_1^2} + \frac{\sigma_{elec} \hat{\sigma}_1}{\hat{\sigma}_1^2 - \sigma_{elec}^2} \sqrt{\hat{i}_s^2 + 2(\hat{\sigma}_1^2 - \sigma_{elec}^2) \ln \left(\frac{\hat{\sigma}_1}{\sigma_{elec}} \right)}, \quad (199)$$

where $\hat{\sigma}_1$ is the estimate of σ_1 using \hat{i}_s .

5.3 Simulation set-up

5.3.1 Modeling the turbulence. The turbulence effects explored subsequently in simulated scenarios were generated using 10 Fourier-series-based random phase screens with the correct statistics placed along the path [48, 83]. The layered analytic spherical coherence diameter $r_{0_{sp}}$, spherical Rytov number \mathcal{R}_{sp} , and isoplanatic angle θ_0 matched within 1% of the full path continuous atmospheric turbulence parameters.

The simulations propagate a collimated Gaussian beam with a $1/e$ field radius of $W_0 = 2.5$ cm using a split-step Fresnel propagation to a 20 cm diameter receiver aperture. Great care was taken to adequately sample the Fresnel propagation between the screens to avoid aliasing in the beam as well as the quadratic phase term [17]. See Section 4.2.1 for the constraints.

5.3.2 Temporally modeling tracker jitter. A coarse tracking system was simulated for the transmitter and receiver for the five air-to-air paths detailed in Table 4 by implementing an ideal centroid tracker and adding random tracking system errors. The errors in the Tx tracker are driven by tilt isoplanatism σ_{TA}^2 due to the point-ahead angle, temporal errors σ_{TT}^2 in the controller, measurement error σ_{TM}^2 , and platform jitter σ_{PJ}^2 . Therefore, the total transmitter tracker error is [31]

$$\sigma_j^2 = \sigma_{TA}^2 + \sigma_{TT}^2 + \sigma_{TM}^2 + \sigma_{PJ}^2. \quad (200)$$

The tilt anisoplanatic error is driven by how close the beams' separation angle is to the tilt isoplanatic angle. The receiver tracker error includes the last three terms of Eq. (200).

The simulated proportional-integral (PI) tracker controller attains temporally correlated jitter rather than using random draws to simulate tracker jitter. The tilt corrector simulates the tracker by centering the centroid of the irradiance at the pupil plane. In order to emulate the Tx and Rx trackers, temporal errors are incorporated in the tilt correctors by adjusting the loop gain of the feedback controller. The simulated different residual beam wander σ_{bw} and beam angle-of-arrival (AOA) jitter σ_{AOA} are multiples of the entire beam wander σ_X for the Tx and AOA jitter σ_T for the Rx, respectively. These runs included an ideal Tx tracker to control the beam wander (i.e. each centroid is shifted to the center of the aperture) such that $\sigma_{bw} = 0$ and non-ideal controllers with residual beam wanders of $\sigma_{bw} = 0.25\sigma_X$, $\sigma_{bw} = 0.75\sigma_X$, and $\sigma_{bw} = \sigma_X$. Likewise, the Rx tracker included an ideal tracker to track the tilt at the aperture and the resulting focal spot jitter, as well as non-ideal Rx trackers with residual tilt jitters of $\sigma_{AOA} = 0.25\sigma_T$, $\sigma_{AOA} = 0.75\sigma_T$, $\sigma_{AOA} = \sigma_T$. For the worst cases of $\sigma_{bw} = \sigma_X$ and $\sigma_{AOA} = \sigma_T$, the Tx beam was pointed on-axis to the Rx and the beams were allowed to wander due to turbulence without a tracking system. The one-axis beam wander variance for a collimated beam is [69]

$$\sigma_X^2 = \frac{6.08}{D^{1/3}} \left(L^2 \int_0^L C_n^2(z) dz - 2L \int_0^L z C_n^2(z) dz + \int_0^L z^2 C_n^2(z) dz \right) \quad (201)$$

in meters squared. The Rx AOA variance T_t^2 in radians squared is given by Eq. (47) in Section 2 [69].

5.3.3 Modeling fiber coupling. At the Rx, the light is coupled into a single-mode fiber to be amplified by an EDFA. There are two primary considerations when coupling into a fiber; the angle at which the light enters the fiber core and the size of the source at the fiber end face. The coupling efficiency due to ray angle is unity for light that enters a fiber at less than the fiber's numerical aperture angle

$\theta_{NA} = \arcsin(NA)$. For single-mode fibers, the efficiency is also limited by an approximately Gaussian field mode guided through the fiber. This field can be described by [11]

$$E_{LP_{01}} = E_0 J_0 \left(\frac{ur}{a} \right) \quad \text{for } r < a \quad (202)$$

$$= E_0 \frac{J_0(u)}{K_0(w)} K_0 \left(\frac{wr}{a} \right) \quad \text{for } r > a, \quad (203)$$

where $u = 1.55$, $w = 1.1428V - 0.996$, and $V = 2.405$ is the normalized frequency parameter of a single mode fiber. This parameter is known as the V number and is given by

$$V = 2\pi a NA / \lambda. \quad (204)$$

In Eqs. (202) and (203), the Bessel function of the first kind is denoted by J_0 , and K_0 is the modified Bessel function of the second kind. Using Eq. (203) determines the irradiance profile in the fiber and enables the program to sum up the optical power coupled in the fiber. To do so, the field at the image plane is written as a linear combination of basis functions

$$E(x, y) = \sum_{i=1}^N a_i f_i(x, y), \quad (205)$$

including the field that couples into the fiber

$$f_1(x, y) = E_{LP_{01}}(x, y) \quad (206)$$

and the field that fails to couple into the fiber

$$f_2(x, y) = 1 - E_{LP_{01}}(x, y). \quad (207)$$

Specifically, the coupled field can be determined by evaluating

$$E_{coupled} = a_1 f_1(x, y), \quad (208)$$

where

$$a_1 = \frac{\iint E(x, y) f_1(x, y) dx dy}{\iint f_1(x, y) dx dy}. \quad (209)$$

Entering the fiber at the numerical aperture angle θ_{NA} yields the optimal coupling efficiency since it provides the smallest spot and enters the fiber end face within θ_{NA} . Therefore, the optimal focal length f of a lens of diameter D to couple a uniform planar field into a fiber is

$$f = \frac{D/2}{\tan(\theta_{NA})}. \quad (210)$$

As the AOA variance increases, the optimal focal length shifts to slightly longer focal lengths. A trade-off could be made, since increasing the focal length also increases the spot size. Although in this research, Eq. (210) determines the focal length of the Rx telescope.

5.4 Temporal results

Computer simulations of airborne single-Tx and double-Tx FSOC systems were performed for the scenarios described in Table 4. The separation distance for all five scenarios for the double-Tx system was $2\rho_c = 31$ cm. Section 5.4.1 describes the resulting temporal fade statistics of the detected signal. Section 5.4.2 plots the BER for all five scenarios and for different techniques used to improve their performance.

5.4.1 Fade statistics. First, a fade definition is required to determine the fade statistics. In Fig. 29, the plot shows the optimal fixed threshold, measured signal (which includes the variation due to the turbulence), and the noise σ_1 associated with the measurement of a ‘1’. Notice how the measured signal near the threshold crosses the threshold often due to the measurement noise σ_1 . Instead of counting each one of those crossings as a fade, a fade occurs only if the variation due to the turbulence in the channel causes it to cross the threshold. In this plot, according to the definition above, there are two distinct fades centered at about 3.9 and 4.05 ms as the dashed

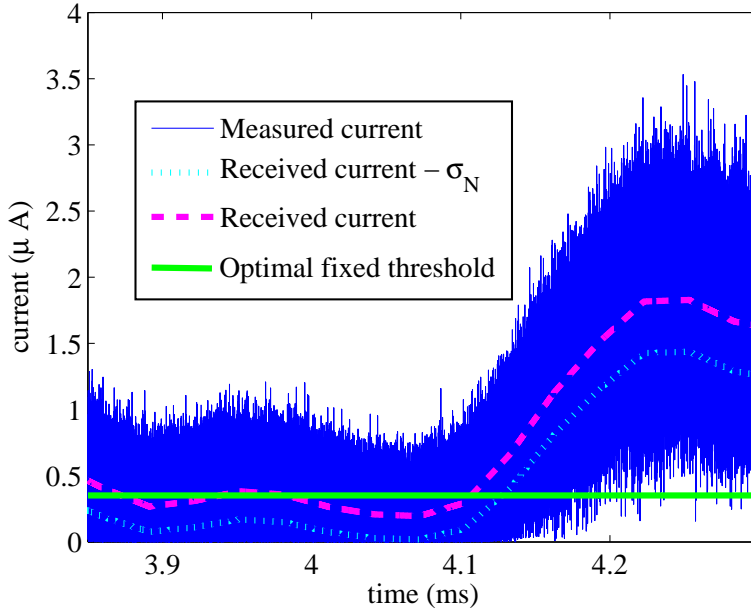


Figure 29: Scenario 5 (HHL). Measured current (solid dark line), received current (dashed line), optimal fixed threshold (solid light line), and received current reduced by the standard deviation of the measurement noise $\sigma_N = \sigma_1$ (dotted line).

line i_s drops below the wide solid line i_T . It is also clear to see in this plot how as the received signal increases, the signal-dependent measurement noise σ_1 increases.

Scenarios 1 and 3 did not experience any fades for the double-Tx cases according to the definition given above so the fades are not plotted. However, these scenarios did experience bit errors and their performance are shown in Section 5.4.2. For the other three scenarios, Figs. 30, 31, and 32 show the double-Tx cases, denoted with dashed line have shorter and less frequent fades than the single-Tx cases denoted by solid line. This is due to the fact that the fade depths are reduced when the multiple Tx's “smooth out” the variation in the received power. As for the tracking systems, the better the tracker the shorter the fades, but the greater the number of fades per second. The tracking systems have essentially the same effect as just turning up the power. Each of the scenarios included an ideal centroid tracker ($\sigma_j = 0$) denoted by a plain line, a tracker with a jitter of $\sigma_j = \sigma_T/4$ denoted by a diamond symbol, and a tracker with a jitter of $\sigma_j = 3\sigma_T/4$ denoted by an asterisk. Figures 30 and

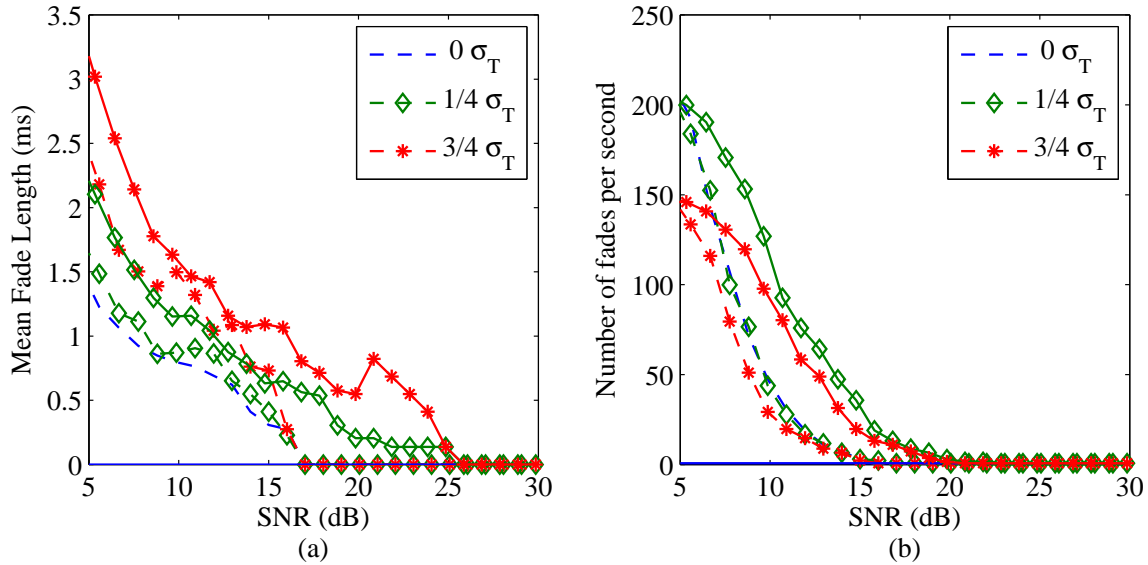


Figure 30: Scenario 2 (HLL). The mean fade length (a) and number of fades per second (b) are plotted vs. SNR. The solid lines are for a single-Tx and the dashed lines are for a double-Tx. A fade is defined here as when the raw received signal s drops below the optimal fixed threshold i_T . The data rate was $R_B = B = 8$ GHz.

32 show results for the most severe turbulence cases and consequently they have the longest and highest number of fades. The only difference between these two cases is the Greenwood frequency of the turbulence. For the low frequency case in Fig. 30, the fade length is about 4.4 times as long, but there are 4.0 times fewer fades than in the high- f_G case in Fig. 32.

5.4.2 Bit error rate. First, the discretized PDFs of the raw received signal $p(i_s)$, i.e. the variations caused by atmospheric turbulence, for each of the scenarios mentioned in Table 4 for the single transmitter cases are compared with their double transmitter cases for all five scenarios. If the PDF is heavily weighted to the left, the chances of a missed detection are greater, as it might not reach above the threshold. Figure 33 shows that the PDFs of the received signal for all of the scenarios shifted to the right when two transmitters were used. Even for the low- \mathcal{R}_{sp} cases, the PDFs markedly shifted to the right to improve the performance. This shift to the right reduces the probability of error since it reduces the probability of a missed detection.

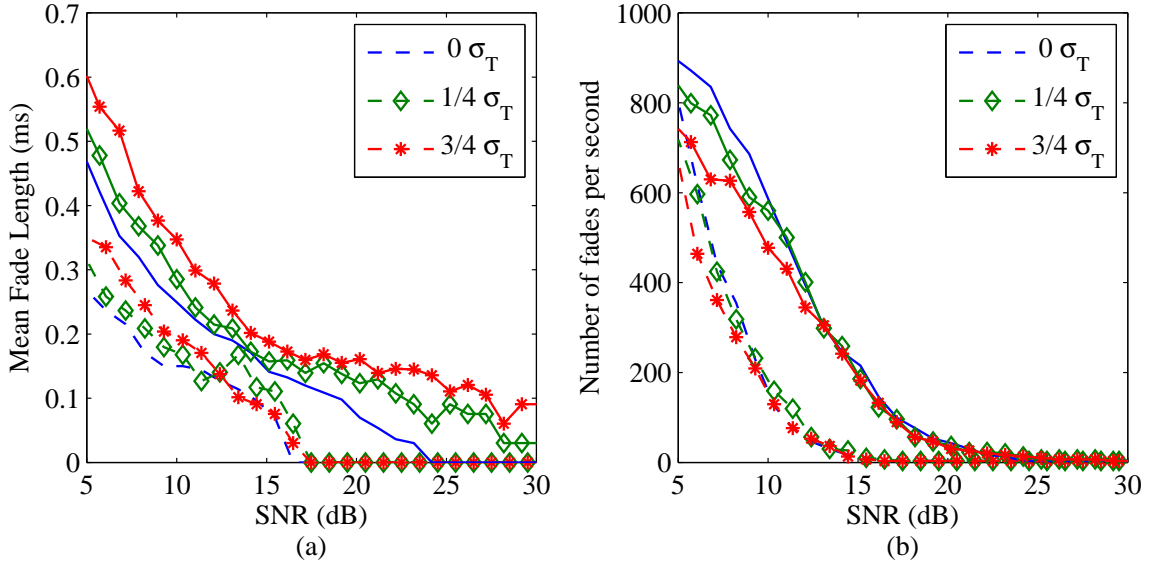


Figure 31: Scenario 4 (HHH). The mean fade length (a) and number of fades per second (b) are plotted vs. SNR. The solid lines are for a single-Tx and the dashed lines are for a double-Tx. A fade is defined here as when the raw received signal s drops below the optimal fixed threshold i_T . The data rate was $R_B = B = 8$ GHz.

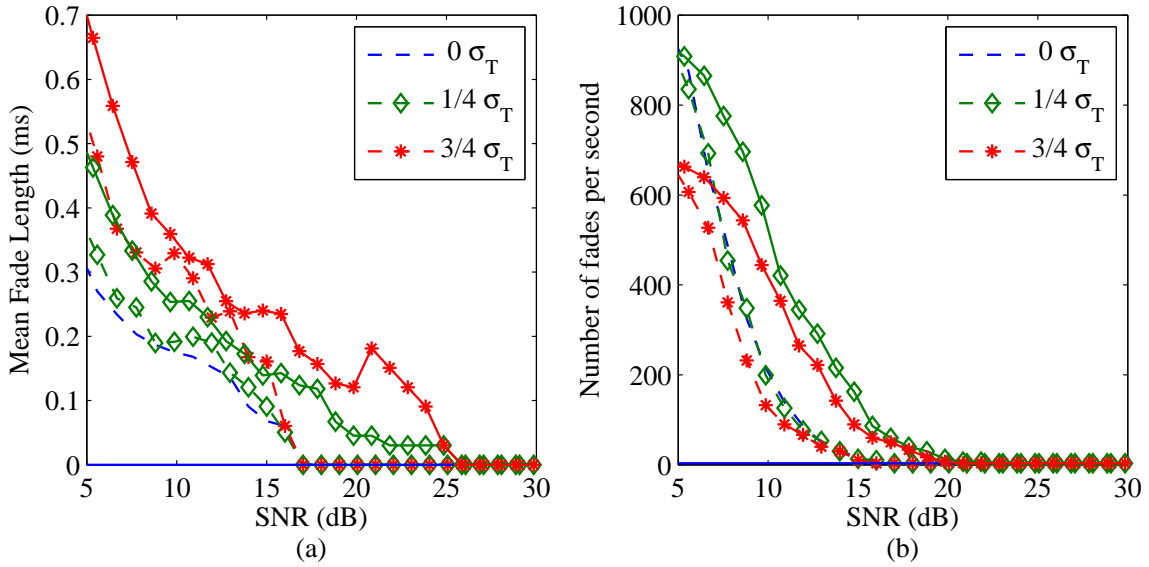


Figure 32: Scenario 5 (HHL). The mean fade length (a) and number of fades per second (b) are plotted vs. SNR. The solid lines are for a single-Tx and the dashed lines are for a double-Tx. A fade is defined here as when the raw received signal s drops below the optimal fixed threshold i_T . The data rate was $R_B = B = 8$ GHz.

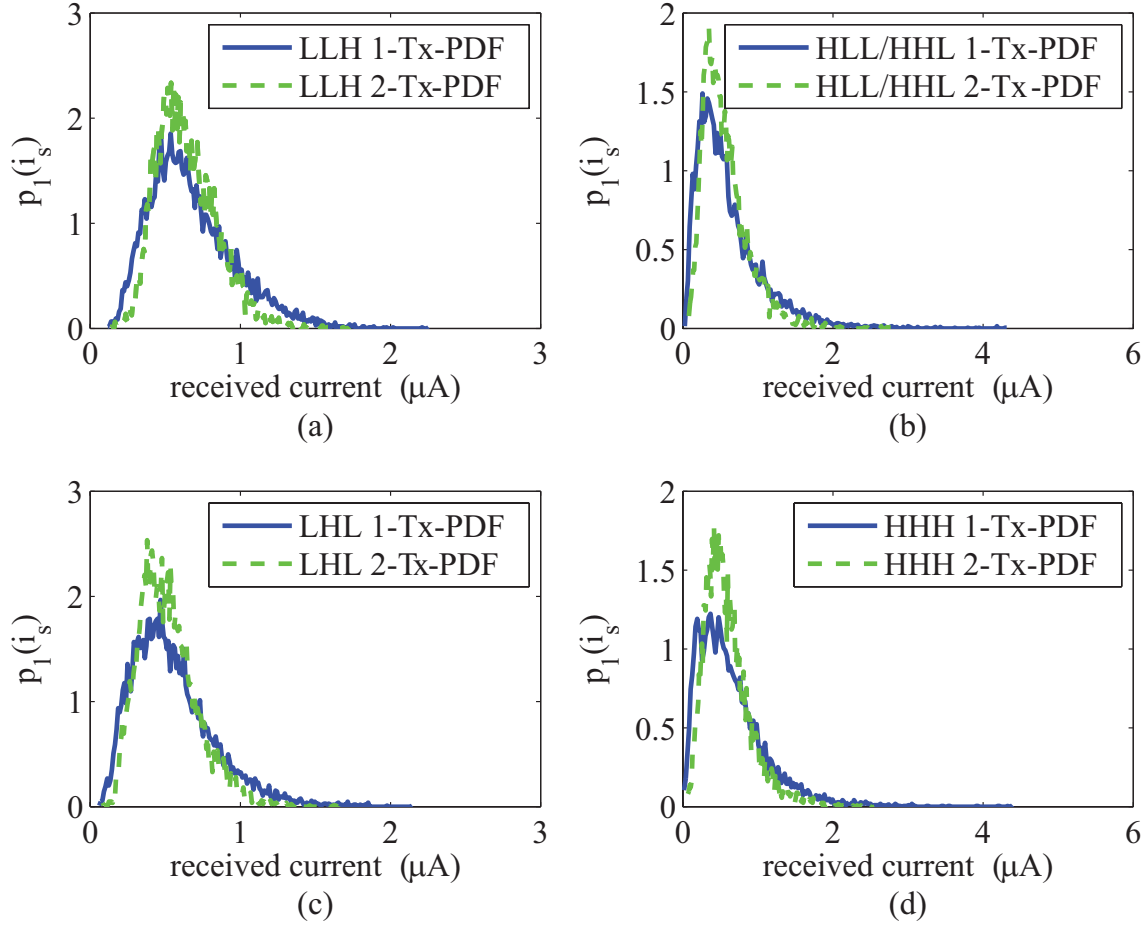


Figure 33: This plot shows the discretized PDFs of the received signals due to turbulence $p(i_s)$ for each of the scenarios for the single-Tx (solid line) and double-Tx (dashed line) cases. Subplots (a)-(d) were calculated for scenarios 1, 2 & 5, 3, and 4, respectively.

It also shifts the optimal threshold to the right, reducing the probability of a missed detection. These performance improvements are quantified with the BER calculations in the next section.

Next, the BERs of ideal and realistic adaptive thresholds are compared to the optimal fixed case. Recall this optimal fixed case takes into account the PDF of the received signal $p(i_s)$ over the ensemble of the runs calculated (see Eq. (188)). There were 10 independent realizations with 1000 time slices for each realization. The time slices were determined by $\tau_s = 1/(64f_G)$ for each of the scenarios. Therefore, each

independent realization covered a time frame of over 15 Greenwood time constants, resulting in well over 150 relatively independent realizations per scenario.

It is clear from Fig. 34 that the BER significantly decreases when two transmitters are used (3-10 dB depending upon the scenario). The ideal adaptive threshold systems improved performance by up to 5 dB for the high-Rytov cases in plots (c) and (d). This is substantial since this was compared to the *optimal* fixed threshold case for the particular scenario which used the actual PDF of the received signal to determine the optimal threshold. In most cases, the fixed threshold is not chosen in such a precise manner. The double-Tx systems outperformed all other techniques even though improvements due to the adaptive-threshold technique were up to 5 dB. As expected, the system with a Rx and Tx tracker, an ideal adaptive threshold, and two transmitters performed the best.

The realistic estimators simulated in this study proved to improve the performance in all cases. The performance of three different adaptive threshold systems are compared in Fig. 34; an ideal adaptive threshold, an adaptive threshold with an estimator operating at $f_s = 64f_G$, and another system with an estimator operating at $f_s = 16f_G$. For a single transmitter the performance for the $f_s = 16f_G$ estimator was the poorest for the highest-Rytov case in scenario 4 HHH. For this and all other cases, this lower sampling rate estimator performance greatly improved when two transmitters were implemented. The single transmitter cases have more variability in the received irradiance and require a higher fidelity estimator to keep up with the turbulence. This trickle-down effect indicates multiple transmitters can enable the use of cheaper lower-sampling-rate estimators.

Finally, the turbulence effects for each of the scenarios are compared with the BER rate performance to determine causality. The only difference between scenarios 2 (HLL) and 5 (HHL) is the speed of the turbulence and therefore, as expected, their BERs are identical. The three scenarios with high Rytov numbers (scenarios 2, 4, and 5) have the worst performance, but the improvement provided by multiple trans-

mitters is much greater for these scenarios. The combination of all three approaches provided at least a 10 dB gain over implementing none of them for all three high Rytov number scenarios. Scenario 5 with a Rytov number $\mathcal{R}_{sp} = 0.20$ enjoyed a 13 dB overall improvement. Due to the improvements afforded by these multiple techniques, the high Rytov cases of $\mathcal{R}_{sp} \approx 0.20$ were on par with Rytov numbers of $\mathcal{R}_{sp} \approx 0.060$ without these techniques. All five scenarios tested $0.060 < \mathcal{R}_{sph} < 0.20$ were within 3 dB of each other when all of the improvement techniques were implemented. In all scenarios, the coherence diameter r_0 was greater than the diameter of the receiver D , therefore changes in the Rytov number had a much larger effect than r_0 . If $D/r_0 > 1$ the phase effects due to the turbulence would likely have had a larger effect on the BER.

Adaptive thresholding systems provide significant improvement over optimal fixed thresholds for both single-Tx and double-Tx systems, providing an additional 3-4 dB over both systems. As long as the estimator kept up with the turbulence the realistic estimators performed well. As the scintillation effects were stronger for the single-Tx high Rytov scenario (HHH), the lower bandwidth estimator performance lagged behind the high resolution estimator and the ideal adaptive threshold system. The primary driver to the adaptive threshold system seemed to be the bandwidth, not the noisy measurements. This is most likely due to the fact that the SNR in the estimator was much higher than for the digital receiver leg (see Fig. 28, since the required bandwidth was so much lower (kHz vs. GHz).

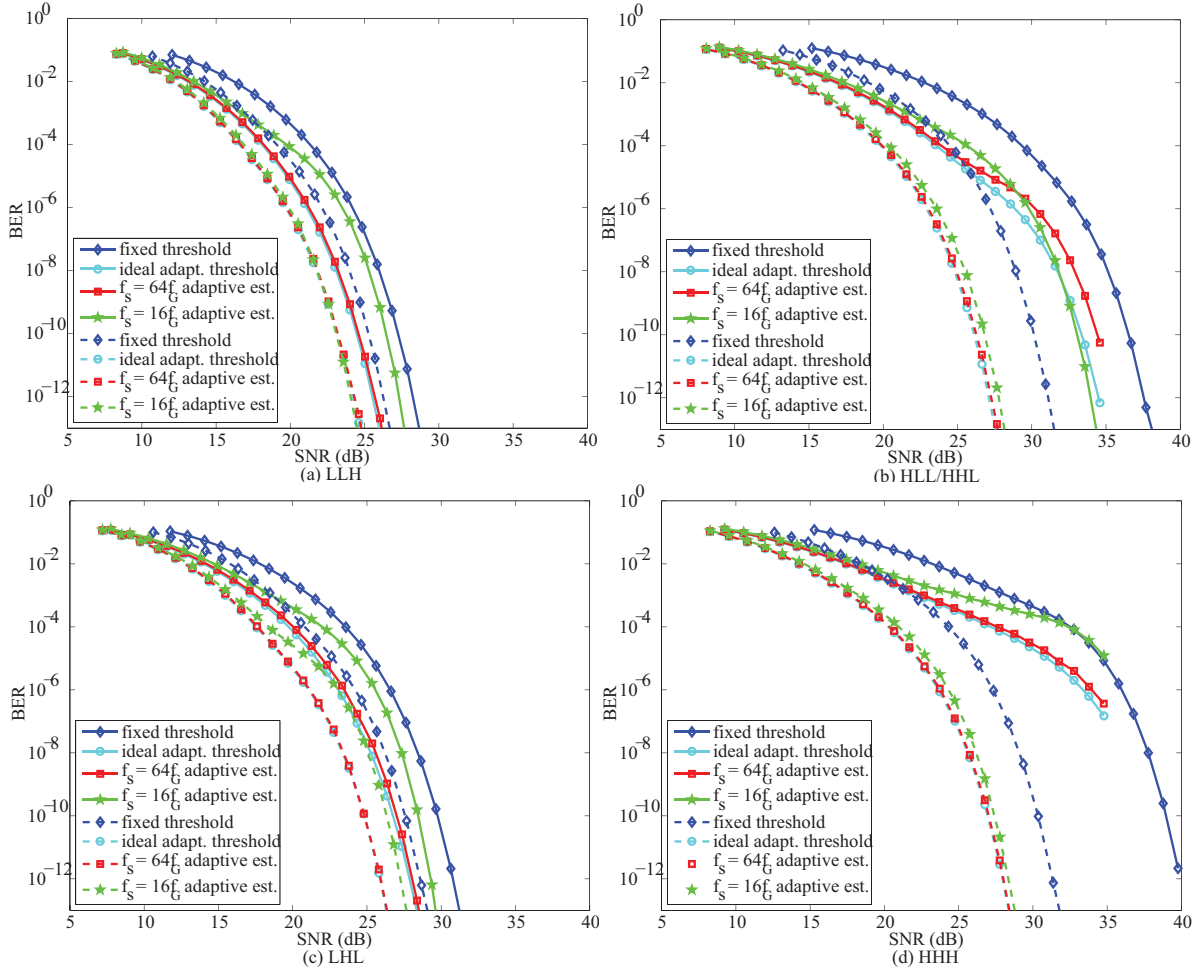


Figure 34: BER for systems with an optimal fixed threshold, ideal adaptive threshold, $f_s = 64f_G$ estimator adaptive threshold, and $f_s = 16f_G$ estimator adaptive threshold for single Tx (solid lines) and double Tx (dashed lines) for the tracker case of $\sigma_j = \sigma_T/4$. Subplots (a)-(d) were calculated for scenarios 1, 2 & 5, 3, and 4, respectively. The data rate was $R_B = B = 1$ GHz.

VI. Conclusion

This chapter discusses the final conclusions of this research including the challenges that were overcome to complete the project, the key results, first-time derivations, and recommendations for future work.

6.1 *Challenges met*

The first challenge met as with any research endeavor dealt with defining the problem and scoping the effort to a reasonable size to accomplish the research in the afforded time. There has been quite a bit of research into free-space optical communication in recent years. Fortunately, FSOC still offers many different fertile areas for research, especially for the air-to-air link. The idea for using multiple transmitters came from the realization that extended objects in the far field (like the moon and the planets) do not twinkle like the stars. The fluctuations for these extended objects still occur, but they are averaged over the extent of the object. Multiple laser transmitters incoherent with each other and adequately separated act in much the same way.

Secondly, for all the literature on multiple Tx-Rx systems, there was little information about how far apart to have the Tx's to accomplish good averaging. For the multiple-Tx case, the next challenge was to determine analytic equations for the requisite anisoplanatic separations for the phase and amplitude perturbations. This analytic research built on developments from Roggemann and Welsh, [66] Sasiela, [69] Andrews and Phillips, [2] and Fried [26] to determine the anisoplanatic effects in turbulence. Many tacks were taken to determine these relations, starting with a study of the differential tilt variance relations in Sasiela to determine the tilt anisoplanatic angle. Determining the separation required for the tilt anisoplanatic angle proved to be intractable. A new tack was used to determine tilt anisoplanatic angle by way of the phase anisoplanatic angle. This approach started with the phase isoplanatic effects and determined for the first time a relation for the phase anisoplanatic angle. As for the amplitude effects, using the principle of reciprocity, the requisite Tx separation was determined by using the correlation width ρ_{cw} previously used to predict how Rx

size effects scintillation. Similarly, this ρ_{cw} relation can be determined by referring to the log-amplitude structure function. The problem with the amplitude effects is that they saturate for strong turbulence, making these relations only valid for the weak turbulence regime and increasing the importance of simulation and experimentation.

The third challenge was to determine the practical feasibility of a multiple transmitter approach for the airborne scenario. Since these analytic relations had not been studied for the airborne scenario, they needed to be tested to determine which geometries might be feasible. Scenarios for the air-to-air, ground-to-air, ground-to-ground, and air-to-ground were tested in random independent realizations of turbulence. The Rx model included a tracking system for both the Rx and the Tx as well as modeling the coupling into a single mode fiber.

The fourth challenge was to design a method to simulate these multiple scenarios. A wave-optics simulation for each of the scenarios was developed from scratch, with each requiring special considerations for sampling. These considerations were dealt with by implementing a split-step Fresnel propagation system to reduce the sampling requirements. The long propagations using the split-step Fresnel method still require large arrays to satisfy the sampling constraints in Eqs. (163) to (166). In this research 2048×2048 arrays were used to calculate the propagations through 10 independent phase screens for the propagations in Chapter V. Special coding considerations were used to properly handle these large arrays to avoid “out of memory” conditions. The analysis that followed determined that an air-to-air multiple Tx system was feasible since the optimal separation was only about 31cm apart for the 100 km long, 10 km altitude path.

Next, implementing the time-series wave-optics simulation presented new challenges in modeling. A new relation for determining the temporal sampling of a wave-optics simulation was developed that takes into account the temporal aspects of the amplitude perturbations. The Fourier-series-based phase screens enabled the calculation of time-correlated phase screens without requiring the screens to be repeated.

Finally, the fixed optimal threshold required knowledge of turbulence PDF, but determining the PDF of these multiple turbulence scenarios with multiple Tx's was intractable. Therefore, numerical PDFs were determined from the simulations and used to determine the fixed optimal threshold. The ideal adaptive threshold system used in other research [13,18,72] was compared to a new linear estimator designed for this research. For all calculations the measurement noise sources included, thermal, shot, and ASE noise from the EDFA.

6.2 *Key results*

6.2.1 Anisoplanatic effects. This research designed a multiple-transmitter system to average different effects of turbulence by first determining the requisite separation distances. Roggemann, Fried, Saseila and others determined isoplanatic conditions so that the effects of two paths were relatively correlated [26,51,66,69,70,84]. This separation allows AO systems to measure and correct for these effects in real time. Here, the research of Roggemann, Welsh, and Fried was extended to determine when these effects become uncorrelated [26,66]. The phase anisoplanatic angle $\theta_{\psi_{ind}}$ was first derived in support of this research [46,47,49] and defines the angle over which the phase effects between the propagation paths of two point sources are nearly uncorrelated. This relation increases with outer scale and turbulence strength and defines the separation where the beams wander nearly independently. This angle describes the minimum separation for uncorrelated beam wandering which determines the optimal separation distance for untracked multiple Tx systems. The likely application for an untracked system is a ground-to-ground last-mile communication system, since the system is stationary and the outer scale is small, allowing for reasonable separation distances (i.e. 25-100 cm). As long as there are sufficient number of Tx's with wide enough beams, a system could be designed to maintain at least one beam on the target without the need for tracking. This phase anisoplanatic angle also corresponds to the tilt anisoplanatic angle, since the lowest-order phase effects manifest themselves as tilt and beam wander.

Since this research is concerned with air-to-air laser communication a separation distance is required for a tracked system. In this case, a separation angle is required to average the higher-order phase and/or scintillation effects. The beams must be separated far enough apart that the scintillation effects are uncorrelated. This occurs when the variance of the difference between the two effects is equal to twice the variance of a single path effect. In previous research [2], this condition was determined as the correlation width ρ_{cw} for amplitude variations of two paths. This previous work applied to how large a receiver aperture needs to be averaging out scintillation effects. Here, the principle of reciprocity determines how far apart the *transmitters* need to be so the scintillation effects can be averaged at the receiver. At this separation, the hot spots and signal drop outs due to strong scintillation across the aperture are “averaged out.” Research has been done to determine this requisite separation distance [4, 5, 59, 60], but it has not been accomplished for air-to-air scenarios and not put in terms of the correlation width ρ_{cw} . The optimal Tx separation distance for reducing BER was 1-3 times ρ_c for the air-to-air and ground-to-air scenarios.

The improvement due to implementing two transmitters can be scaled to a small degree for multiple transmitters. A limit to this improvement does exist, since separating beams much greater than $2\rho_c$ results in diminishing improvement as shown in Chapter IV [46, 49]. The mechanism for declining performance improvement depends upon how the beams are separated. If the beams are separated in angle, the average AOA of the beams at the receiver causes the beams to land off-center of the detector. If the beams are too far apart angularly, the beams on average will land off of the detector in the focal plane, consequently reducing the power at the detector. If the beams are parallel, separating them further causes each beam to land further off axis at the aperture, reducing the individual beam’s received power and increasing the scintillation.

Since scintillation effects begin to decorrelate for fairly small separations, the transmitters only need to be separated by approximately $2\rho_c$ for air-to-air scenarios of 100 km in length at 4km in altitude and above.

Conventional AO systems only correct for phase and cannot correct for strong scintillation, but here the different transmitters “average out” the strong scintillation effects by incoherently summing up the two beams in the receiver. Additionally, since the Rx aperture diameter was smaller than r_0 , an AO system would not have provided much improvement.

6.2.2 Temporal aspects and fade statistics. Research by Haas, Anguita, Lee, Peleg, and others into multiple transmitters have not considered the temporal impacts of multiple transmitters [4, 5, 29, 30, 43, 59]. This research determined that the multiple transmitter approach not only reduces the length of fades, but also reduces the number of fades by simultaneously reducing the variation and increasing the received power. The averaging effect of two transmitters reduced the BER and the length of faded. This effect had not been studied before. If further error reduction is required, an interleaver/FEC receiver could be implemented. Multiple Tx techniques and adaptive thresholding do not require physical elements to adaptively compensate for turbulence, but they reduce fade lengths. This temporal aspect of multiple-Tx systems had not been studied before. In addition, the length of fades for higher air velocities are shorter than the lower air velocities. Shorter fade lengths require shorter interleavers, reducing data latency and making shorter interleavers more effective.

6.2.3 Optimal fixed and adaptive thresholding. Burriss used estimates of signal mean and variance to determine the optimal fixed threshold using the LRT [13]. Crabtree calculated the optimal fixed threshold using turbulence PDF estimates, which is better since it takes into account an estimate of the turbulence PDF’s shape [18]. This research and Schmidt’s research used the actual discretized PDFs from the simulations [72]. The ideal adaptive threshold system in other research [13, 18] was compared to a new linear estimator designed for this research. All previous cases of adaptive thresholding systems were implemented for the single-Tx case. For high-Rytov scenarios, the low-sampling-rate estimator performance greatly improved when two transmitters were implemented. The single transmitter cases have

more variability in the received irradiance and require a higher fidelity estimator to keep up with the turbulence. This trickle-down effect indicates multiple-Tx systems enable the use of cheaper lower-sampling-rate estimators.

These and other trickle-down effects, like the reduction in fade lengths for multiple transmitter systems indicate the techniques implemented in this research were complimentary. In addition, the performance improvements for these techniques were additive and pushed the performance of high-Rytov ($\mathcal{R}_{sp} \approx 0.20$) turbulence cases to the performance of much more benign turbulence regimes ($\mathcal{R}_{sp} \approx 0.06$).

This research enables free-space optical communication systems, promising to provide covert, difficult to jam or intercept, high-speed, broadband connectivity to airborne platforms [86]. This connectivity will provide unparalleled situational awareness to the warfighter. The next steps in this research include designing hardware to implement this system in a hardware in the loop test followed by flight testing.

6.3 Recommendations for future work

Throughout this research effort multiple areas for future research were identified. These areas are summarized below.

6.3.1 Diversity techniques. To illustrate the optimal separation only two beams were used, so the full impact of this approach has yet to be explored. Others have shown that four beams, for instance, can be very effective in a ground-to-ground link scenario [5]. Multiple-transmitter configurations could be studied to determine the point of diminishing return and what configuration is optimal for both parallel and angular separations. Since the improvements for two Tx's peaked for separations of about 2-3 ρ_c and diminishing returns occurred for separations larger than about 3 ρ_c , 4-5 transmitters is potentially the limit before improvements diminish, but this needs to be demonstrated conclusively. In addition, a comparison of parallel versus angular separated beams might provide some interesting design considerations.

A combination of multiple transmitters and conventional AO might provide significant improvement without the need for sophisticated multi-conjugate adaptive optics systems. The multiple transmitters would provide the improvement in terms of reducing scintillation while the AO system would handle the phase perturbations, likely improving the fiber coupling. A comparison of conventional AO and multiple transmitter system performance for varying turbulence conditions could also provide some design considerations for future air-to-air FSOC systems.

6.3.2 Optical receiver design. The receiver coupled the laser light into a single mode EDFA. The optimal focal length used in this research was based on a plane wave incident on the aperture. If the AOA variance is large at the Rx, longer focal lengths would be required to maintain an angle less than the NA angle to couple more light into the fiber. A trade-off would have to be made as well since increasing the focal length also increases the spot size. AOA variance due to turbulence and multiple-transmitter systems could provide a rich design space for investigating tradeoffs in the focal length of the receiving telescope.

Fiber amplifiers offer advantages in simplicity, efficiency, and high-speed performance. More detailed fiber amplifier modeling could distinguish other advantages including automatic gain control afforded by the gain saturation. In addition, schemes to improve the coupling efficiency could ameliorate their performance.

The propagation of lasers through extended turbulence causes significant hot spots and dropouts. Therefore, an optical and/or electrical AGC would likely provide significant performance improvement with inherently dynamic-range-limited detectors. EDFAs do afford some optical automatic gain control, but research into other techniques could provide additional improvements.

6.3.3 Signal processing techniques. Adapting the threshold provided significant improvement. This improvement was compared to the optimal fixed threshold case, which is difficult to implement since it requires knowledge of the turbulence

PDF. If comparisons were made with more realistic thresholds, the performance improvement would have been more significant. Comparisons with multiple methods including a threshold determined solely from the average power level over a time period might provide a more realistic improvement metric. In addition, the estimator used in this work could be extended to an optimal estimation of the decision threshold from a noisy measurement.

6.3.4 Tracking systems. A point-ahead angle study for very fast moving transmitters and receivers might lead to a determination that higher-order phase compensation using conventional adaptive optics systems might be difficult at best, unfeasible at worst.

The centroid trackers used in this research performed relatively poorly. This was due to the significant scintillation of the extended turbulence propagation. Techniques to track the multiple hot spots or select the optimal tracking path could improve the performance. (Many times the centroid was located in a low intensity location on the aperture) In addition, new tracking and pointing algorithms could be developed for multiple-transmitter systems, since the separation required to average out the scintillation is smaller than the tilt isoplanatic angle. Scintillation does adversely affect centroid determination in a centroid-tracking system [48].

In this work, each transmitter had its own tracking system. Since the transmitter separation is likely to be within the tilt isoplanatic angle, a single tracker for this configuration might be adequate. Multiple transmitters alone might be able to improve the tracking system since it would reduce the hot spots in the receiver. This reduction in hot spots could enable a better centroid tracking system since it would not jump around due to the scintillation effects.

6.3.5 Large communication system design. On a system-level basis one could study the design consideration of a high-altitude optical communication hub. This hub would provide satellite uplink/downlink to coordinate and route information from the

future Transformational Satellite Communications System (TSAT). An airborne relay mirror system could be considered to provide over-the-horizon high-speed line-of-sight communication for the battle space. It would provide much faster communication than satellite communication systems and would provide a high bandwidth approach to long haul ground-to-ground communication systems.

Bibliography

1. Alexander, S. B. *Optical Communication Receiver Design*. SPIE Tutorial Texts in Optical Engineering, vol. TT22; IEE Telecommunications Series, vol. 37. SPIE Press, Bellingham, WA, 1997.
2. Andrews, L. C. and R. L. Phillips. *Laser Beam Propagation Through Random Media*. SPIE Optical Engineering Press Bellingham, WA, 2005.
3. Andrews, L. C., R. L. Phillips, and C. Y. Hopen. *Laser Beam Scintillation with Applications*. SPIE Press, Bellingham, WA, 2nd edition, 2001.
4. Anguita, J. A., M. A. Neifeld, and B. V. Vasic. “Multi-beam space-time coded systems for optical atmospheric channels”. *Proc. SPIE*, 6304(63041B):1–9, 2006.
5. Anguita, J. A., M. A. Neifeld, and B. V. Vasic. “Spatial correlation and irradiance statistics in a multiple-beam terrestrial free-space optical communication link”. *Appl. Opt.*, 46(21):6561–6571, 2007.
6. Arnon, S. “Use of Satellite Natural Vibrations to Improve Performance of Free-Space Satellite Laser Communication”. *Appl. Opt.*, 37(21):5031–5036, 1998.
7. Belmonte, A. “Influence of atmospheric phase compensation on optical heterodyne power measurements”. *Opt. Express*, 16(9):6756–6767, 2008.
8. Boone, B. G., J. R. Bruzzi, W. P. Millard, K. B. Fielhauer, B. E. Kluga, C. W. Drabenstadt, and R. S. Bokulic. “Optical Communications Development for Spacecraft Applications: Recent Progress at JHU/APL”. *IEEE Aerospace Conference*, 0-7803-8870-4:1–13, 2005.
9. Booth, M. “Wave front sensor-less adaptive optics: a model-based approach using sphere packings”. *Opt. Express*, 14(4):1339–1352, 2006.
10. Britz, D.M., J.P. Dodley, and C.L. Rutledge. “High dynamic range free-space optical communication receiver”, September 19 2000. US Patent 6,122,084.
11. Buck, J.A. *Fundamentals of Optical Fibers*. Wiley-Interscience, 2004.
12. Burris, H.R., N.M. Namazi, A.E. Reed, W.J. Scharpf, C.I. Moore, M.J. Vilcheck, M.A. Davis, M.F. Stell, M.R. Suite, W.S. Rabinovich, and R. Mahon. “Comparison of adaptive methods for optimal thresholding for free-space optical communication receivers with multiplicative noise”. *Proc. SPIE*, 4821:139–154, 2002.
13. Burris, H.R., A.E. Reed, N.M. Namazi, W.J. Scharpf, M.J. Vicheck, M.F. Stell, and M.R. Suite. “Adaptive thresholding for free-space optical communication receivers with multiplicative noise”. *Proc. IEEE Aerospace Conference*, volume 3, 1473–1480. 2002.

14. Burris, H.R., A.E. Reed, N.M. Namazi, M.J. Vilcheck, and M. Ferraro. "Use of Kalman filtering in data detection in optical communication systems with multiplicative noise". *Proc. IEEE International Conference on Acoustics, Speech, and Signal Processing (ICASSP '01)*, volume 4, 2685–2688. 7-11 May 2001.
15. Churnside, J. H. "Aperture averaging of optical scintillations in the turbulent atmosphere". *Appl. Opt.*, 30(15):1982–, 20 May 1991.
16. Churnside, J. H. and R. J. Lataitis. "Wander of an optical beam in the turbulent atmosphere". *Appl. Opt.*, 29(7):926, March 1990 1990.
17. Coy, S. "Choosing Mesh Spacings and Mesh Dimensions for Wave Optics Simulation". *Proc. SPIE*, 5894, 2005.
18. Crabtree, P. N. *Dissertation: Performance-Metric Driven Atmospheric Compensation for Robust Free-Space Laser Communication*. Air Force Institute of Technology, Wright-Patterson AFB, OH, 2006.
19. Dereniak, E.L and G.D. Boreman. *Infrared Detectors and Systems*. John Wiley and Sons, Inc, New York, NY.
20. Duchak, G. "Optical RF Combined Link Experiment Brief". *Defense Advanced Research Project Agency Advance Technology Office*, 19 November 2003.
21. Eaton, F. D. and G. D. Nastrom. "Preliminary estimates of the vertical profiles of inner and outer scales from White Sands Missile Range, NM VHF radar observations". *Radio Sci.*, 33(4):859–903, 1998.
22. Filho, C. JCSS and P. Yacoub. "Simple accurate lognormal approximation to lognormal sums". *Electron. Lett.*, 41(18):1016–1017, 2005.
23. Fried, D. L. "Optical Resolution Through a Randomly Inhomogeneous Medium for Very Long and Very Short Exposures". *J. Opt. Soc. Am. A*, 56(10):1372–1379, 1966.
24. Fried, D. L. "Aperture averaging of scintillation". *J. Opt. Soc. Am. A*, 57(2):169–175, 1967.
25. Fried, D. L. "Spectral and Angular Covariance of Scintillation for Propagation in a Randomly Inhomogeneous Medium". *Appl. Opt.*, 10(4):721–731, 1971.
26. Fried, D. L. "Anisoplanatism in adaptive optics". *J. Opt. Soc. Am. A*, 72(1):52–61, 1982.
27. Goodman, J. W. *Statistical Optics*. John Wiley & Sons, Hoboken, NJ, 1985.
28. Grunet-Jepsen, A., AE Johnson, ES Maniloff, TW Mossberg, MJ Munroe, and JN Sweetser. "Demonstration of all-fiber sparse lightwave CDMA based on temporalphase encoding". *IEEE Photonics Lett.*, 11(10):1283–1285, 1999.
29. Haas, S. M. *Dissertation: Capacity of and Coding for Multiple-Aperture, Wireless, Optical Communications*. Massachusetts Inst. of Technology, 2003.

30. Haas, S. M. and J. H. Shapiro. “Capacity of Wireless Optical Communications”. *IEEE J. Sel. Areas Commun.*, 21(8):1346–1357, 2003.
31. Hardy, J.W. *Adaptive Optics for Astronomical Telescopes*. Oxford University Press, USA, 1998.
32. Hemmati, H. “Status of free-space optical communications program at JPL”. *IEEE Aerospace Conf. Proc.*, volume 3. 2000.
33. Hemmati, H. “Optical systems for free-space laser communications”. *SPIE Proc.*, volume 5173, 64. SPIE, 2003.
34. Higgs, C., H. T. Barclay, and K. W. Billman. “Multibeam laser illuminator approach”. *Proc. SPIE*, 3706:206–215, 1999.
35. Hindman, C. and L. Robertson. “Beaconless satellite laser acquisition-modeling and feasibility”. *IEEE Military Communications Conference*, 0-7803-8847-W:41–47, 2004.
36. Ishimaru, A. *Propagation and Scattering in Random Media*. New York: Academic Press, 1978.
37. Javitt, J.I. and C.L. Rutledge. “Automatic gain control for free-space optical telecommunications links”, February 29 2000. US Patent 6,031,648.
38. Jennewein, T., C. Simon, G. Weihs, H. Weinfurter, and A. Zeilinger. “Quantum Cryptography with Entangled Photons”. *Phys. Rev. Lett.*, 84(20):4729–4732, May 2000.
39. Kiasaleh, K. “Performance analysis of free-space on-off-keying optical communication systems impaired by turbulence”. *SPIE Proc.*, volume 4635, 150. 2002.
40. Kim, I. I., H. Hakakha, P. Adhikari, E. J. Korevaar, and A. K. Majumdar. “Scintillation reduction using multiple transmitters”. *Proc. SPIE*, 2990:102, 1997.
41. Kolmogorov, A. N., S.K. Friedlander, and L. Topper (editors). *Turbulence, Classic Papers on Statistical Theory*. Interscience, New York, NY, 1961.
42. Lange, R., B. Smutny, B. Wandernoth, R. Czichy, and D. Giggenbach. “142 km, 5.625 Gbps free-space optical link based on homodyne BPSK modulation”. *Proc. SPIE*, 6105:61050A, 2006.
43. Lee, E. J. and V. W. S. Chan. “Part 1: Optical Communication Over the Clear Turbulent Atmospheric Channel Using Diversity”. *IEEE J. Sel. Areas Commun.*, 22:1896–1906, 2004.
44. Lee, S., J. W. Alexander, and M. Jeganathan. “Pointing and tracking subsystem design for optical communications link between the International Space Station and ground”. *Proc. SPIE*, 3932:150–157, 2000.
45. Louthain, J. A. *Master’s Thesis: Atmospheric turbulence scintillation effects of wavefront tilt estimation*. Air Force Institute of Technology, 1997.

46. Louthain, J. A. and J. D. Schmidt. “Anisoplanatism in airborne laser communication”. *Opt. Express*, 16(14):10769–10785, 2008.
47. Louthain, J. A. and J. D. Schmidt. “Integrated approach to airborne laser communication”. *Proc. SPIE*, 7108(14), 2008.
48. Louthain, J. A. and B. M. Welsh. “Fourier-series-based phase and amplitude optical field screen generator for weak atmospheric turbulence”. *Proc. SPIE*, 3381:286–296, 1998.
49. Louthain, James A. and Jason D. Schmidt. “Anisoplanatic Approach to Airborne Laser Communication”. *Meeting of the Military Sensing Symposia (MSS) Specialty Group on Active E-O Systems*, I(AD02):1–20, 2007.
50. Magee, E. P. *Phase Screens for Long Time Series Wave Optics Simulations*. Technical Report. Mission Research Corporation, Dayton, OH, 2003.
51. Magee, E. P., M. R. Whiteley, S. T. Das, and B. M. Welsh. “Tilt anisoplanatism in extended turbulence propagation”. *Proc. SPIE*, 4976:13–21, 2003.
52. McManamon, P. F. and W. Thompson. “Phased Array of Phased Arrays (PAPA) Laser Systems Architecture”. *Fiber Integr. Opt.*, 22(2):79–88, 2003.
53. Murray, L.P., J.C. Dainty, J. Coignus, and F. Felberer. “Wavefront-sensorless aberration correction of extended objects using a MEMS deformable mirror”. *Proc. of SPIE*, volume 6113, 61130G–1 – 61130G–8. 2006.
54. Naletto, G., F. Frassetto, N. Codogno, E. Grisan, S. Bonora, V. Da Deppo, and A. Ruggeri. “No wavefront sensor adaptive optics system for compensation of primary aberrations by software analysis of a point source image. 2. Tests”. *Appl. Opt.*, 46(25):6427–6433, 2007.
55. Ohtsuki, Tomoaki. “Turbo-coded atmospheric optical communication systems”. *IEEE International Conference on Communications*, volume 5, 2938–2942. 2002.
56. Osche, G. R. *Optical Detection Theory for Laser Applications*. John Wiley & Sons, Hoboken, NJ, 2002.
57. Papoulis, A. *Probability, Random Variables, and Stochastic Processes*. MacGraw-Hill, New York, 3rd edition, 1991.
58. Parry, G. “Measurements of Atmospheric Turbulence Induced Intensity Fluctuations in a Laser Beam”. *J. Mod. Opt.*, 28:715–728, 1981.
59. Peleg, A. and J. V. Moloney. “Scintillation index for two Gaussian laser beams with different wavelengths in weak atmospheric turbulence”. *J. Opt. Soc. Am. A*, 23(12):3114–3122, 2006.
60. Polynkin, P., A. Peleg, L. Klein, T. Rhoadarmer, and J. Moloney. “Optimized multiemitter beams for free-space optical communications through turbulent atmosphere”. *Opt. Lett.*, 32:885–887, 2007.

61. Poppe, A., A. Fedrizzi, R. Ursin, H. Bhm, T. Lrunser, O. Maurhardt, M. Peev, M. Suda, C. Kurtsiefer, and H. Weinfurter. “Practical quantum key distribution with polarization entangled photons”. *Opt. Express*, 12(16):3865–3871, 2004.
62. Prasad, N.S., P.T. Kratovil, C. Bjork, and N.J. Vallesterio. “Angle discrimination based pointing and tracking for free-space communication links”. *SPIE Proc.*, volume 5550, 20. 2004.
63. Razavi, Mohsen. “Wireless Optical Communications via Diversity Reception and Optical Preamplification”. *IEEE Trans. Wireless Commun.*, 4(3), May 2005.
64. Ricklin, J. C. and F. M. Davidson. “Atmospheric turbulence effects on a partially coherent Gaussian beam: implications for free-space laser communication”. *J. Opt. Soc. Am. A*, 19(9):1794–1802, Sep 2002.
65. Ricklin, J. C. and F. M. Davidson. “Atmospheric optical communication with a Gaussian Schell beam”. *J. Opt. Soc. Am. A*, 20(5):856–866, May 2003.
66. Roggemann, M. C. and B. M. Welsh. *Imaging Through Turbulence*. CRC Press, 1996.
67. Roggemann, M. C., B. M. Welsh, D. A. Montera, and T. Rhoadarmer. “Method for simulating atmospheric turbulence phase effects for multiple time slices and anisoplanatic conditions”. *Appl. Opt.*, 34:4037–4051, 1995.
68. Ryan, P. T., W. H. Lowrey, I. A. De La Ru, and R. Q. Fugate. “Scintillation characterization for multiple beams”. *Proc. SPIE*, 3763:210–217, 1999.
69. Sasiela, R. J. *Electromagnetic wave propagation in turbulence. Evaluation and application of Mellin transforms, 2nd Ed.* SPIE Publications, 2007.
70. Sasiela, R. J. and J. D. Shelton. “Transverse spectral filtering and Mellin transform techniques applied to the effect of outer scale on tilt and tilt anisoplanatism”. *J. Opt. Soc. Am. A*, 10:646660, 1993.
71. Schawlow, AL and CH Townes. “Infrared and Optical Masers”. *Phys. Rev.*, 112(6):1940–1949, 1958.
72. Schmidt, J. D. *Dissertation: Free-Space Optical Communications Performance Enhancement by Use of a Single Adaptive Optics Correcting Element*. University of Dayton, Dayton, OH, 2006.
73. Schmitt-Manderbach, T., H. Weier, M. Fürst, R. Ursin, F. Tiefenbacher, T. Scheidl, J. Perdigues, Z. Sodnik, C. Kurtsiefer, J.G. Rarity, et al. “Experimental Demonstration of Free-Space Decoy-State Quantum Key Distribution over 144 km”. *Phys. Rev. Lett.*, 98(1):10504, 2007.
74. Sklar, B. *Digital Communications Fundamentals and Applications*. Prentice-Hall, Inc., 2nd edition, 2001.

75. Toyoshima, M., T. Jono, K. Nakagawa, and A. Yamamoto. "Optimum divergence angle of a Gaussian beam wave in the presence of random jitter in free-space laser communication systems". *J. Opt. Soc. Am. A*, 19(3):567–571, Mar 2002.
76. Trisno, S. and C. C. Davis. "Performance of free space optical communication systems using polarization shift keying modulation". A. K. Majumdar and C. C. Davis (editors), *Proc. SPIE Free-Space Laser Communications VI.*, volume 6304, 63040V–1–63040V–9. Aug 2006.
77. Tyson, R. K. "Adaptive optics and ground-to-space laser communications". *Appl. Opt.*, 35(19):3640, 1996.
78. Tyson, R. K. "Bit-error rate for free-space adaptive optics laser communications". *J. Opt. Soc. Am. A*, 19(4):753–758, April 2002.
79. Tyson, R. K., D. E. Canning, and J. S. Tharp. "Measurement of the bit-error rate of an adaptive optics, free-space laser communications system, part 1: tip-tilt configuration, diagnostics, and closed-loop results". *Opt. Eng.*, 44(9), 2005.
80. Tyson, R. K. and B. W. Frazier. *Field Guide to Adaptive Optics*. SPIE Press, 2004.
81. Tyson, R. K., J. S. Tharp, and D. E. Canning. "Measurement of the bit-error rate of an adaptive optics, free-space laser communications system, part 2: multi-channel configuration, aberration characterization, and closed-loop results". *Opt. Eng.*, 44(9), September 2005.
82. VanTrees, H. L. *Detection, estimation, and modulation theory*. Wiley, 2002.
83. Welsh, B. M. "Fourier-series-based atmospheric phase screen generator for simulating anisoplanatic geometries and temporal evolution". *Proc. SPIE*, 3125:327, 1997.
84. Welsh, B.M. and C.S. Gardner. "Effects of turbulence-induced anisoplanatism on the imaging performance of adaptive-astronomical telescopes using laser guide stars". *J. Opt. Soc. Am. A*, 8:69–80, 1991.
85. Wheelon, A. D. *Electromagnetic scintillation. 1, Geometrical optics*. Cambridge Univ. Press, 2001.
86. Writers, Staff. "Northrop Grumman Awarded DARPA Contract To Design Hybrid Optical/RF Communications Network". *Spacedaily.com*, May 2008.
87. Yang, P., W. Yang, Y. Liu, S. Hu, M. Ao, B. Xu, and W. Jiang. "19-element sensorless adaptive optical system based on modified hill-climbing and genetic algorithms". *Proceed. SPIE*, volume 6723, 672303. SPIE, 2007.
88. Yenice, Y. E. and B. G. Evans. "Adaptive beam-size control scheme for ground-to-satellite optical communications". *Opt. Eng.*, Vol. 38(No. 11):1889, November 1999.

89. Yenice, Y. E. and B. G. Evans. “Adaptive beam-size control for ground to satellite laser communications”. *Proc. SPIE*, 3266:221–230, 1998.
90. Yu, M., J. Li, and J. C. Ricklin. “Efficient forward error correction coding for free-space optical communications”. *Proc. SPIE*, 5550:344–353, 2004.
91. Yuksel, H. and C. C. Davis. “Aperture averaging analysis and aperture shape invariance of received scintillation in free-space optical communication links”. *Proc. SPIE*, 6304:63041E, 2006.
92. Yuksel, H. and C.C. Davis. “Aperture averaging experiment for optimizing receiver design and analyzing turbulence on free space optical communication links”. *Conference on Lasers and Electro-Optics (CLEO)*, 1:743–745, May 2005.
93. Yuksel, H., S. Milner, and C. C. Davis. “Aperture averaging for optimizing receiver design and system performance on free-space optical communication links”. *J. Opt. Networking*, 4(8):462–475, 2005.
94. Zhang, Y., T. Zhu, and C. Tao. “Aperture-averaging effects for weak to strong scintillations in turbulent atmosphere”. *Chin. Opt. Lett.*, 2(7):373, 10 July 2004.
95. Zhu, X. and J. M. Kahn. “Free-Space Optical Communication Through Atmospheric Turbulence Channels”. *IEEE Trans. Commun.*, 50(8):1293, 2002.
96. Zhu, X. and J. M. Kahn. “Performance bounds for coded free-space optical communications through atmospheric turbulence channels”. *IEEE Trans. Commun.*, 51(8):1233–1239, 2003.

REPORT DOCUMENTATION PAGE

Form Approved
OMB No. 0704-0188

The public reporting burden for this collection of information is estimated to average 1 hour per response, including the time for reviewing instructions, searching existing data sources, gathering and maintaining the data needed, and completing and reviewing the collection of information. Send comments regarding this burden estimate or any other aspect of this collection of information, including suggestions for reducing this burden to Department of Defense, Washington Headquarters Services, Directorate for Information Operations and Reports (0704-0188), 1215 Jefferson Davis Highway, Suite 1204, Arlington, VA 22202-4302. Respondents should be aware that notwithstanding any other provision of law, no person shall be subject to any penalty for failing to comply with a collection of information if it does not display a currently valid OMB control number. **PLEASE DO NOT RETURN YOUR FORM TO THE ABOVE ADDRESS.**

1. REPORT DATE (DD-MM-YYYY) 29-12-2008		2. REPORT TYPE Doctoral Dissertation		3. DATES COVERED (From — To) Sep 2005 — Dec 2008	
4. TITLE AND SUBTITLE Integrated Approach to Airborne Laser Communication				5a. CONTRACT NUMBER	
				5b. GRANT NUMBER	
				5c. PROGRAM ELEMENT NUMBER	
6. AUTHOR(S) James A. Louthain, Lt Col, USAF				5d. PROJECT NUMBER	
				5e. TASK NUMBER	
				5f. WORK UNIT NUMBER	
7. PERFORMING ORGANIZATION NAME(S) AND ADDRESS(ES) Air Force Institute of Technology Graduate School of Engineering and Management 2950 Hobson Way WPAFB OH 45433-7765				8. PERFORMING ORGANIZATION REPORT NUMBER AFIT/DEE/ENG/09-02	
9. SPONSORING / MONITORING AGENCY NAME(S) AND ADDRESS(ES) Dr. Earl Spillar AFMC/AFRL/RDS US Air Force Research Laboratory Kirtland AFB, NM 87117				10. SPONSOR/MONITOR'S ACRONYM(S)	
				11. SPONSOR/MONITOR'S REPORT NUMBER(S)	
12. DISTRIBUTION / AVAILABILITY STATEMENT Approval for public release; distribution is unlimited.					
13. SUPPLEMENTARY NOTES					
14. ABSTRACT Lasers offer tremendous advantages over RF communication systems in bandwidth and security, due to their ultra-high frequency and narrow spatial beamwidth. Atmospheric turbulence causes severe received power variations and high bit error rates (BERs) in airborne laser communication. Airborne optical communication systems require special considerations in size, complexity, power, and weight. Conventional adaptive optics systems correct for the phase only and cannot correct for strong scintillation, but here the two transmission paths are separated sufficiently so that the strong scintillation is "averaged out" by incoherently summing up the two beams in the receiver. This requisite separation distance is derived for multiple geometries, turbulence conditions, and turbulence effects. Integrating multiple techniques into a system alleviates the deleterious effects of turbulence without bulky adaptive optics systems. Wave optics simulations show multiple transmitters, receiver and transmitter trackers, and adaptive thresholding significantly reduce the BER (by over 10,000 times).					
15. SUBJECT TERMS free-space optical communication, atmospheric turbulence, adaptive threshold, spatial diversity, multiple-transmitters, anisoplanatism					
16. SECURITY CLASSIFICATION OF:			17. LIMITATION OF ABSTRACT	18. NUMBER OF PAGES	19a. NAME OF RESPONSIBLE PERSON
a. REPORT	b. ABSTRACT	c. THIS PAGE			Jason D. Schmidt, Maj, USAF
U	U	U	UU	151	19b. TELEPHONE NUMBER (include area code) (937) 255-3636, ext 7224